PORE- TO FIELD-SCALE MODELLING OF THREE-PHASE FLOW PROCESSES IN HETEROGENEOUS RESERVOIRS WITH ARBITRARY WETTABILITY

ADNAN AL-DHAHLI

Submitted for the degree of Doctor of Philosophy

Institute of Petroleum Engineering

Heriot-Watt University

January 2013

Dedicated to my parents,
my brothers, my sister,
and to my nieces and nephews

ABSTRACT

Most reservoirs, such as carbonate reservoirs not only have structural heterogeneities (e.g. complexly shaped geobodies or fractures). But they also have distributed wettabilities and are mixed- to oil-wet. The interplay of structural and wettability heterogeneities impacts sweep efficiency and oil recovery. Choosing the appropriate Improved Oil Recovery (IOR) or Enhanced Oil Recovery (EOR) technique based on adequate predictions of oil recovery requires a sound understanding of the fundamental controls on fluid flow in mixed- to oil-wet and structurally complex rocks. The underlying multiphase flow processes are modelled with physically robust flow functions, i.e. relative permeability and capillary pressure functions. Obtaining these flow functions is a challenging task, especially when three fluid phases coexist, such as during Water-Alternating-Gas (WAG) injection. In this work we use pore-network modelling, a reliable and physically based simulation tool, to predict three-phase flow functions. We have developed a new three-phase flow pore-network model for rocks with arbitrary wettability, which allows us to analyse the fundamental multi-phase displacement processes. Unlike other models, our model *combines* three main features: (I) A novel thermodynamic criterion for formation and collapse of oil layers that strongly depends on the fluid spreading behaviour and the rock wettability. The model hence captures film/layer flow of oil accurately, which impacts, in particular, the oil relative permeability at low oil saturation and hence the accurate prediction of residual oil. (II) Multiple displacement chains, where injection of one phase at the inlet triggers a chain of interface displacements throughout the network. This allows accurate modelling of the mobilization of disconnected phase clusters that arise during higher order (WAG) floods. (III) The model takes as input realistic 3D pore-networks extracted from pore-space reconstruction methods and Computed Tomography (CT) images, preserving both topology and pore shape of the rock. The model comprises a constrained set of parameters that can be tuned to mimic the wetting state of a given reservoir. We have validated

our model against available experimental data for a range of wettabilities. We demonstrate the importance of film and layer flow for the continuity of the various phases during subsequent WAG cycles and for the residual oil saturations. A sensitivity analysis has been carried out with the full 3D model to predict three-phase relative permeabilities and residual oil saturations for WAG cycles under various wetting conditions with different flood end-points and for different rock types. This revealed a wide range of three-phase relative permeabilities and residual saturations. The pore-scale generated three-phase flow functions have then been used in a heterogeneous reservoir model. Here we demonstrate their impact on the sweep efficiency after gas injection and WAG for a range of realistic wettability scenarios. We show that the uncertainty in flow functions can be as big as the geological uncertainty in a reservoir model that was history matched for an extended waterflood.

PUBLICATIONS

This thesis contains excerpts from the following papers:

- Al-Dhahli A., Geiger S., van Dijke M. I. J., Three-Phase Pore-Network Modelling for Reservoirs with Arbitrary Wettability, *SPE Journal*, in press.
- Al-Dhahli A., van Dijke M. I. J., Geiger S., Accurate modelling of pore-scale film and layer flow for three-phase flow processes in clastic and carbonate rocks with arbitrary wettability. *Transport in Porous Media*, in revision.
- Al-Dhahli A., Geiger S., van Dijke M. I. J., Pore-to-reservoir modelling of three-phase flow processes in reservoirs of arbitrary wettability. *Journal of Petroleum Science and Engineering*, in review.
- Al-Dhahli A., Geiger S., van Dijke M. I. J., Three-phase pore-network modelling for mixed-wet carbonate reservoirs. SPE Paper 147991. In *SPE Reservoir Characterization and Simulation Conference, Abu Dhabi, U.A.E*, 9-11 October 2011.
- Al-Dhahli A., Geiger S., van Dijke M. I. J., Accurate modelling of pore-scale film and layer flow for three-phase EOR in carbonate rocks with arbitrary wettability. SPE Paper 154019. In *SPE Improved Oil Recovery Symposium, Tulsa, Oklahoma, USA*, 14-18 April 2012.
- Al-Dhahli A., van Dijke M. I. J., Geiger S., Pore-to-reservoir modelling of three-phase flow processes in mixed-wet carbonate reservoirs. In *proceedings of the 13th European Conference on the Mathematics of Oil Recovery, Biarritz, France*, 10-13 September 2012.

Desire is the starting point of all achievement,
not a hope, not a wish, but a keen pulsating
desire which transcends everything.
— Napoleon Hill

ACKNOWLEDGMENTS

This thesis is the final destination of my journey towards one of my "dreams". The best and worst moments of my PhD have been shared with numerous people including my friends and colleagues. I am here to THANK all those who contributed in many ways to the success of my mission over the past 3 years. You always remain dear to me.

My first debt of gratitude must go to my first supervisor *Sebastian Geiger*. I want to thank *Sebastian* for his encouragement and serving as a role model to me as a junior member of academia. Without his support and encouragement, this work would have not seen the light. I am also extremely indebted to my second supervisor *Rink van Dijke* for his valuable advice, constructive criticism and his extensive discussions around pore-network modelling. The three-phase network code would have not been at this level without his guidance. Furthermore, I would like to thank my third supervisor, Rachel Wood at Edinburgh University for supervising me as an ECOSSE PhD student. Thanks for your discussion at my winning poster at the University of Edinburgh School of Geosciences GradSchool Conference 2011 at Pitlochry.

I also want to thank Kejian Wu for his constructive feedback on my first year annual review and for supplying carbonate network that was used in chapter 6. Equally, I would like to thank Ken Sorbie for being the reviewer of my second year and for giving me an encouraging feedback to carry on developing my three-phase pore-network code. Also, I thank all the friends and colleagues who attend my public annual review talks at the Institute of Petroleum Engineering (IPE). I thank Lorna Backhouse for passing me the Brugge field data files which I used them in chapter 7. A special thanks goes to Andrey Ryazanov for his help and support during the early stages of my PhD. I would like to thank Branko Bijeljic from Imperial College and Ken Sorbie (again!) for being my examiners. I am so pleased that you enjoyed reading this thesis. I enjoyed the viva very very much.

During my PhD, I was really fortunate to "live" in an office with a fantastic "family" who made me a prince one day. In no particular order, Christine, thank you for the tour in Paris and for the delicious muffins. Claudia, thanks for the Easter Sunday at holy corner, for all invitations to support Germany in the World

Cup and Euro \o/, and for Friday cake. Karen, thanks for all the chocolate and for your patient when I once locked you out of the office. Yan, thank you for advertising LaTeX, and for the few links to get started. Chen, good man from china thank you for the badminton game. Shanti, thanks for the unintentional rumours ☺ about me and for energising the office. Marta, thanks for being part of this office group. Simeon, thanks for different discussions that we had in the bus. Alessandro, welcome to the team and wish you best of luck in this office. Robert thanks for sharing "The Valley of ****" post and all the great discussions on various subjects. Abu Ayman, thank you for being a close friend, close to my heart and thanks for always offering the help.

A thank you goes to some friends and partners. Abdullah, Mohammad and Ghassan, thank you all for encouraging me to apply for a PhD scholarship. Talal Al-Aulaqi, thank you for giving me advices during writing my PhD proposal and again a big thanks to *Sebastian* and *Rink* for helping me during that time. Kirsty and Cheryl, thank you for reading some sections of my thesis. Thanks to all my tennis partners, in particular, Natalia, thank you for all the practice games. Tom, thanks for long tennis battles. Usman, thanks for that few tennis games and for occasional discussions about pore-network modelling. Thanks to all of my football mates at IPE. You know who you are!. Thanks to all my muslim friends at IPE for the daily discussions. Patricia, muchas gracias por tu ayuda. Laura, thank you for being an amazing friend and for the good time sharing the Scottish culture.

I take this opportunity to sincerely acknowledge Petroleum Development Oman (PDO) for funding, not only my PhD but, my studies in Oman and UK during the past 9 years, including my A-level and language, undergraduate, master, and finally PhD. I would like to thank Asad Al-Mahrezi for his prompt replies to my emails. Suad Al-Battashy, for supporting me regarding some financial issues at PDO. Hamed Al-Hadhrami, for visiting Edinburgh last summer. Mohammed Ali for keeping my allowances coming on time. I am looking forward to serving the company for the next 5 years at least.

I would like to thank ExxonMobil Research Alliance, Fundamental Controls of Flow in Carbonates $(FC)^2$, for giving me the opportunity to attend their meetings and presenting my posters. I thank as well itf-ISF sponsors for letting me to be part of their project. I thank CMG Reservoir Simulation Foundation for paying my travel expenses to the US. Once again, the big thank goes to the mastermind *Sebastian* who put me in these meetings and projects.

I wish to thank my family. Their love provided my inspiration and was my driving force. I owe them everything and wish I could show them just how much I love them. I dedicate this work to them.

Adnan Al-Dhahli
Edinburgh, January 2013

ACADEMIC REGISTRY
Research Thesis Submission

Name*:*	Adnan Rashid Saif Al-Dhahli		
School/PGI:	IPE		
Version: *(i.e. First, Resubmission, Final)*	Final	Degree Sought (Award **and** Subject area)	PhD in Petroleum Engineering

Declaration

In accordance with the appropriate regulations I hereby submit my thesis and I declare that:

1) the thesis embodies the results of my own work and has been composed by myself
2) where appropriate, I have made acknowledgement of the work of others and have made reference to work carried out in collaboration with other persons
3) the thesis is the correct version of the thesis for submission and is the same version as any electronic versions submitted*.
4) my thesis for the award referred to, deposited in the Heriot-Watt University Library, should be made available for loan or photocopying and be available via the Institutional Repository, subject to such conditions as the Librarian may require
5) I understand that as a student of the University I am required to abide by the Regulations of the University and to conform to its discipline.

* *Please note that it is the responsibility of the candidate to ensure that the correct version of the thesis is submitted.*

Signature of Candidate*:*		Date:	

Submission

Submitted By *(name in capitals):*	
Signature of Individual Submitting:	
Date Submitted:	

For Completion in the Student Service Centre (SSC)

Received in the SSC by *(name in capitals):*			
Method of Submission *(Handed in to SSC; posted through internal/external mail):*			
*E-thesis Submitted (**mandatory for final theses)***			
Signature:		Date:	

Please note this form should bound into the submitted thesis.

Updated February 2008, November 2008, February 2009, January 2011

CONTENTS

LIST OF FIGURES

LIST OF TABLES

LIST OF ALGORITHMS

ACRONYMS

AM Arc Meniscus

BFM Bellman-Ford-Moore

CT Computed Tomography

EOR Enhanced Oil Recovery

IOR Improved Oil Recovery

IP Invasion Percolation

MTM Main Terminal Meniscus

NTIP Non-Trapping Invasion Percolation

SEM Scanning Electronic Microscope

PBF Pore Body Filling

TIP Trapping Invasion Percolation

TNO Dutch Organization for Applied Scientific Research

WAG Water-Alternating-Gas

1

INTRODUCTION

Commonly, oil field development comprises three main stages: (1) Primary recovery where hydrocarbons are recovered by using the reservoir natural energy as drive mechanisms (e.g. water drive, solution gas drive, gas cap drive and gravity drainage), which moves the hydrocarbons towards the production wells. However, at some point the hydrocarbons become immobile. This could be, for example, because the reservoir pressure drops as a result of production of hydrocarbons. (2) Secondary recovery where the reservoir pressure is maintained by injecting fluids, commonly water, into the reservoir. Water flooding helps to sweep the oil towards the production wells, creating regions where two phases, oil and water, coexist and oil can be trapped. When water breaks through at production wells and the water cut is high, further oil production may not be economical. Hence it can become necessary to implement a new development technique to increase the oil production rate and decrease water production. (3) Tertiary recovery comprises a range of Enhanced Oil Recovery (EOR) methods, which can be applied to further improve oil production. The main idea behind these methods is to mobilise trapped oil, i.e. reduce the residual oil saturation, and transport it to the production wells. Examples of EOR techniques include steam injection, polymer flooding, and Water-Alternating-Gas (WAG) injection. The selection of a specific EOR technique requires an accurate prediction of incremental oil recovery for the given field.

WAG injection is an EOR technique that has already been implemented successfully in many oil fields (Christensen et al., 2001) and is increasingly considered for some Middle East carbonate fields to improve the oil recovery (Kalam et al., 2011). WAG injection can improve oil recovery by contacting unswept zones in the reservoir and increasing the microscopic sweep efficiency in the three-phase

regions. Three-phase regions are generated during WAG injection because two fluids, water and gas, with different physical properties are injected (Fig. 1.1). Although there is field and experimental evidence that WAG is a viable EOR scheme, the exact microscopic mechanism that leads to improvement in oil recovery during WAG is still not well understood. Many factors still need to be considered for successful implementation of WAG injection. Jackson et al. (1985) found that the wetting state of the reservoir has a major influence on the WAG flood performance and a careful selection of the WAG ratio is required. The most popular WAG ratio in field applications is 1:1 (Christensen et al., 2001). Maintaining this ratio may be challenging due to limited gas availability. Christensen et al. (2001) carried out a review for 59 oil fields where the WAG injection was applied, mostly as a tertiary recovery technique. The dates when WAG was started in these fields ranges from 1957 to 1996. Miscible WAG injection was implemented in the majority of the fields (47) whereas only a few fields (10) used immiscible WAG injection (Fig. 1.2a). 88% of the reviewed projects were onshore and the remaining 12% were offshore. WAG injection has been implemented in clastic and carbonate reservoirs (Fig. 1.2b). The typical increase in oil recovery due to WAG injection commenced was around 5% with some fields reporting an increase in oil recovery of up to 20%. Hydrocarbon gas and CO_2 were the most common gases that were injected during WAG (Fig. 1.2c).

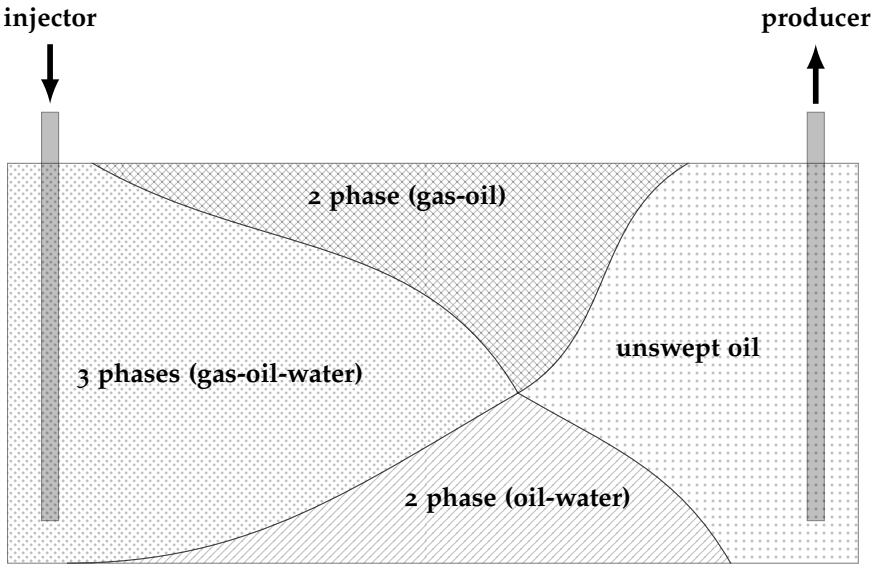

Figure 1.1: Conceptual model of WAG injection. Water and gas are injected through same well, generating two- and three-phase region.

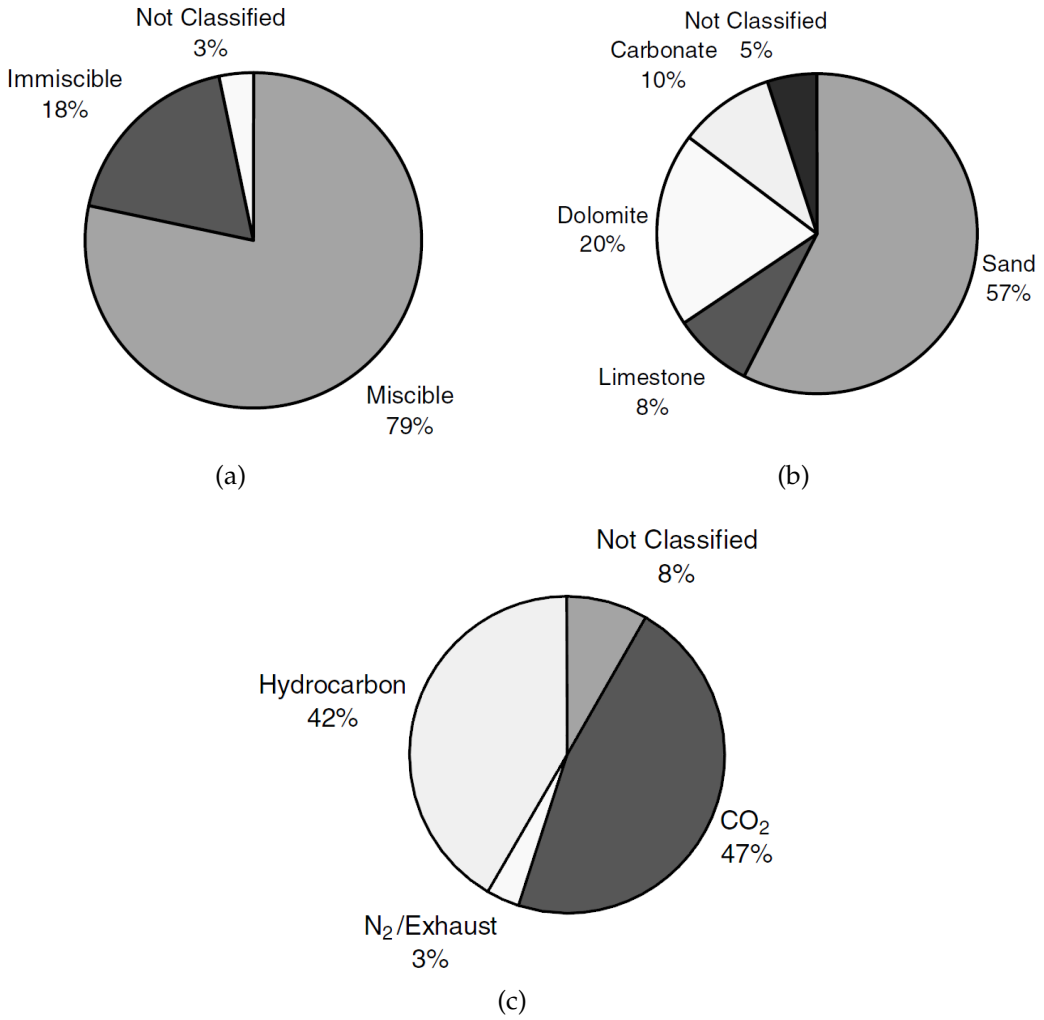

Figure 1.2: Summary of WAG injection for 59 oil fields between 1957 and 1996 by Christensen et al. (2001): (a) Distribution of miscible and immiscible WAG (b) Distribution of rock types. (c) Distribution of injection gases.

Despite the encouraging results of WAG injection for improving oil recovery, the intrinsic physical mechanisms of three-phase flow that control this process are still not well understood. Fundamentally, the physical processes which govern the simultaneous movement of these phases occur at the pore space. Yet being able to accurately model these physical processes at the continuum-scale, i.e. for the reservoir, is paramount to making well informed decisions about the success or failure of implementing WAG for a given field. Holm et al. (2010) have shown that subtle changes in wettability at the pore-scale during three-phase flow impact the macro-scale displacement patterns fundamentally. Thus, it is crucial to analyse the displacement processes at the pore-scale in order to predict their consequences at the macro-scale, especially when all three phases coexist in one region of the reservoir or even in a single pore. We point out that

WAG enhanced oil recovery is not the only application of three-phase flow. For example, if CO_2 is used as the injected gas, it can get sequestered during this process (Qi et al., 2008, 2009). Other applications could also include groundwater remediation strategies such as steam injection during non-aqueous phase liquid contamination (e.g. Falta et al., 1992a,b).

Accurate prediction of oil recovery during WAG, or three-phase flow in general, at the field scale requires flow functions, i.e. relative permeabilities and capillary pressures, and fluid saturations. These are the up-scaled expressions of the displacement physics at the pore scale. It is extremely difficult, time consuming and expensive to measure relative permeabilities and capillary pressures for three-phase flow in a laboratory setting. Results are also very uncertain at low oil saturations (Oak, 1990), where accurate predictions are needed because the corresponding (trapped) oil is targeted during WAG injection. Furthermore, there is an infinite number of scenarios (fluid arrangements and displacement paths) of a three-phase system. This renders the reliable experimental determination of flow functions for three-phase displacements highly challenging. Hence, empirical correlations are frequently used to predict the relative permeabilities and capillary pressures based on available two-phase data (Stone, 1970, 1973; Baker, 1988; Blunt, 2000; Juanes and Patzek, 2004).

However, empirical models often have little or no physical basis and, thus, the prediction could differ from one model to the other and they may also be significantly different from relative permeabilities determined in laboratory measurements, Fig. 1.3, (Blunt, 2000). These empirical models also have some important limitations: most empirical models have been developed for water-wet systems and fail to capture oil flow at very low saturation.

For water-wet system, when the oil saturation reaches below approximately $S_o = S_{orw}$ during gas injection, it was observed that the oil relative permeability is proportional to the oil saturation squared, quadratic behaviour $k_{ro} \propto S_o^2$ (Fig. 1.4), where, S_o denotes oil saturation, S_{orw} denotes residual oil during waterflooding and k_{ro} denotes oil relative permeability. The quadratic behaviour $k_{ro} \propto S_o^2$ can be explained as follows: during gas injection (after primary drainage or waterflood), gas displaces oil from the pore space. However, oil is not removed completely from the pore space but it remains in the pore corners as layers separating water residing in the corners, and gas in the center of the pore. At low

oil saturations, the drainage of oil results from these oil layers. Hence, the oil saturation is proportional to the oil layers area and the oil relative permeability is calculated using the hydrodynamic conductance of oil layers, which is proportional to the square of the area occupied by the oil layers. Therefore, $k_{ro} \propto S_o^2$ (Blunt, 2000).

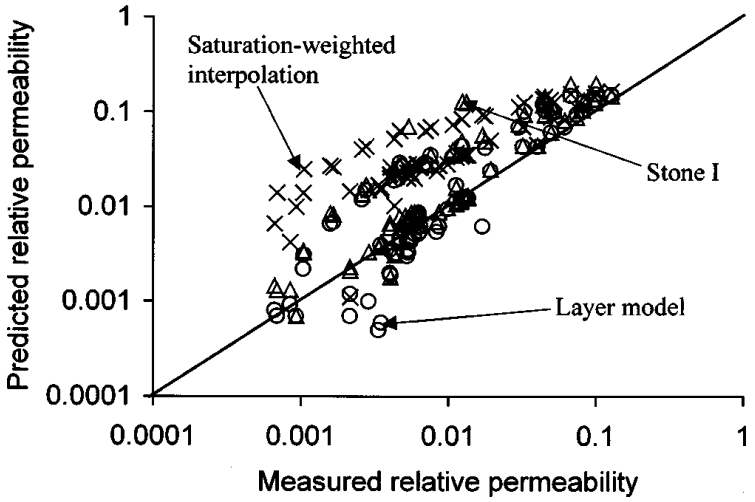

Figure 1.3: Cross-plot of experimental and predicted three-phase relative permeabilities using different empirical models. Data are obtained by predictions using three empirical models: saturation-weighted interpolation is denoted by the crosses (Baker, 1988), saturation-weighted interpolation including layer drainage is denoted by the circles (Blunt, 2000), and Stone I is denoted by the triangles (Stone, 1970). In general, these models overestimate three-phase oil relative permeability. The layer model and Stone I give better predictions than saturation-weighted interpolation. However, they still differ from the measurements by a factor 10 for some points. Taken from Blunt (2000).

In the last two decades, network modelling, a physically-based simulation tool, has been proposed as an alternative approach to predict the two- and three-phase relative permeabilities and capillary pressures functions. This method uses CT imaging (Dunsmuir et al., 1991; Spanne et al., 1994; Coles et al., 1998) of core samples to construct 3D digital rocks. Alternatively, 2D thin sections can be used by different reconstruction methods (commonly, process-based algorithms (Bakke and Øren, 1997; Øren and Bakke, 2003) and statistical methods (Wu et al., 2006; Okabe and Blunt, 2007)) to obtain a 3D digital rock, from which a network of pore bodies connected by pore throats can be extracted (Jiang et al., 2007; Dong and Blunt, 2009). The network is then used to simulate the flooding sequence that occurs in the real reservoir. During these simulations, it is possible to compute the relative permeabilities, k_r, and capillary pressures, P_c. Fig. 1.5 summarises the common approaches used to obtain the relative permeabilities

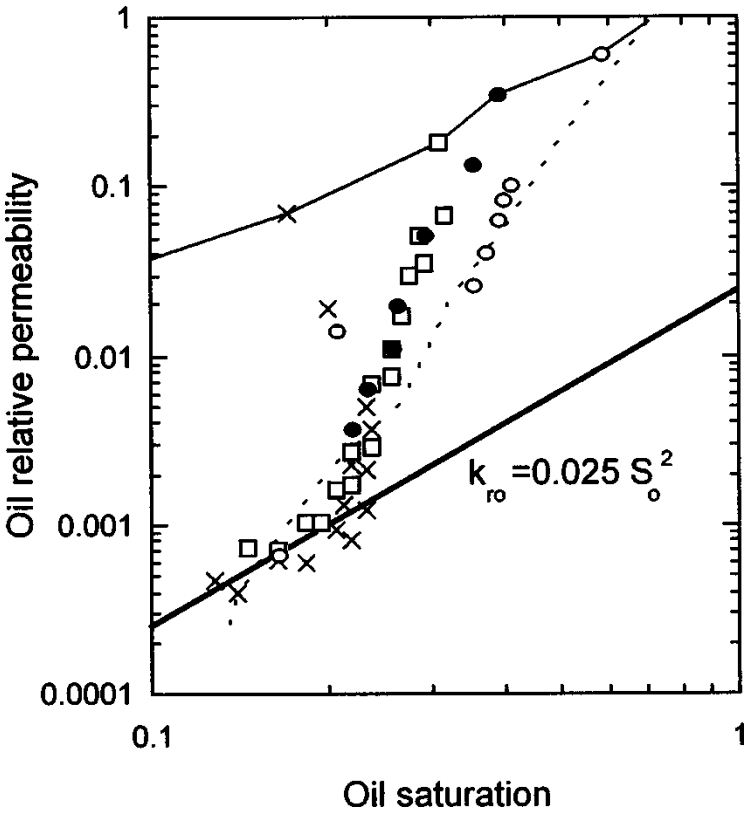

Figure 1.4: Oil relative permeabilities for a water-wet sandstone from Oak (1990). The three-phase data are denoted by symbols for different gas-water injection ratios. The solid line and the dashed line denote the two-phase experimental data of oil-water and gas-oil at connate water, respectively. A possible oil layer drainage regime is indicated by a quadratic fit to the data at low oil saturation (Blunt, 2000).

and capillary pressure either from digital rock or pore-network modelling or by using experimental data.

Note that the 3D digital rocks can be employed directly to simulate fluid flow using for examples the Lattice-Boltzmann method (Chen and Doolen, 1998; Pan et al., 2004) and finite element-finite volume simulation method for modelling single-phase fluid flow (Zaretskiy et al., 2010). However, the current computational power is not capable of simulating multi-phase flow in a representative pore volume, especially for digital rocks that represent heterogeneous rocks, such as carbonates containing micro-pores, large vugs and fractures. The network modelling approach is able to overcome such limitations (Jiang et al., 2012).

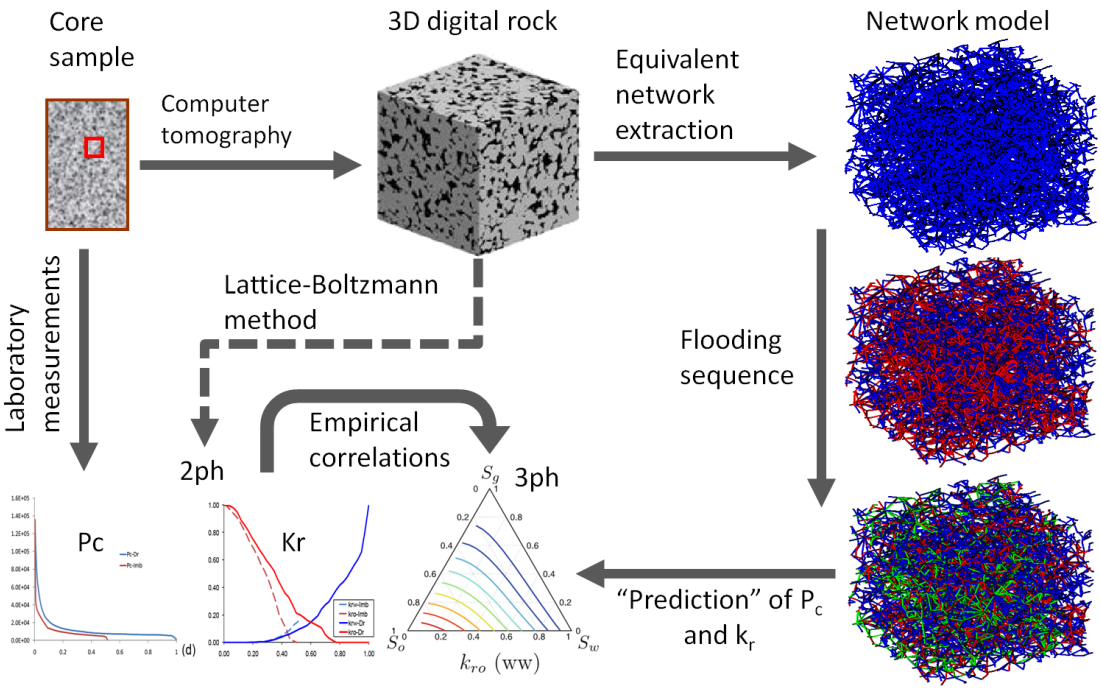

Figure 1.5: Different workflows to obtain relative permeabilities and capillary pressures of two- and three-phase flow starting from core sample.

1.1 OBJECTIVES AND AIMS

The main objective of this work is to develop a state-of-the-art, physically-based pore-network model that is capable of computing reliable three-phase flow functions. The new pore-network model will be implemented into a computer software to provide a tool that can be used by researchers for academics and industry involved in three-phase flow processes. The main aims of developing this model are:

1. Overcome some of the limitations of three-phase empirical models. These limitations are: (a) Empirical models have been developed for water-wet systems, but the wettability of real reservoir rocks often ranges from mixed- to oil-wet. Our new model is developed for rocks with arbitrary wettability. (b) Empirical models fail to capture the flow of oil at very low oil saturation. Here, flow is controlled by film and layer flow. Our new model is able to capture the film and layer flow adequately.

2. Model the three-phase physics at the pore-scale accurately. We use a novel thermodynamic criterion introduced by van Dijke et al. (2004a, 2007) to accurately model pore-scale film and layer flow during three-phase flow.

Additionally, we model the movement of disconnected phase clusters by multiple displacements, which has been observed by micromodel experiments to control residual oil.

3. Derive physically consistent capillary pressure and relative permeability functions for two- and three-phase flow and use them in field-scale simulations of WAG injection.

The new pore-network model can be employed to "predict" three-phase flow functions, which can be used to simulate three-phase EOR technique, including but not limited to WAG injection, at the field-scale. Here we state the key objectives of this work at the field-scale:

1. Compare pore-scale generated three-phase flow functions with empirical three-phase flow functions for predicting field-scale oil recovery during tertiary gas injection in oil reservoirs.

2. Study the efficiency of WAG injection in reservoirs of different wettability, using three-phase flow functions which have been derived from our new pore-network model.

3. Explore the impact of pore-scale wettability compared to the impact of geological uncertainty for predicting field-scale oil recovery during WAG.

In summary, we have developed an advanced three-phase pore-network model that incorporates the most important three-phase physics at the pore level. This enables us to investigate different effects at the pore scale and to overcome the aforementioned limitations of empirical three-phase flow models. The pore-scale generated three-phase flow functions have been used in a synthetic but realistic reservoir model for which we demonstrate their impact on sweep efficiency after gas injection and WAG for a range of realistic wettability scenarios. In the following sections, we describe briefly the pore-network modelling. Then, we state the basic displacement processes that occur at the pore scale and must be captured in a pore-network model. After that, we review the most well-known three-phase pore-network models and present their contributions in understanding the three-phase flow in porous media and their limitations. Finally, we summarize the structure of this thesis.

1.2 PORE-NETWORK MODELLING

In network modelling, the pore space of porous medium is represented by a network of pore bodies (nodes) connected by pore throats (bonds), Fig. 1.6. The network is usually extracted from 3D images of the pore space (Bakke and Øren, 1997; Øren and Bakke, 2003; Al-Kharusi and Blunt, 2007; Jiang et al., 2007). Effective properties are assigned to these nodes and bonds. Additionally, different shapes are assigned to these pores and throats to enable to model the multiphase physics (e.g. wetting films or layers at the pore corners) at the pore scale. Structure of pore space, including realistic pore shape characterisation, will be presented in detail in chapter 3.

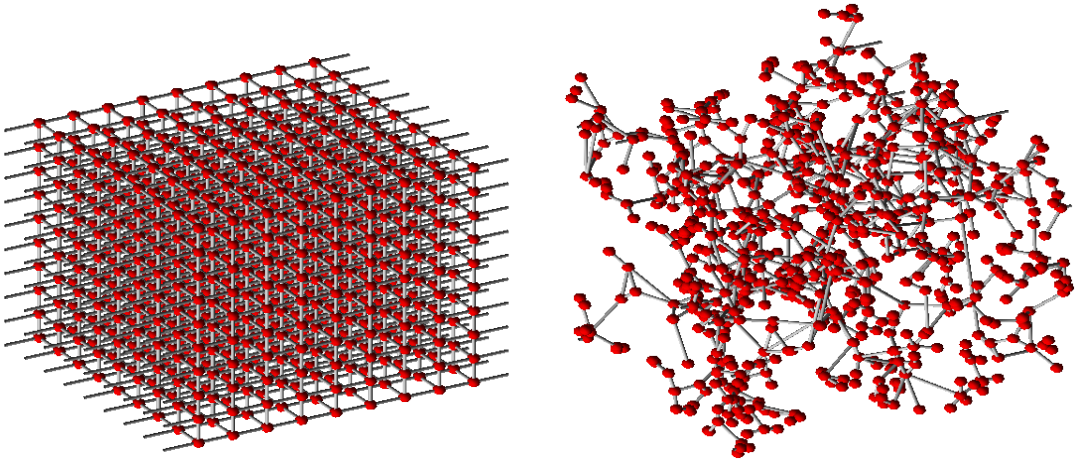

(a) (b)

Figure 1.6: Different networks consisting of the same number of pore bodies. (a) A structured network (regular cubic lattice). (b) An unstructured network. Red denotes pore bodies and gray denotes pore throats. In the context of network modelling, pore bodies are refereed as nodes and pore throats as bonds. Note that the size of pore throats and pore bodies are not scaled.

The pore-network model is used to simulate the flooding sequence that occurs in the real reservoir. Initially, the pore-network is completely filled by water. The network is then flooded with oil up to irreducible water saturation to mimic oil migration into the reservoir, during primary drainage. This represents the initial state of the reservoir. Then, the network wettability is changed, modelling the alteration of the reservoir wettability during ageing (Kovscek et al., 1993). After that, the imbibition process is performed to model reservoir production during waterflooding. Finally, gas is injected (tertiary gas injection) in the network to model oil production in the reservoir during gas injection. This flooding

sequence is often simulated to obtain the flow properties, e.g. relative permeabilities and capillary pressures. To predict such properties, accurate description of the multiphase flow at pore level is essential.

At the equilibrium conditions in a three-phase system, oil, water and gas could coexist in one pore. An important feature of three-phase physics is the ability of one fluid to spread over the other in the presence of a third fluid in the system, expressed by the spreading coefficient. This feature has a crucial impact in determining the fluid configurations in the network pores, and hence the three-phase flow. For example, a fluid can be present as a layer between the other two phases if only its spreading coefficient is zero or positive, discussed in chapter 2. Capturing oil films and layers flow is crucial for more accurate prediction of oil relative permeability and residual oil (Piri and Blunt, 2005a,b).

In a three-phase system, the wetting order of the phases in the presence of a solid surface is controlled by three-phase contact angle between each of the three fluid pairs when the three phases coexist. The wetting order defines the three phases as: wetting phase, intermediate phase and non-wetting phase. In petroleum systems, three general wetting orders are possible (from most to least wetting): water-oil-gas, oil-water-gas and oil-gas-water. Further discussion about three-phase system will be described in chapter 2.

1.3 PORE-SCALE DISPLACEMENTS

In pore-network modelling fluid invasion is often based on the Invasion Percolation (IP) algorithm where one phase displaces another phase by quasi-static pore-scale displacement rules. This may cause clusters of connected fluid phases to break up and merge, thus resulting in new fluid distributions. There are two types of IP (Knackstedt et al., 2000): (a) Non-Trapping Invasion Percolation (NTIP) where the defending phase is infinitely compressible and thus it can be displaced from any accessible pore. (b) Trapping Invasion Percolation (TIP) where the defending phase is incompressible, implying that it can be trapped by the invading phase. The latter is commonly used in pore-network modelling.

There are three main types of displacements at the pore-scale which all have been observed in the micromodel experiments (Lenormand et al., 1983): (1) piston-

like displacement, (2) snap-off, (3) pore-body filling. They are described briefly in the following.

1.3.1 *Piston-like displacement*

This event occurs when the invading phase from an adjacent pore body displaces the bulk of the defending phase from a throat (Fig. 1.7). In a pore with angular cross-section, the invading phase may not displace the defending phase completely. For example in a water-wet system, oil could invade a water-filled pore during drainage, displacing water from the centre of the pore. Some water may be left in corners of the pore as films. This displacement also may involve the formation of oil layers in the subsequent floods, as explained in section 4.4. Formation of these films and layers plays a crucial role in maintaining phase connectivity within the network. Therefore, intensive studies have been conducted to develop an accurate model that can predict where these layers form during three-phase flow (Fenwick and Blunt, 1998a,b; van Dijke et al., 2004a; Piri and Blunt, 2005a,b; van Dijke et al., 2007). We discuss the pore occupancies arising from this type of displacement in chapter 4.

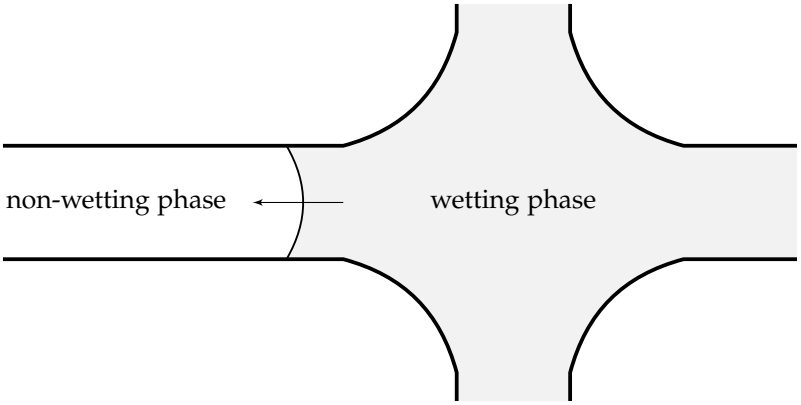

Figure 1.7: Piston-like displacement where wetting phase occupies a pore body displace non-wetting phase from a throat.

1.3.2 *Snap-off displacement*

Snap-off displacement occurs when the wetting phase, surrounding the non-wetting phase in a pore or throat, displaces the non-wetting phase from the same pore or throat. Mohanty et al. (1987) referred to snap-off as a choke-off dis-

placement (Fig. 1.8) where films of water, surrounding oil in a pore constriction or throat, start to swell until they break the oil-neck meniscus, an arc meniscus, forming two new head menisci, or main menisci during a water flood in a water-wet pore. Eventually, the throat becomes filled completely by water. This process results in disconnection of the oil phase, which may contribute to the entrapment by forming disconnected clusters that are completely surrounded by water clusters. The stability of the arc meniscus depends on the local pore geometry and surface wettability of the pore, as will be shown in section 4.4.2.

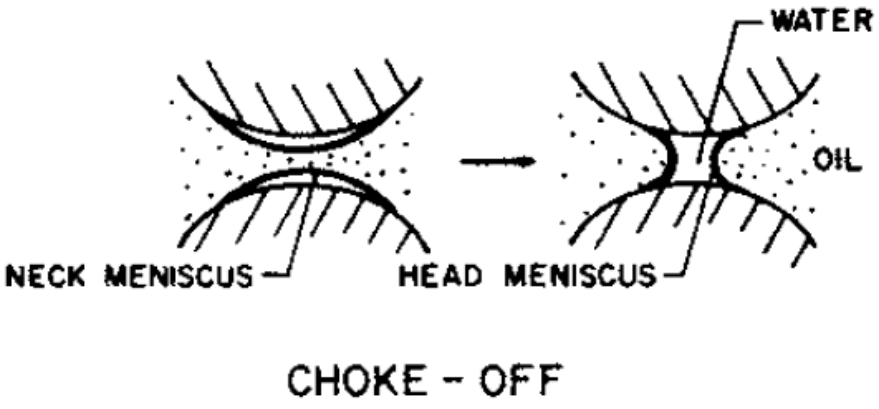

Figure 1.8: Choke-off or snap-off displacement in a throat (Mohanty et al., 1987).

1.3.3 *Pore-body filling displacement*

Pore Body Filling (PBF) occurs when the wetting phase in the centre of a pore body is displaced by the non-wetting phase of the neighbouring throats (Fig. 4.14). The capillary entry pressure is controlled by the inscribed radius of the pore-body and the number of adjoining throats that can contribute to the displacement of the defending phase from the pore-body. If only one neighbouring throat accommodates the defending phase, then PBF becomes a normal piston-like displacement.

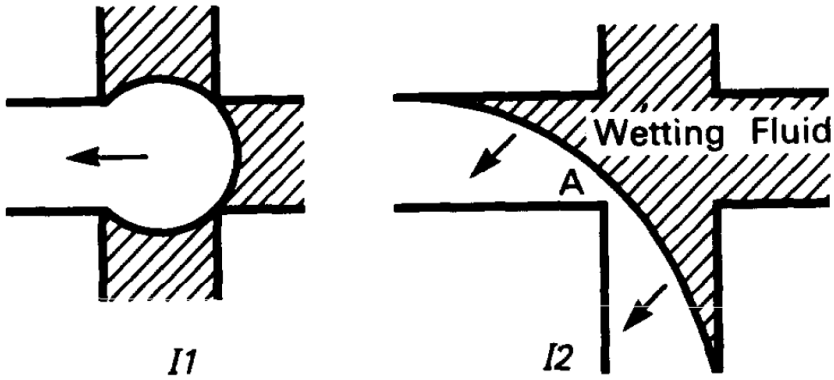

Figure 1.9: Pore-body filling events. I1 and I2 denote one or two throats occupied by a non-wetting phase (e.g. oil), resepectively (Lenormand and Zarcone, 1984).

1.4 THREE-PHASE PORE-SCALE MODELS

Fatt (1956) pioneered the use of network model to represent porous media. Since then, a wide range of network models were developed to study different flow processes in porous media. However, these studies were limited to single- and two-phase flow until 1984 when the first three-phase network model was introduced (Heiba et al., 1984). In the following we will review the most known three-phase network model:

Heiba et al. (1984) introduced the first three-phase network model by extending a previous two-phase model (Heiba et al., 1983) to calculate relative permeabilities and capillary pressures. The porous medium was represented by a Bethe tree or Cayley network. Each pore was able to accommodate one fluid only at any given time. Six basic types of displacements, o$\rightarrow$w, o$\rightarrow$g, w$\rightarrow$o, w$\rightarrow$g, g$\rightarrow$w and g$\rightarrow$o, where labels o, w, and g stand for oil, water, and gas respectively, were implemented. Displacement was controlled by the local capillary pressure. It was assumed that gas is the least wetting phase, oil is the intermediate wetting phase and water is the most wetting phase. It was found that the gas and water relative permeabilities were functions of their own saturations. Oil iso relative permeability curves (isoperms) were found to be strongly curved, suggesting that the oil relative permeability was not a function of its own saturation. It was further concluded that three-phase relative permeabilities at given saturation are dependent on saturation paths, i.e. the saturation history, of the system.

Soll and Celia (1993) developed a capillary-dominated two-phase and three-phase network model. The porous media were represented by regular 2D and

3D networks, which consisted of pore bodies that were connected by pore throats. Every pore could accommodate one fluid as well as wetting layers of a different phase. The effect of gravity was incorporated by modifying the local capillary pressures whereas the viscous forces were ignored. The model was able to calculate the capillary pressure-saturation. The model was used to simulate micromodel experiments (Soll et al., 1993). For two-phase flow, the predicted capillary pressures were in good agreement with the measured values. For three-phase flow, the model could not match the measured three-phase capillary pressure values. The model was not used to compute three-phase relative permeabilities.

Øren et al. (1994) developed a two-dimensional network model to study immiscible gas injection into residual oil after waterflooding, i.e. tertiary gas injection, for spreading and non-spreading oil in strongly water-wet systems. The pore throats were rectangular ducts and the pore bodies were spherical pores. The authors gave a detailed description of the pore level displacement mechanisms which included a double drainage mechanisms where gas connected to the inlet displaces trapped oil that displaces water connected to the outlet. This allowed immobile oil to connect to continuous oil and thus increase the oil recovery. Oil recoveries computed by the model were in good agreement with measured values from the micromodel experiments (Øren and Pinczewski, 1991; Øren et al., 1992). The model confirmed the importance of oil spreading films in improving the recovery of waterflood residual oil for positive spreading systems. There were no relative permeabilities computed from the model.

Pereira et al. (1996) and Pereira (1999) developed a numerical simulation model to describe three-phase, drainage dominated, fluid flow in strongly water- and oil-wet systems, considering both capillary and viscous forces. Pores and throats were assumed to be lenticular in cross-section, so wetting and spreading layers can be present. The pore-scale displacement mechanisms were based on the work by Øren and Pinczewski (1995). Simulated fluid recoveries closely matched the corresponding experimental fluid recoveries of Øren et al. (1992) and Øren et al. (1994). A large difference in oil recovery was observed for spreading and non-spreading systems. The model confirmed that the displacement of the intermediate wetting phase is dependent on the saturation history of the displacement. No relative permeabilities were calculated in this work.

Mani and Mohanty (1997, 1998) developed a pore-network model to study the effect of spreading coefficients on three-phase flow through porous media in water-wet systems. A three-dimensional cubic lattice was used to represent the porous medium. Simulation of larger systems was enabled by re-injection of fluids produced at the outlet into the inlet of the network. Capillary-controlled immiscible gas injection into a porous medium, initially saturated with water and oil, was simulated. The following three displacement events were considered during gas invasion: (1) Direct water drainage where gas connected to the inlet displaces water connected to the outlet. (2) Direct oil drainage where gas connected to the inlet displaces oil connected to the outlet. (3) Double drainage where gas connected to the inlet displaces trapped oil that displaces water connected to the outlet. It was found that the direct water drainage event was preferred over double drainage when the spreading coefficient was highly negative. The residual oil saturation to gas invasion, starting after a waterflood, was higher for a system with negative spreading coefficient because of the absence of oil layers. The water relative permeability in two-phase and three-phase systems was found to be a function of its own saturation and was independent of the spreading coefficient and saturation history. The gas relative permeability curves, for positive spreading coefficient systems, were very similar to gas-oil drainage curves. This agrees with the common assumptions made in empirical models that the gas relative permeability is a function of its own saturation only. However, this assumption broke down for systems with negative spreading coefficient, in which the gas relative permeability was dependent on the imposed oil-water capillary pressure, the saturation history and its own saturation. For systems with negative spreading coefficient, the oil relative permeability remained zero throughout the process, if there were no connected oil paths present at the start of the gas injection. For similar initial conditions, in a system with positive spreading coefficient, the oil relative permeability started at zero and then increased, albeit that the oil saturation decreased, because oil is connected through films in gas-filled paths. This suggested that the oil relative permeability was a function of the oil saturation, the imposed oil-water capillary pressure, the spreading coefficient, and the saturation history.

Fenwick and Blunt (1998a,b) developed a network model that was able to calculate relative permeability, capillary pressure and oil recovery for water-wet

media. The porous medium was presented by a cubic lattice of pores connected by throats. All the pores and throats had equilateral triangular cross-sections to allow for corner films and layers to exist. The authors used the model to address two unique aspects of three-phase flow: (1) Formation of the oil layers sandwiched between water corner films and gas in the centre of the pore. Such oil layers were observed in micromodel experiments (Chatzis et al., 1988; Øren et al., 1992; Soll et al., 1993; Øren and Pinczewski, 1994). These oil layers allow oil to drain to low saturation during gas flood. In order to model these layers, an approximate analytical model of oil layers conductance was introduced, which was used to compute oil relative permeability in the layer drainage regime. (2) A three-phase displacement involves changes in two independent saturations. This leads to infinite number of saturation paths which potentially have different relative permeability and oil recoveries. A self-consistency procedure was presented to allow the network model to find relative permeabilities for the corresponding saturation path, produced by a one-dimensional Buckley-Leverett simulator. Drainage through connected oil layers was observed to cause the high oil recovery during gas injection. These oil layers were found to be on the order of microns in thickness and can be present in systems with negative spreading coefficient. At low oil and water saturation, oil relative permeability was found to vary as a quadratic function of oil saturation (as in Fig. 1.4). This finding was consistent with experimental results (Grader and O'Meara Jr., 1988; Sahni et al., 1998).

Laroche et al. (1999a,b) developed a two-dimensional regular lattice network model to study the impact of small-scale wettability heterogeneities on gas injection efficiency. The network model consists of cylindrical pore bodies, interconnected by pore throats of triangular cross-section. The authors used the model to simulate imbibition-drainage events and flow through films, as observed in micromodel experiments (Laroche, 1998). In the experiments, the initial spreading coefficient was positive, suggesting that oil was spreading. The capillary number of the experiment indicated that the displacements were capillary dominated. The authors found that gas injection has higher efficiency in uniformly oil-wet systems, compared to water-wet systems. This was because oil films in uniformly oil-wet systems had higher conductivity than oil layers in water-wet systems. Additionally, in uniformly oil-wet systems gas was blocked by water

that occupied large pores, giving a more uniform gas front. In non-uniformly oil-wet system, gas preferred to invade the oil-wet regions because the pathways in these regions exhibited less resistance to gas invasion compared to the water-wet regions. In the water-wet regions, the high connectivity of water increases the resistance to flow.

Hui and Blunt (2000a,b) developed a mixed-wet model comprising a capillary bundle of horizontally aligned pores. All pores had the same length and cross-section (equilateral triangular) but had different cross-sectional sizes. The model incorporated wettability alteration by changing the wettability of all of the pore surfaces in contact with the oil after primary drainage. Ten different fluid configurations were considered in a single pore to calculate the capillary pressure for all possible displacements. Oil and water layer formation and collapse was analysed. The authors introduced approximate expressions for fluid conductance to compute the three-phase relative permeabilities. Initially, the network was assumed to be water-saturated. Three floods were simulated: primary drainage, waterflooding and gas injection. The effect of wettability on three-phase flow was studied as well. For water-wet systems, there was good agreement with the theoretical and experimental results (Fenwick and Blunt, 1998a; Sahni et al., 1998; Dicarlo et al., 2000) particularly with respect to the quadratic oil layer drainage regime (as in Fig. 1.4) and the effect of spreading coefficient. Oil forms layers during gas injection, which help it to drain to very low saturation. It was found that the relative permeability of the intermediate-wetting phase, for different wetting systems, depends on its own saturation and on initial oil saturation at the beginning of gas injection.

Lerdahl et al. (2000) reconstructed a 3D Berea sandstone, using the process based reconstruction technique developed by Bakke and Øren (1997). The reconstructed pore space was translated to a pore network. This model was the first to simulate three-phase flow in a realistic pore network. However, the model was limited to water-wet systems. The model was used to compute the two-phase and three-phase relative permeabilities. The predicted relative permeabilities were in agreement with experimental data (Oak, 1990). The theory that three-phase relative permeabilities of the wetting phase (water) and nonwetting phase (gas) are independent of the saturation history, whereas recovery and relative

permeability of the intermediate phase (oil) is strongly dependent on the saturation history was confirmed in the simulations.

Larsen et al. (2000) used a network model based on the work of Fenwick and Blunt (1998a,b) to simulate three-phase immiscible WAG injection processes in micromodel experiments. The network model was a regular cubic lattice which consisted of pore bodies (nodes) and throats (bonds). The pore sizes were calculated based on the inscribed radius of their cross-sections, which were assumed to be squares. Four possible fluid combinations were allowed to be present in a single pore: water; water and oil; water and gas; oil, water and gas. An iterative procedure, similar to the self-consistency procedure of Fenwick and Blunt (1998a,b) was used, to link the pore-scale, providing the relative permeabilities, and field-scale, providing the saturation paths.

van Dijke et al. (2000, 2001a,b) developed a capillary bundle model of cylindrical tubes for non-spreading and spreading oil in mixed-wet and fractionally-wet systems. A fraction of pores is assumed to be strongly water-wet and the remaining pores are oil wet. The porous medium was assumed to be completely accessible. Consistent linear relationships were introduced for the cosines of the gas-oil and gas-water contact angles as a function of the oil-water contact angles, when all three interfacial tensions and cosine angles of oil-water are given. These linear relationships will be presented in detail in chapter 2 and they will be used in our new network model. The saturation space was divided into regions based on saturation dependencies of the corresponding relative permeabilities. The number of these regions depends on the interfacial tensions, the range of the pore sizes, and the degree of wettability of the pores. In each region there was only one phase for which the relative permeability depended on more than one phase saturation. This phase is called the intermediate-wetting phase. For the remaining two phases, the relative permeabilities, depended on their own saturation.

van Dijke et al. (2004b, 2006) developed a regular three-dimensional three-phase network model for different wettability systems. The network consists of throats with a circular cross-section. Films and layers were incorporated by specifying threshold values for the corresponding contact angles at which they form. These films and layers are only notional, i.e. there are no volumes associated with them. Hence they are not involved in the saturation or conductance calcula-

tion but they are incorporated when detecting the continuity of different phases and computing relative permeabilities. In our new model, as will be discussed in chapter 3, these films and layers have volumes based on the precise shape of the pore cross-section. Therefore they contribute to both saturation and conductance (i.e., relative permeability) calculations. It was assumed that pores can be filled by more than one fluid. Gravitational effects were also included. A key feature of the model by van Dijke et al. (2004b, 2006) was the implementation of multiple displacements. This is an extension of the double displacement process discussed by Øren and Pinczewski (1995) and Fenwick and Blunt (1998b). Multiple displacements occur when the injection of one fluid at the inlet of a network model triggers a chain of displacements that involves disconnected clusters of oil, water or gas, which span a connected displacement path from the inlet to the outlet. Such displacement mechanisms were observed in micromodel experiments (Sohrabi et al., 2000, 2001, 2004). This is an important feature when wetting films are absent as the latter reduces the phase connectivity and forms disconnected clusters that can be mobilised only by multiple displacements. The model was used to simulate the micromodel experiments of higher WAG floods for water-wet, oil-wet and mixed-wet systems (Sohrabi et al., 2000, 2001, 2004). The comparisons with the experiments were based on oil recovery and three-phase fluid distributions for the oil-wet WAG micromodel experiments, although the oil recovery was different (Fig. 1.10). The importance of the multiple displacements mechanism for predicting trapping and remobilisation of gas and oil was apparent throughout the simulations. We will use the same experimental data to validate our model in chapter 5.

Svirsky et al. (2007) used the model of van Dijke et al. (2004b, 2006) to predict the experimental three-phase relative permeability data for water-wet systems. They used experimental data for water-wet Berea sandstone of Oak (1990). The network was anchored to the two-phase relative permeability and capillary pressure by tuning the relevant network parameters and then simulating the gas injection to generate three-phase relative permeability. A reasonable prediction was achieved. The model was used to examine the behaviour of the flow functions for two different combinations of interfacial tensions, so-called immiscible and near miscible cases, and different wetting conditions. Immiscible and near miscible cases generated two different saturation paths, which was attributed

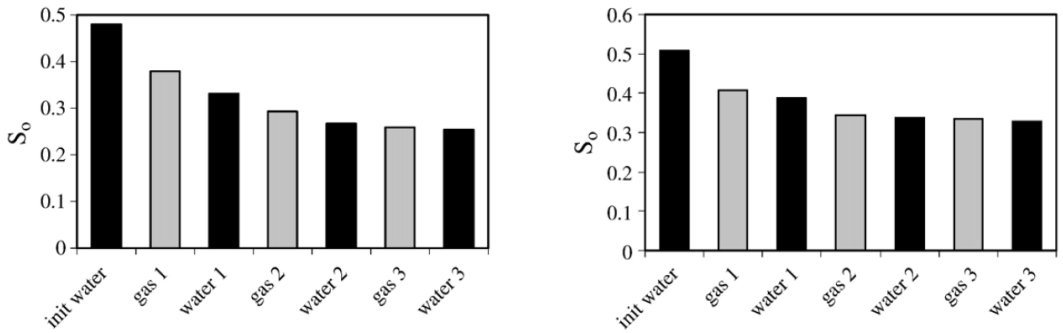

(a) (b)

Figure 1.10: Oil saturation after the three WAG floods starting with water injection for oil-wet system obtained by (a) Micromodel experiment (Sohrabi et al., 2004) (b) Pore-network simulation (van Dijke et al., 2006).

to the presence and absence of oil-spreading layers. It was observed that for different combinations of interfacial tensions, the corresponding relative permeabilities are identical along identical saturation paths.

Piri and Blunt (2005a,b) developed a 3D pore-network model for capillary dominated processes. The model was able to take as input the equivalent network extracted from a real pore space, comprising a network of pores connected by throats. Circular, square, or triangular cross-sections were assigned to each pore, or throat, of the network based on the shape factor that matches the real pore shape (Mason and Morrow, 1991). Wettability alteration, wetting films, spreading layers of the intermediate-wet phase and hysteresis were incorporated in the model. The model included a very detailed description of the fluid configurations for two- and three-phase flow. Double displacements, layer formation and layer collapse were also implemented. Experimental data for three-phase relative permeability for a water-wet Berea sandstone (Oak, 1990), was used to validate the model. A good match between predicted and measured relative permeabilities was observed. More rigorous approach was then used to track the saturation paths of the experiments, point by point, by injecting small slugs of oil, water and gas. However, the model overpredicted the relative permeability of the intermediate wetting phase (oil). This was attributed to the simple geometric criterion that was used to model the formation and collapse of oil layers. It was found that the oil relative permeability is very sensitive to the oil layer conductance (Fig. 1.11). Simulations were ran using secondary and tertiary gas injections. The oil relative permeability during tertiary gas injection was found

to be lower than in the secondary case. This was because oil-water capillary pressure was low during tertiary gas injection. This leads to thinner and less stable oil layers compared to secondary gas injection. An approximate quadratic equation was obtained for the oil relative permeability at low oil saturation (see Fig. 1.4) during secondary gas injection. This was interpreted as oil layers dominating flow at low saturation. Two wetting systems, oil- and water-wet, were used to study the effects of wettability on relative permeabilities. Different two-phase and three-phase relative permeabilities were obtained for different wetting systems.

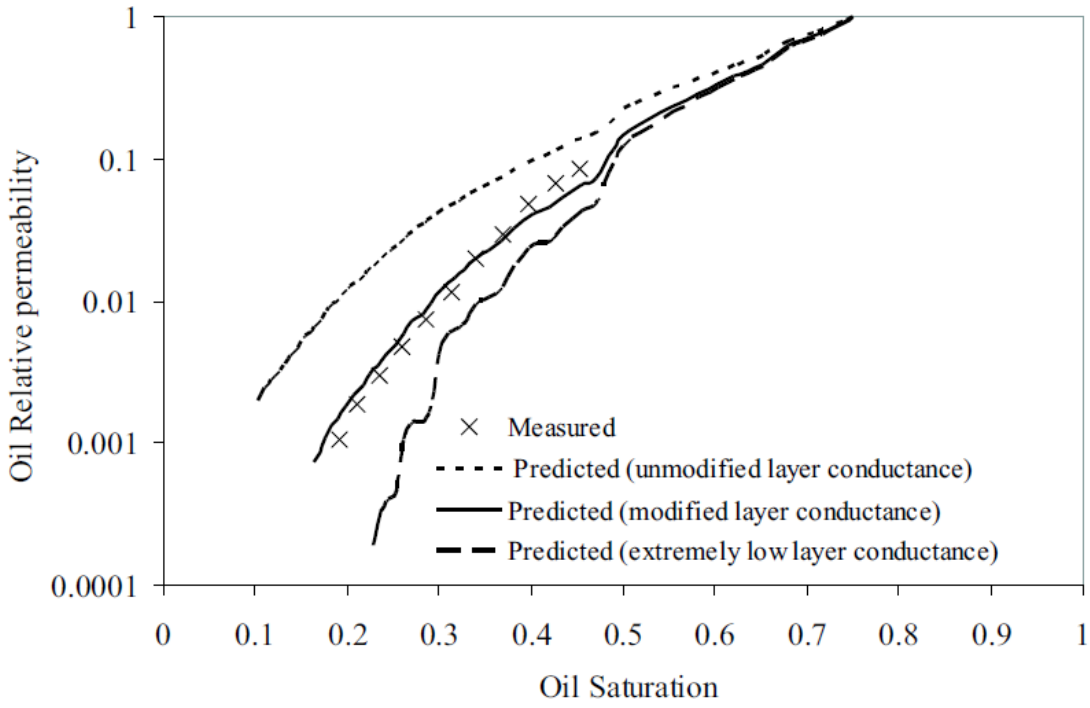

Figure 1.11: Sensitiviy of oil relative permeability to oil layer conductance (Piri and Blunt, 2005b) by comparing measured and predicted three-phase oil relative permeabilities for the experiments by Oak (1990). The dotted line denotes the the predicted relative permeability by Piri and Blunt (2005b), the solid line was obtained by multiplying the oil conductance by a constant factor of 0.08 and the dashed line was obtained by multiplying the oil conductance by a constant factor of 0.001.

Suicmez et al. (2006, 2007) extended the thee-dimensional three-phase network model of Piri and Blunt (2005a,b) by adding two new double displacement mechanisms for a water-wet system: double imbibition (water→oil→gas) and imbibition-drainage (water→gas→oil). The model was further validated using additional experimental datasets from Oak (1990), Egermann et al. (2000) and Element et al. (2003). The first dataset was previously used by Piri and Blunt

(2005b). However, in this work, both simultaneous and cyclic gas-water injection experiment were simulated. The water relative permeability prediction was excellent. However, the oil relative permeability at low oil saturation was underestimated. This result was different from that obtained by Piri and Blunt (2005b) who overestimated the oil relative permeability during gas injection. In both cases, at low oil saturation the oil relative permeabilities were controlled by oil layer flow.

Piri and Blunt (2005a,b) and Suicmez et al. (2006, 2007) illustrated that it is important to model oil layer conductance accurately to obtain adequate estimate of oil relative permeability. In our model we overcome this problem by modelling the oil layers based on a novel thermodynamic criterion for the formation and collapse of oil layers in pores with angular cross-sections, introduced by van Dijke et al. (2004a, 2007). The criteria was derived using an extension of the MS-P method of Mayer and Stowe (1965) and Princen (1969a,b, 1970) to three-phase flow. Such criteria allows for adequate modelling of layer flow of oil, which affects the oil relative permeability at low oil saturation. We will discuss this in more details in chapter 4.

Nardi et al. (2009) developed a three-phase network model, which can use networks extracted for 3D digital rocks. The model incorporated wettability alteration, hysteresis, oil spreading layers and true three-phase capillary entry pressures. It was assumed that water is hydraulically connected everywhere in the pore-network. Hence, only single and double displacements are considered. The model was used to predict two experimental datasets: The data for Berea sandstone from Oak (1990) and the data for composite core material from the Statfjord field reported by Petersen et al. (2008). In general, the predicted three-phase relative permeabilities were in fair agreement with the corresponding experimental three-phase relative permeabilities. The authors suggested that the implementation of a saturation path tracking algorithm is needed for a more comprehensive validation of the model.

Table 1.1 gives a summary of previous three-phase pore-networks which were discussed in this chapter.

Table 1.1: Summary of three-phase pore-network models.

Reference	Network	Compute	F/L	Comment
Heiba et al. (1984)	Cayley	P_c, k_r	–	water-wet systems
Soll and Celia (1993)	3D regular	P_c	F	-
Øren et al. (1994)	2D regular	P_c	F	strongly water-wet systems
Pereira et al. (1996)	2D regular	P_c	F/L	strongly water-wet and oil-wet
Mani and Mohanty (1997, 1998)	3D cubic lattice	P_c, k_r	F/L	–
Fenwick and Blunt (1998a,b)	3D cubic lattice	P_c, k_r	F/L	–
Laroche et al. (1999a,b)	2D or 3D lattice	P_c	F	–
Hui and Blunt (2000a,b)	capillary bundle	P_c, k_r	F/L	–
Lerdahl et al. (2000)	realistic 3D (Berea sandstone)	P_c, k_r	F/L	the first to simulate three-phase flow in a realistic pore network
Larsen et al. (2000)	regular cubic lattice	P_c, k_r	F/L	–
van Dijke et al. (2000, 2001a,b)	capillary bundle	P_c, k_r	–	introduce the linear relationships, see chapter 2
van Dijke et al. (2004b, 2006)	regular 3D	P_c, k_r	F/L^*	*only notional
Piri and Blunt (2005a,b)	realistic 3D (Berea sandstone)	P_c, k_r	F/L	–
Nardi et al. (2009)	realistic 3D	P_c, k_r	F/L	–

where

F implementation on corner films

L layers separating corner films and bulk phase that occupying the centre part of the pore

k_r relative permeabilities

P_c capillary pressures

1.5 STRUCTURE OF THE THESIS

This thesis is divided into two mutually connected parts: The first part relates to the pore-scale simulation and comprises the description of the fundamental three-phase physics at the pore-scale, resulting in a new pore-network model. The second part demonstrates the capability of the pore-scale network model to derive flow functions that can be used to predict three-phase flow processes at a larger scale. Different injection scenarios are simulated at the macro-scale. In total, this thesis consists of 8 chapters.

Chapter 1: This is the current chapter in which we showed the importance of the three-phase flow processes, in particular WAG injection, in the oil and gas industry. The physics of the three-phase flow that lead to an increase in oil recovery as result of WAG injection are still not well-understood. We propose using pore-network modelling as a physically-based simulation tool to explore the behaviour of three-phase flow at the pore-scale and for subsequent "predictions" of three-phase flow functions. We also reviewed the previous three-phase models and their limitations.

Chapter 2: Here we describe the fundamental physics of three-phase flow, most notably, the two physical properties which control the three-phase fluid configuration at equilibrium conditions. This includes the interfacial tensions of three coexisting phases. They are used to determine the spreading coefficient and the three-phase contact angles, which decide the wetting state of the system: water-wet or oil-wet.

Chapter 3: Here we discuss the shape of the real pores, demonstrating the importance of angular pore shapes to model key pore-scale physics like the oc-

currence of films and layers, which influence three-phase flow behaviour. We also introduce the pore networks which are used in this study. We then provide the calculations of conductance, porosity, phase saturations, absolute permeability and relative permeability.

Chapter 4: Here we give a detailed description of the pore-network model, discussing the two most important advancements in the current model: A thermodynamic criterion for oil layer formation and collapse and multiple displacement chains.

Chapter 5: Here we validate our pore-network model against experimental data for different wetting systems. For a water-wet system, we match our simulations with landmark experimental data of Oak (1990). We demonstrate the impact of implementing the thermodynamic criteria for oil layer formation and collapse by comparing predictions from our model and the well-known network model of Piri and Blunt (2005a,b) to the experimental data. For an oil-wet system, we simulate the micromodel experiments that were conducted by Sohrabi et al. (2001, 2004). The simulation results are compared with the experimental data quantitatively, using the oil recovery profile, and qualitatively, using fluid distributions. We also compare our model prediction with previously published results for the pore-network model developed by van Dijke et al. (2006).

Chapter 6: Here we use realistic 3D pore-networks, representing sandstone and carbonate rocks, to show the capability of our new model to compute the relative permeabilities for different wetting systems. We study the emergent behaviours and resulting flow properties of the networks and wetting systems. We compare the saturation paths between two runs, using single- and multi-displacement. The impact of these implementations on the residual oil saturation is discussed.

Chapter 7: Here we show how the flow functions derived from our pore-network model can be used in a commercial reservoir simulator. We use our network model to derive physically consistent capillary pressure and relative permeability functions for two- and three-phase flow. These functions are im-

plemented into a commercial field-scale simulator to model WAG injection. We study different processes, including the impact of pore-scale generated three-phase flow functions on recovery rates in oil reservoirs, the efficiency of WAG injection in reservoirs of different wettability.

Chapter 8: Here we summarise the results of this work and provide the key conclusions. We also give some recommendation for future work.

Part I

THREE-PHASE PORE-SCALE NETWORK MODELING

In this part we introduce our newly developed state-of-the-art three-phase flow pore-network model, demonstrating the key advancements of our model over the existing three-phase pore-network models. These comprise the implementation of a novel thermodynamic criterion for the formation and collapse of, oil layers and the multiple displacements mechanisms of disconnected phase clusters which were observed by micromodel experiments. We explain the local theory of these processes which were worked out some time ago by van Dijke et al. (2004a, 2007) in Institute of Petroleum Engineering. We describe the pore space structure of the networks. We validate the model against the well-known experimental data conducted by Oak (1990) and the micromodel experiments of Sohrabi et al. (2000, 2001, 2004). Finally, we run simulations using full 3D pore-networks for sandstone and carbonate rocks for different wettability systems.

2

FUNDAMENTALS OF THREE-PHASE PHYSICS

2.1 INTRODUCTION

Two main physical properties are required to describe the three-phase fluid configuration in a porous medium at equilibrium conditions. The first property is the interfaical tension between each of the three fluid pairs when the three phases coexist. These interfacial tensions are different from the corresponding two-phase systems (Zhou and Blunt, 1997). The three-phase interfacial tensions are used to determine an important feature of three-phase physics which is the ability of one fluid to spread over the other in the presence of a third fluid in the system, expressed by the spreading coefficient. This is a crucial concept that affects the residual oil saturation (Mani and Mohanty, 1997) and thus employing realistic values of interfacial tensions is essential. The second property is the three-phase contact angle between each of the three fluid pairs when the three phases coexist. This decides the wetting order of the phases in the presence of a solid surface. The contact angle is defined as the angle that the fluid-fluid interface between the two fluids makes with the solid surface, usually measured through the denser fluid. In this chapter, we give a background of these two physical properties and other parameter which can be determined from them.

2.2 INTERFACIAL TENSIONS AND SPREADING COEFFICIENTS

The spreading coefficient can be calculated by taking into account the force balance of the contact line where all three phases (oil, water and gas, labeled o, w, and g, respectively) meet. The important quantities which are required to cal-

culate the spreading coefficient are the interfacial tensions, σ_{go}, σ_{ow} and σ_{gw}. If each of the interfacial tensions was measured for a pair of fluids in the absence of the third fluid (i.e. two-phase system), then the spreading coefficient $C^i_{s,o}$ can be given in Eq. 2.1 which defines the initial oil spreading coefficient (Adamson and Gast., 1997). However, if these interfacial tensions were measured when all fluid phases are present in the system (i.e. three-phase system), they would be different from the corresponding two-phase systems (Zhou and Blunt, 1997). If the fluids remain in contact for a sufficient period of time to reach thermodynamic equilibrium, then a new spreading coefficient, called the equilibrium oil spreading coefficient $C^{eq}_{s,o}$ can be defined by Eq. 2.2 (Adamson and Gast., 1997).

$$C^i_{s,o} = \sigma_{gw} - \sigma_{go} - \sigma_{ow}. \tag{2.1}$$

$$C^{eq}_{s,o} = \sigma^{eq}_{gw} - \sigma^{eq}_{go} - \sigma^{eq}_{ow}, \tag{2.2}$$

where σ^{eq}_{gw}, σ^{eq}_{go} and σ^{eq}_{ow} denote the interfacial tensions at thermodynamic equilibrium for gas-water, gas-oil and oil-water, respectively.

In the absence of a solid surface, the three-phase systems can be divided into three groups (Piri, 2003), shown in Fig. 2.1:

(a) A non-spreading system, where a blob of oil floats on the surface of water. In this case all three fluids in the system are in contact with each other and, therefore, there are contact lines where all three fluids meet. At the contact lines the interfacial tensions balance. For this system, the initial spreading coefficient is negative.

(b) A partially spreading system, where the initial spreading of oil over water takes place to form a thin film of oil covering the surface of the water. This is possible when the initial spreading coefficient is positive and the equilibrium spreading coefficient is positive.

(c) A spreading system, where a layer of oil spreads between water and gas. Any addition of oil to the system leads to a thickening of the oil layer. In

this system, the initial spreading coefficient is positive and the equilibrium spreading coefficient is close to zero.

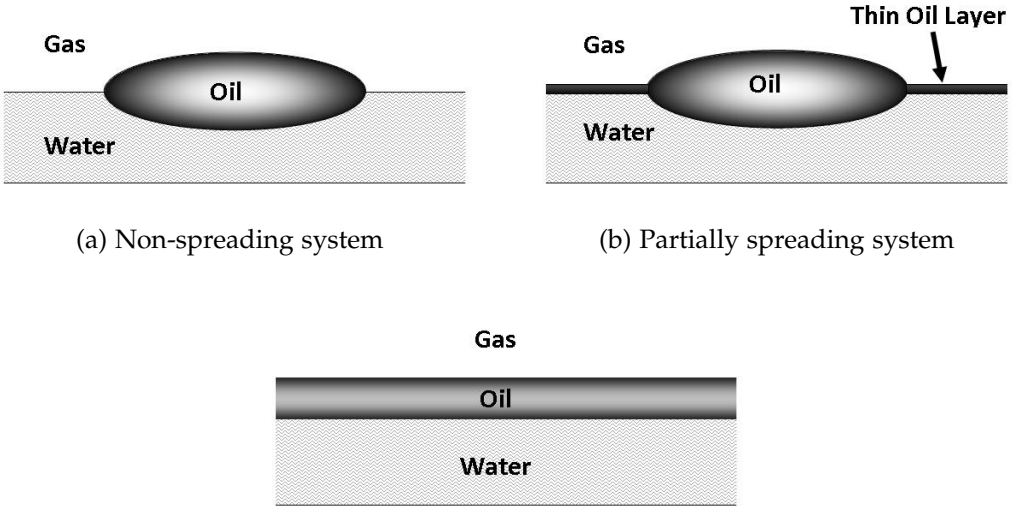

(a) Non-spreading system

(b) Partially spreading system

(c) Spreading system

Figure 2.1: Classification of spreading systems.

In addition to the oil spreading coefficient (Eq. 2.2), the equilibrium spreading coefficient for each of the remaining two fluids are defined as:

$$C_{s,w}^{eq} = \sigma_{go}^{eq} - \sigma_{gw}^{eq} - \sigma_{ow}^{eq}. \tag{2.3}$$

$$C_{s,g}^{eq} = \sigma_{ow}^{eq} - \sigma_{go}^{eq} - \sigma_{gw}^{eq}. \tag{2.4}$$

From Eqs. 2.2–2.4 it is clear that only one spreading coefficient can be positive or zero at any time and, therefore, there is only one fluid that may spread as a layer between the other two. Considering realistic values of the interfacial tensions for oil, water and gas systems in oil reservoirs, only the oil spreading coefficient is normally non-negative, $C_{s,o} \geq 0$. However, Rowlinson and Widom (1989) showed that at thermodynamic equilibrium, spreading coefficients cannot be positive. Based on this, oil will spread only if $C_{s,o} = 0$.

It is well-known that the properties of oil and gas become very similar at high pressure (i.e. a near miscible system) such as high pressure high temperature

(HT-HP) reservoirs. Moreover, during the production phase, the reservoir pressure could either increase or decrease, depending on the balance between the production rate and injection rate of the reservoir. The water-wet micromodel experiment of Mackay et al. (1998) showed that the value of σ_{go} decreases with increasing pressure (Fig. 2.2) until it reaches zero at bubble point pressure. Amin and Smith (1998) studied the effect of pressure and temperature on interfacial tension. The measured data of the three-phase interfacial tension and the corresponding oil spreading coefficient as a function of pressure are shown in Figs. 2.3 and 2.4, respectively. These data show that σ_{gw} is most sensitive to a pressure change. At low pressure, the oil spreading coefficient is positive. As the pressure increases, σ_{gw} decrease whereas σ_{ow} increases slightly until they become equal, indicating that oil and gas have similar properties (i.e. are miscible). These interfacial tensions will be related to the contact angles in section 2.3.

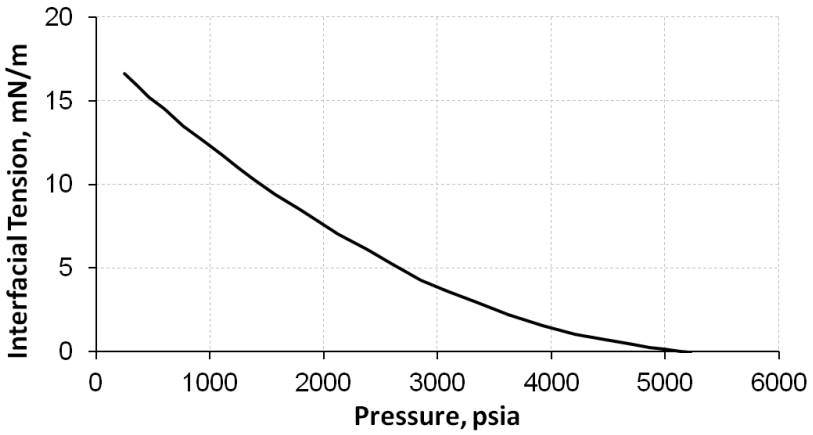

Figure 2.2: The variation of gas/oil interfacial tension with pressure for the C1-nC10 mix (Mackay et al., 1998).

In this study, we always assume that the interfacial tensions are taken at thermodynamic equilibrium, including the effects of any wetting and spreading films or layers that may be present in the system. Unless other values of interfacial tensions are stated, we use the values for three-phase fluid system of air/water/hexane (Hui and Blunt, 2000b) in our pore-scale simulations. The interfacial tensions values of this system are shown in Table 2.1.

Table 2.1: Interfacial tensions which are used in this work (Hui and Blunt, 2000b).

System	σ_{go} (mN/m)	σ_{ow} (mN/m)	σ_{gw} (mN/m)
Hexane	19	48	67

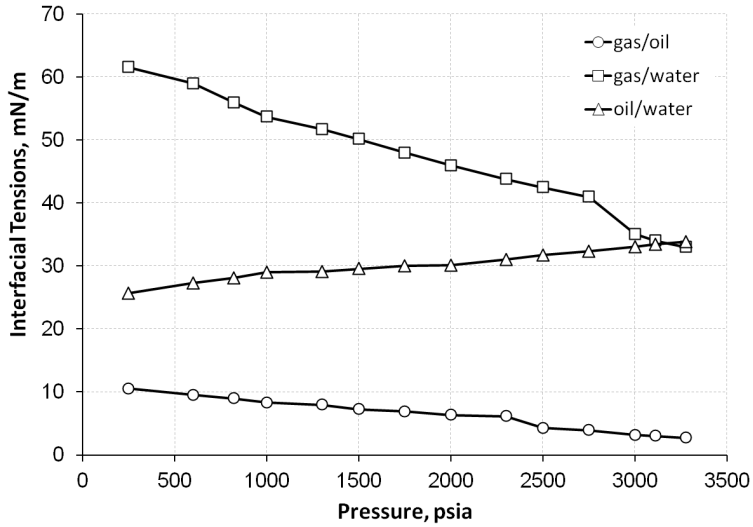

Figure 2.3: Measured data of the three-phase interfacial tension as a function of pressure at reservoir conditions (Amin and Smith, 1998).

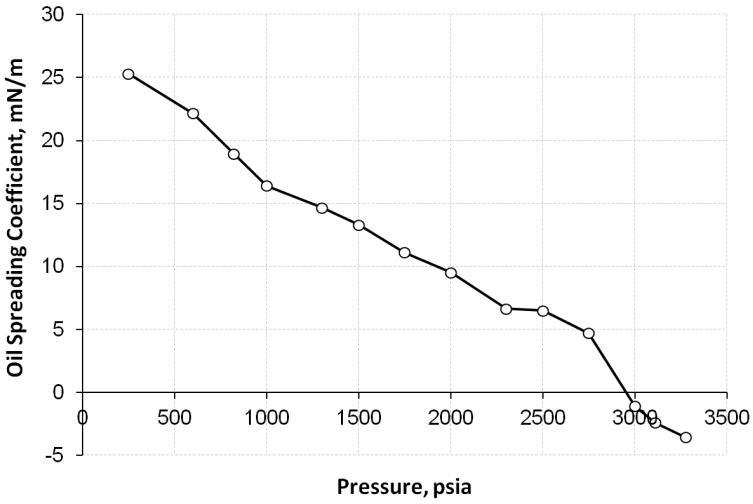

Figure 2.4: The corresponding oil spreading coefficient as a function of pressure at reservoir conditions (Amin and Smith, 1998).

2.3 CONTACT ANGLES AND WETTABILITY ALTERATION

The ability of oil or water to form wetting films on a solid determines the wettability of the surface (Laroche et al., 1999a), depending on the value of the oil-water contact angle (θ_{ow}). In a three-phase system, Young's equation (2.5) describes the horizontal force balance of the three pairs of fluids in the presence of a solid surface (Fig. 2.5).

$$\sigma_{os} = \sigma_{ws} + \sigma_{ow} \cos\theta_{ow}. \tag{2.5a}$$

$$\sigma_{gs} = \sigma_{ws} + \sigma_{gw} \cos\theta_{gw}. \tag{2.5b}$$

$$\sigma_{gs} = \sigma_{os} + \sigma_{go} \cos\theta_{go}. \tag{2.5c}$$

These three equations can be combined, by eliminating the fluid-solid interfacial tensions (σ_{ws}, σ_{os} and σ_{gs}), to one equation (Eq. 2.6), called the Bartell-Osterhof equation (Bartell and Osterhof, 1927; Johnson and Dettre, 1993; Zhou and Blunt, 1997).

$$\sigma_{gw} \cos\theta_{gw} = \sigma_{ow} \cos\theta_{ow} + \sigma_{go} \cos\theta_{go}. \tag{2.6}$$

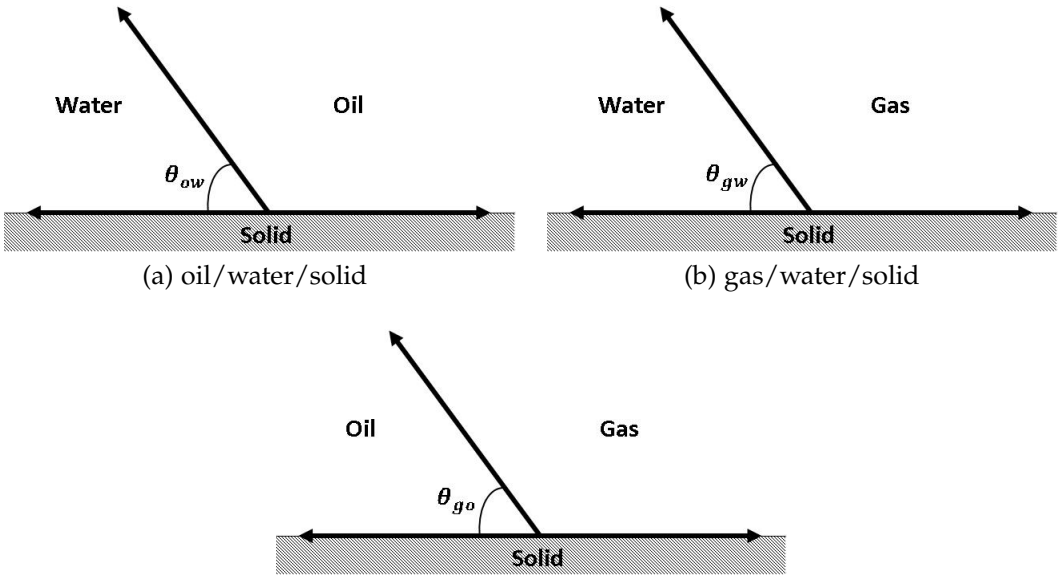

(a) oil/water/solid

(b) gas/water/solid

(c) gas/oil/solid

Figure 2.5: Force balances of three two-phase systems in the presence of solid surface.

The Bartell-Osterhof equation includes the three-phase contact angles and interfacial tensions. This equation requires two of the fluid-fluid contact angles to be known in order to calculate the third one. van Dijke and Sorbie (2002) pro-

posed linear relationships (Fig. 2.6) to find $\cos\theta_{go}$ and $\cos\theta_{gw}$ for a given $\cos\theta_{ow}$ and given interfacial tensions:

$$\cos\theta_{go} = \frac{1}{2}\left\{\left(-1+\frac{\sigma_{gw}-\sigma_{ow}}{\sigma_{go}}\right)\cos\theta_{ow}+1+\frac{\sigma_{gw}-\sigma_{ow}}{\sigma_{go}}\right\}. \tag{2.7a}$$

$$\cos\theta_{gw} = \frac{1}{2}\left\{\left(1-\frac{\sigma_{go}-\sigma_{ow}}{\sigma_{gw}}\right)\cos\theta_{ow}+1+\frac{\sigma_{go}-\sigma_{ow}}{\sigma_{gw}}\right\}. \tag{2.7b}$$

These linear relationships satisfy the Bartell-Osterhof equation. Moreover, Eq. 2.7b has recently been validated experimentally by Grate et al. (2012).

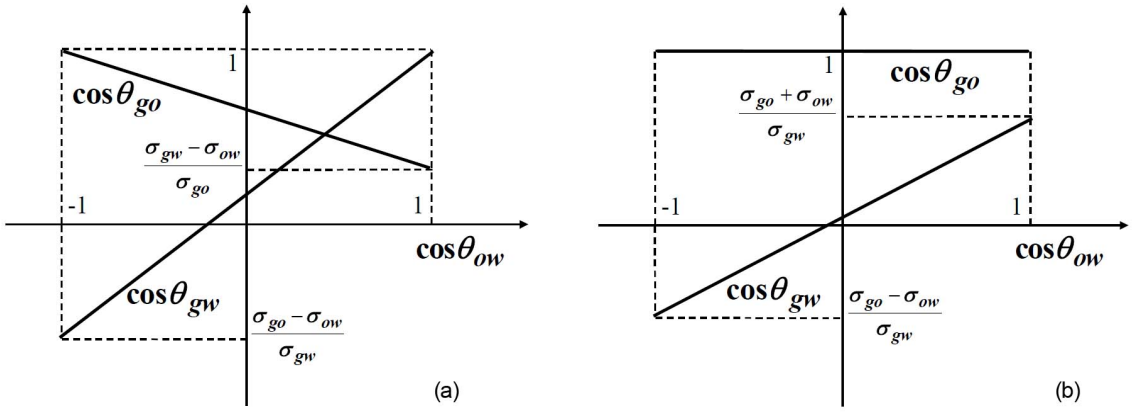

Figure 2.6: Linear relationships proposed by van Dijke and Sorbie (2002), showing $\cos\theta_{go}$ and $\cos\theta_{gw}$ as functions of $\cos\theta_{ow}$ for (a) a nonspreading oil and (b) a spreading oil.

In an oil-water two-phase system, depending on the contact angle of oil/water, the system could be either water-wet ($\theta_{ow} < \frac{\pi}{2}$) or oil-wet ($\theta_{ow} > \frac{\pi}{2}$). In the three-phase system, the wettability can be indicated by the wetting order, which defines the three phases as: wetting phase, intermediate phase and non-wetting phase. For instance, generally, in a strongly water-wet system ($\theta_{ow} \approx 0$), water is the wetting phase, oil is the intermediate wetting phase and gas is the non-wetting phase. The linear relationships (Eqs. 2.7) define the wetting order of gas relative to oil (based on the sign of $\cos\theta_{go}$, Eq. 2.7a) and gas relative to water (based on the sign of $\cos\theta_{gw}$, Eq. 2.7b). Mathematically, there are six wetting orders that are possible in any three-phase system, starting from the most to the least wetting phase: water-oil-gas , water-gas-oil , oil-water-gas, oil-gas-water, gas-water-oil and gas-oil-water. However, general values of three-phase interfa-

cial tensions imply that only three out of the six wetting orders are possible: water-oil-gas, oil-water-gas and oil-gas-water.

McDougall and Sorbie (1995) classified the wettability of any porous rock to be either: (1) Uniform wettability, where the entire rock surface has the same wettability (i.e. 100% water-wet, 100% oil-wet or 100% intermediate-wet) with constant contact angles throughout the system; or (2) Non-uniform wettability, where the pore space has heterogeneous wettability in a way that the wettability can vary from pore to pore throughout the network. The authors subdivided non-uniform wettability into two subclasses: fractional wettability and mixed wettability. In fractionally-wet rock, pores of any size can be oil-wet. In mixed wettability, a fraction of either the largest pores or the smallest pores are considered to be oil-wet whereas the remaining fraction remains water-wet. The authors mentioned about the wettability heterogeneity at sub-pore level (i.e. different wettability within one pore) but they did not consider it in their study.

Generally, the wettability of oil reservoirs are not completely water-wet or oil-wet (Willhite, 1986). This is because direct contact of oil with the (mineral) surfaces of the pores leads to an alteration of the wettability of the contacted regions. Pores often display non-uniform wettability when both water-wet and oil-wet surfaces are present. Kovscek et al. (1993) introduced a model that accounts for the wettability alteration as result of direct contact of oil with the solid surface. The porous medium is assumed to be initially water-saturated, implying a strongly water-wet system (Fig. 2.7a). When oil invades the system, it fills the central part of the (large) pores (Fig. 2.7b). However, thin wetting films of water, covering the solid surface, prevent oil from contacting the surface. Such wetting films were observed by electron microscopy (Robin et al., 1995). These films may collapse at a given threshold capillary pressure, allowing oil to touch the solid surface and alter the wettability of the contacted regions only. This means that within one pore, two surfaces of different wettability are present and the pore is said to display non-uniform wettability (Fig. 2.7c). We refer to this process of wettability alteration as "ageing" and it is modelled by changing the oil-water contact angles of the altered surface. Additionally, the real pore surfaces are normally rough. This causes the contact angle to vary, depending on which phase displaces which (Morrow, 1975), i.e. on the direction of the displacement. This phenomenon is known as contact angle hysteresis. There are generally two

types of contact angles: advancing contact angles where the more wetting phase invades the less wetting phase; and receding contact angles where the less wetting phase invades the more wetting phase. For rough surfaces, the advancing contact angle is bigger than the receding contact angle (Morrow, 1975). Therefore, we assign up to 12 contact angles for each pore as summarised in Table 2.2, depending on the wettability of the pore and the direction of the displacement.

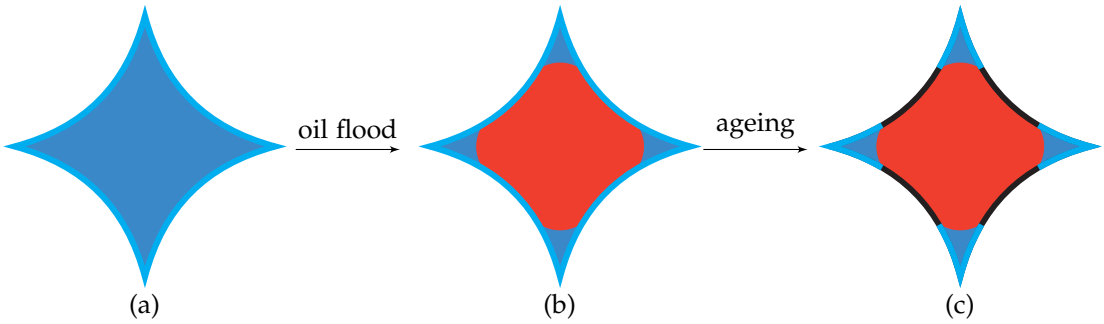

Figure 2.7: Primary drainage (oil flood) and wettability alteration in a pore with corners. (a) The pore is completely filled with water, implying water-wet pore surfaces (i.e. thin wetting films of water, covering the solid surface). (b) Oil displaced water from the centre of the pore, leaving water to reside at the corners. (c) The wettability of the oil contacted surfaces is changed, rendering the pore to non-uniform wettability. Blue denotes water, red denotes oil, blue lines denote water-wet (unaltered wettability) surfaces and black lines denote altered wettabiliy surfaces.

Table 2.2: Possible contact angles assigned for each pore

SURFACE WETTABILITY	ADVANCING (a)			RECEDING (r)		
Unaltered wettability (e.g. water-wet (w))	$\theta^w_{go,a}$	$\theta^w_{ow,a}$	$\theta^w_{gw,a}$	$\theta^w_{go,r}$	$\theta^w_{ow,r}$	$\theta^w_{gw,r}$
Altered wettability (e.g. oil-wet (o))	$\theta^o_{go,a}$	$\theta^o_{ow,a}$	$\theta^o_{gw,a}$	$\theta^o_{go,r}$	$\theta^o_{ow,r}$	$\theta^o_{gw,r}$

In this study, we use the linear relationships (Eq. 2.7) to find the three-phase contact angles. Additionally, we consider "realistic" values of the interfacial tensions that may represent the spreading behaviour of the system in oil reservoir (Table 2.1). The network model can assign both receding and advancing contact angles (Table 2.2). However, in this study we use single values for each of the contact angles (i.e. advancing and receding contact angles are the same on a given wetting surface). Therefore, we drop the subscripts "a" and "r" for simplicity.

2.4 SUMMARY AND CLOSING REMARKS

In this chapter, we have explored the physical properties that control the behaviour of three fluid phases when they coexist. In the absence of a pore or solid surface, the three-phase systems are categorised into three groups (Fig. 2.1): (1) Non-spreading system, where a blob of oil floats on the surface of water. (2) Partially spreading system, where a thin film of oil covering the surface of the water, representing an initial spreading of oil over water. (3) Spreading system, where a layer of oil spreads between water and gas. At thermodynamic equilibrium, spreading coefficients cannot be positive and oil spreads between water and gas only if $C_{s,o} = 0$. The three-phase contact angles and interfacial tensions appear in one equation, called the Bartell-Osterhof equation. Linear relationships are used to calculate $\cos\theta_{go}$ and $\cos\theta_{gw}$ for a given $\cos\theta_{ow}$ and given interfacial tensions. These linear relationships satisfy the Bartell-Osterhof equation and have been partially validated experimentally. Oil reservoirs are usually not completely water-wet or oil-wet, but a mixture of both. At the microscopic scale, pores with non-uniform wettability, where there are water- and oil-wet regions, are commonly found. This is because of the direct contact of oil with the solid surface, causing an alteration in the surface wettability towards more oil-wet conditions.

In the next chapter, we will describe the pore space structure, including geometrical characterisation of the pores. This will enable us to implement the three-phase physics which was described in this chapter.

3

STRUCTURE OF THE PORE SPACE AND INTRA-PORE PROPERTIES

3.1 INTRODUCTION

Accurate prediction of the flow properties for a given reservoir relies on accurate representation of porous medium. In pore-network modelling, pore-networks are used to represent the microstructure of porous media. These pore-networks consist of pore bodies (nodes) connected by pore throats (bonds). Each pore is assigned a regular shape, e.g. n-cornered star, triangle, square or circle (Ryazanov et al., 2009). This allows easy analytical calculation of the intra-pore flow properties such as capillary entry pressures. The pore-networks are commonly extracted from 3D digital images of porous media. The extraction and reconstruction methods of pore-networks are well documented (e.g. Lindquist et al., 1996; Øren et al., 1998; Delerue and Perrier, 2002; Silin et al., 2004; Al-Kharusi and Blunt, 2007; Jiang et al., 2007). However, we briefly review these methods for completeness. There are two methods to obtain the 3D digital image of pore space: (1) Computed tomography (CT) imaging of core samples. In this approach, the 3D digital rock is obtained by using computed X-Ray tomography with a resolution ranging from few microns (Dunsmuir et al., 1991) to sub-microns (Coenen et al., 2004). (2) Using 2D thin sections to reconstruct the 3D digital rock. This approach requires 2D thin section images which can be obtained, for example, by Scanning Electronic Microscope (SEM) and then using common 3D pore space reconstruction methods. The latter is widely done by two ways: (a) Process-based algorithms: these algorithms are based on the concept of linking the the formation of pore structure with the physical process. They use petrographical data

(e.g. grain size distribution) from 2D thin sections to reconstruct 3D digital rocks (Bakke and Øren, 1997; Øren and Bakke, 2002, 2003). (b) Statistical methods: the statistical properties (e.g. porosity) are determined from 2D thin section images. Then 3D digital rocks are generated that capture the statistical properties 2D thin section images (Wu et al., 2006).

Once the 3D digital rocks are obtained, different types of algorithms can be used to extract pore-networks which are topologically and geometrically equivalent. Examples of these algorithms are: (1) Medial axis based algorithm: Here, the digital pore space is reduced to the topological skeleton of the pore-network, followed by pore space partitioning which is used to identify the pore bodies (nodes) and pore throats (bonds) (Lindquist et al., 1996; Lindquist and Venkatarangan, 1999; Sheppard et al., 2005, 2006; Jiang et al., 2007). (2) Maximum ball based algorithm: This algorithm distinguishes between the pore bodies and pore throats by defining a maximum ball for each void voxel of the 3D image. The largest balls are considered to be the pore bodies whereas the set of the smallest balls, which overlap each other and that form a connected path/link between two largest balls, are considered to be pore throats. The algorithm also establishes volumes and connectivity of the bonds and nodes (Silin et al., 2003; Silin and Patzek, 2006). (3) Voronoi diagram: This algorithm uses Voronoi tessellation to extract the skeleton of the pore-network from known coordinates of all grain centres, which are provided by a process-based algorithm for reconstructing the 3D digital rock (Bryant and Blunt, 1992; Bryant et al., 1993a,b; Øren and Bakke, 2003).

Sok et al. (2002) studied the effect of topology on residual saturations by generating stochastic network models with the same geometric (pore-size, throat-size) and topological (coordination number distribution) properties. They derived the two-phase flow properties directly from the network models and their stochastic equivalents. They found that the stochastic networks provided a poor representation of flow properties of two-phase flow on the direct network equivalents. This was attributed to inaccurate topological characterization. They also found that accurate prediction of the residual phase saturations relies heavily on the accuracy of the description of the network topology. Furthermore, Arns et al. (2004) have shown the importance of incorporating realistic 3D topologies to derive accurate flow properties from the network models. They found that using regu-

lar lattice or stochastic networks with identical geometric (pore-size, throat-size) properties of the realistic networks of sandstone cannot reproduce the same flow properties of the latter networks. Therefore, it is crucial to use pore-networks that can preserve the topology of the pore space and the geometrical properties (e.g. inscribed radius, shape factor and hydraulic radius etc.).

In this chapter, we describe the 3D pore-networks that are used in this study to represent sandstone and carbonate rocks. Then we present the real shape characterisation of the pore, showing different shapes of the pore cross-sections that are used to model different realistic fluid configurations in the pore, such as films and layers. The methods for calculating conductance, porosity, phase saturations, absolute permeability and relative permeability of the pore-network are presented in this chapter.

3.2 PORE-NETWORKS

The new three-phase flow network model, which was developed as part of this thesis, takes as input the equivalent network extracted from a real pore space. Table 3.1 presents the types of information of the network that can be read by our model from the input data files, which are properties that are typically extracted for pore-networks (Bakke and Øren, 1997; Øren et al., 1998; Øren and Bakke, 2002). In this study, we use four different realistic 3D pore-networks (Fig. 3.1 and Fig. 3.2) extracted from both sandstone (Network A) and carbonate (Networks B, C and D) rocks for the sensitivity analysis (see chapter 6). These networks have been extracted from pore-space reconstruction methods and CT images, preserving both topology and pore shape of the rock. The key statistics of the networks are given in Table 3.2. In addition, we have generated 2D lattice networks to validate our model against experimental data from an oil-wet micromodel. We will describe these 2D networks in detail in chapter 5. Here we give a brief description of the two types of the realistic 3D networks used in the remainder of this work.

1. Sandstone network (A): This is a widely used pore-network which is extracted from a process based reconstruction of a Berea sandstone (Øren and Bakke, 2003). The pore space image and the extracted network of Berea

Table 3.1: Input network parameters which are obtained by pore-space reconstruction methods (Bakke and Øren, 1997; Øren et al., 1998; Øren and Bakke, 2002) and that can be read by our model and some of the recent pore-network models (Piri and Blunt, 2005a).

Parameters
- Total number of network elements (pore bodies and throats)
- Dimensions of the network (used to calculate the cubic volume of the network, section 3.6)
- Volume of each element (excluding clay volume)
- Clay volume of each element
- 3D coordinates (x, y, z) of each pore
- Inscribed radius (r_{ins}) of each element
- Hydraulic radius (r_h) of each element[1]
- Number of pore(s) connected to each pore
- Indices of pore(s) connected to each pore
- Inlet pores of the network
- Outlet pores of the network
- Index of the throat (bond) connecting two pores
- Shape factor of each element (G)
- Indices of the first and second pores connected to each throat
- Distance between the centres of the two connecting pores
- Length of the first and second pore connecting to each throat
- Length of each throat

[1] if it is given in the input data, cannot be read by other models.

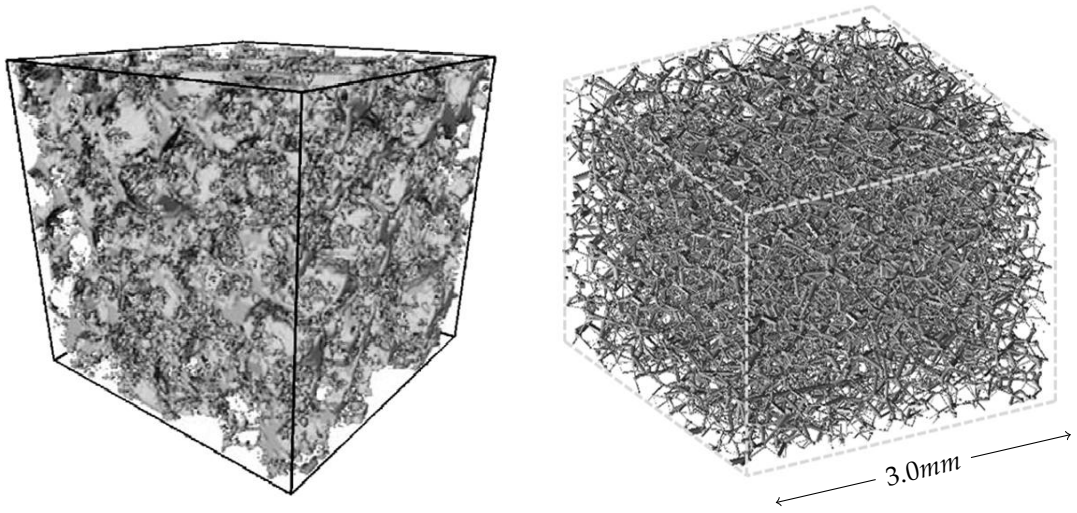

(a) (b)

Figure 3.1: (a) Pore space reconstructed by a process-based approach for a Berea sandstone sample, taken from Øren and Bakke (2003); (b) Network A, Table 3.2, extracted from a process-based Berea sandstone.

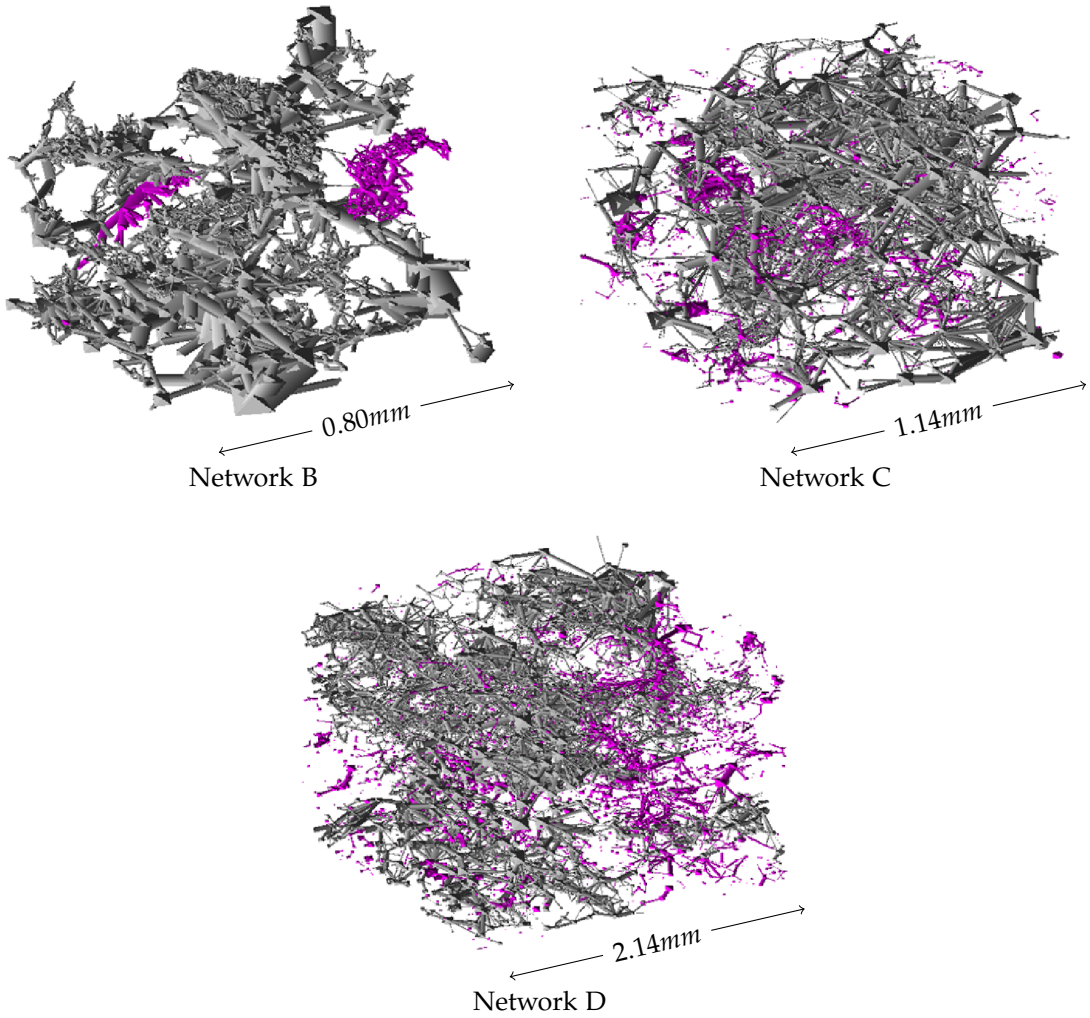

Figure 3.2: Extracted networks for three carbonate samples. Network B was extracted in-house at Heriot-Watt University whereas networks C and D were extracted by Dong and Blunt (2009). Pink regions denote isolated pores.

Table 3.2: Main pore networks parameters

Network	A	B	C	D
Number of Nodes	12349	3698	4576	8508
Number of Bonds	26146	6424	6921	10336
Average Coordination Number	4.19	3.46	2.98	2.37
Permeability, mD	2673	166	570.48	162.25
Net Porosity, %	18.3	15.73	21.25	14.04
Clay Bound Porosity, %	5.72	0.42	1.85	2.28
Formation Volume Factor	15.16	91.72	23.43	84.14
Volume, mm^3	27.0	0.514	1.482	9.772

are shown in Fig. 3.1 and the main parameters of the network are given in Table 3.2. Further details about the data structure for these networks can be found in Bakke and Øren (1997) and Piri and Blunt (2005b). We use

the Berea sample because of the availability of experimental three-phase data for validating our new network model (see chapter 5). This network is homogeneous and well-connected (has high coordination number, Table 3.2). However, its pore structure is less complex than what is commonly encountered in real reservoir rocks.

2. Carbonate networks (B,C,D): These networks are very heterogeneous with poor connectivity (see Table 3.2 and Fig. 3.2). We will use these networks to represent the carbonate rocks in our sensitivity analysis (see chapter 6). Carbonate networks C and D were extracted by Dong and Blunt (2009) from 3D images using the maximal ball algorithm. Carbonate sample B was extracted in-house at Heriot-Watt University (Jiang et al., 2007). A noteworthy feature of these networks is that they contain a small number of pores with large volume ("vugs"). This might affect the results of three-phase flow simulations (see chapter 6). The effect of this feature can be incorporated by using larger pore networks.

3.3 REALISTIC SHAPE CHARACTERISATION OF THE PORE

Many important two- and three-phase flow physics at the pore-scale cannot be modelled without assigning a realistic pore shape. The real pore shapes are irregular (Fig. 3.3a) with many corners that can accommodate a wetting phase (e.g. water) whereas the non-wetting phase (e.g. oil) occupies the centre part of the pore (Lenormand et al., 1983). Moreover, conditionally stable oil layers surrounded by water corner films and bulk water or gas phases could form at the corners. These films and layers contribute to the hydraulic connectivity of the corresponding phases, especially at very low phase saturations, providing pathways for the the phase to escape from the system. One of the limitations of empirical three-phase models (Stone, 1970, 1973) is that they fail to capture the oil relative permeability at very low oil saturations (Blunt, 2000). Therefore, it is essential to characterise the shape of the pore cross section in a "realistic" way by incorporating shapes with corners (e.g. Fig. 3.3).

Mason and Morrow (1991) proposed a parameter called the shape factor (G) that is defined by the cross sectional area (A) of the pore cross-section and its perimeter (L):

$$G = \frac{A}{L^2}, \tag{3.1}$$

where A and L are the area and perimeter of the cross-section, respectively.

The shape factor has been used to formulate the capillary entry pressure for pores with arbitrary triangular cross sections. Øren et al. (1998) and Patzek (2001) used the shape factor to identify the arbitrary triangular shapes of unstructured networks, representing the pore shapes of their pore-space reconstructions. The most common approach for representing the real pore shape is to assign Circle, arbitrary Triangle or Square (C-T-S) shapes to the network pore cross-sections based on shape factor matching (Patzek, 2001; Valvatne and Blunt, 2004; Piri and Blunt, 2005a; Valvatne et al., 2005). Recently, a technique for pore shape characterization was suggested by Joekar-Niasar et al. (2010). It is based on shape factors or a shape factor distribution extracted from input rock images to reproduce a continuous ranges of shape factors.

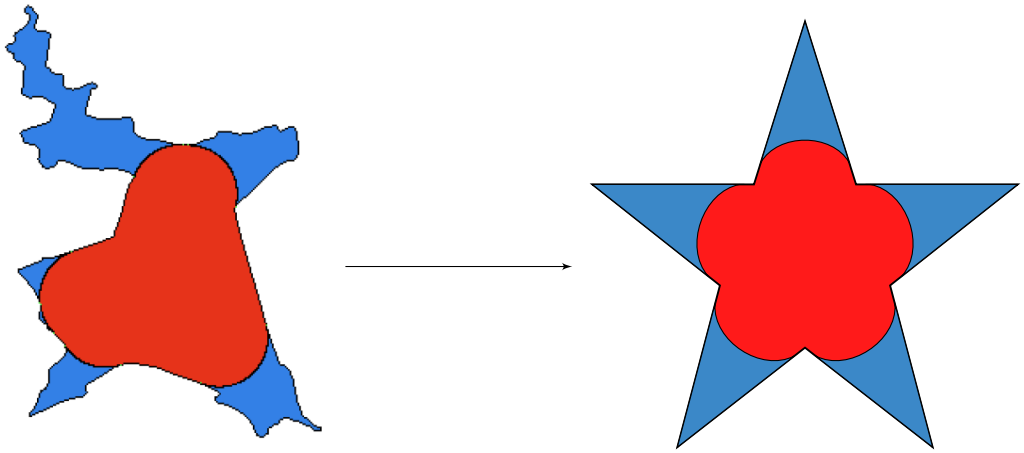

(a) (b)

Figure 3.3: (a) Cross-section of a real pore with irregular shape, accommodating water at the corners and oil at the centre part of the pore, taken from Ryazanov (2011). (b) The star shape approximation for the real pore. Blue denotes water and red denotes oil.

The ratio (known as the dimensionless hydraulic radius H, Eq. 3.2) of the hydraulic radius (R_h) and the inscribed radius (R_{ins}) of the shape cross-section defines its convexity, which divides the types of cross-section into two groups:

1. Convex (C-T-S) shapes, where for every pair of points that fall inside the shape boundary, every point on the straight line segment that connects them lies also within the shape boundary (Fig. 3.4). This is the most common approach to represent the pore cross-section shape based on the shape factor G (Øren et al., 1998; Patzek, 2001; Valvatne and Blunt, 2004):

   - Arbitrary triangle: if $G \leq \frac{\sqrt{3}}{36}$. The half angle values are determined using a special procedure introduced by Øren et al. (1998) and Patzek and Silin (2001).
   - Square: if $\frac{\sqrt{3}}{36} < G \leq \frac{1}{16}$.
   - Circle: if $G > \frac{1}{16}$.

   Convex shapes have $H \geq 0.5$. Circle, square and all triangles have $H = 0.5$.

2. Non-convex (n-cornered star) shapes, where for at least one pair of points that fall inside the shape boundary, there are points on the straight line segment that connects them fall outside the shape boundary (Fig. 3.5). Non-convexity occurs in a significant fraction of pores in realistic rocks (Kovscek et al., 1993). The main characteristic of this type of shapes is the sharp corners, which facilitate the presence of wetting films and layers. Non-convex shapes have $H < 0.5$. This type of shape is represented by regular n-stars whom dimensionless hydraulic radius ($H_{n,\gamma}$) and shape factor ($G_{n,\gamma}$) are defined based on the number of corners n and the corner half-angle γ (Eq. 3.3).

$$H = \frac{R_h}{R_{ins}} = \frac{\frac{A}{L}}{R_{ins}}. \tag{3.2}$$

$$H_{n,\gamma} = \frac{1}{2}\sin(\gamma + \frac{\pi}{n}), G_{n,\gamma} = \frac{1}{4}\frac{\sin(\gamma)\sin(\gamma + \frac{\pi}{n})}{n\sin(\frac{\pi}{n})} \text{ with } \gamma < \frac{\pi}{2} - \frac{\pi}{n}. \tag{3.3}$$

The star shape for any cross-section with dimensionless hydraulic radius < 0.5 and arbitrary shape factor can be identified uniquely (Helland et al., 2008), Fig. 3.6.

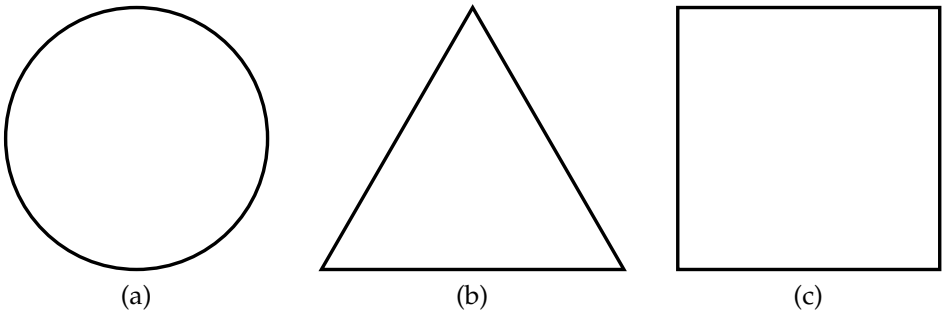

Figure 3.4: Convex pore cross-sections.

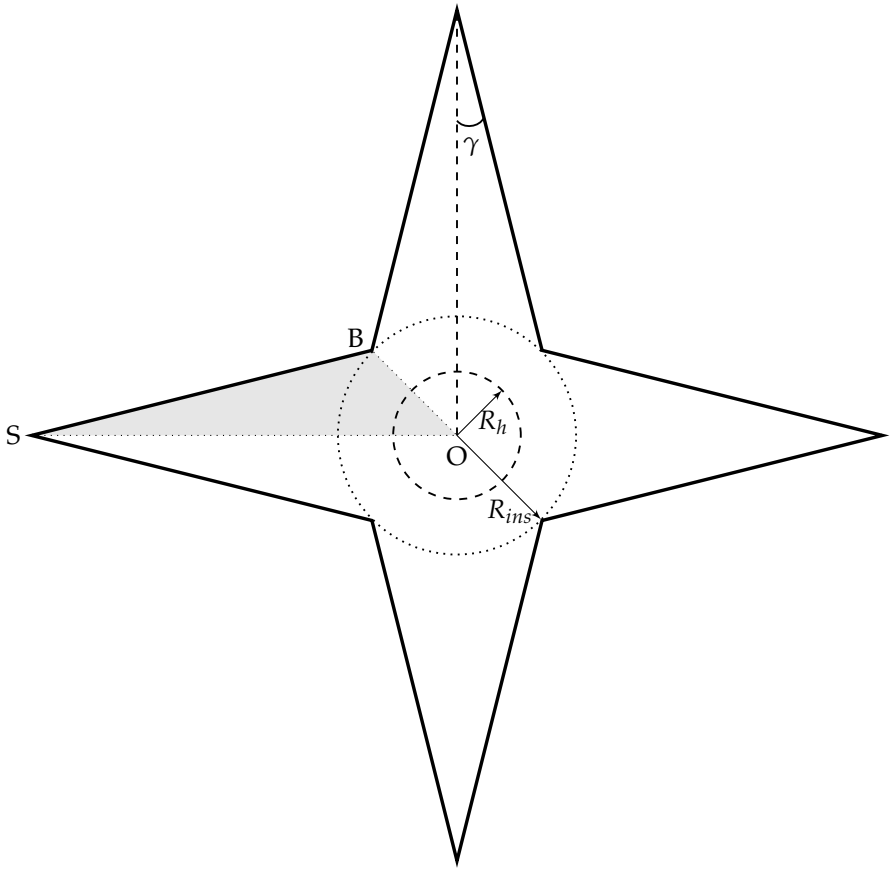

Figure 3.5: Non-convex regular n-star cross-section. R_h is the hydraulic radius, R_{ins} the inscribed radius and γ is corner half angle. The shaded elementary triangle SOB is used to calculate the shape factor of the limiting regular n-cornered polygon (section 3.4).

In this study, the pore networks that are used as input for the network flow model consists of pore bodies (nodes) and pore throats (bonds). We used n-cornered star, equilateral triangle, square and circle shapes for the pores cross-sections.

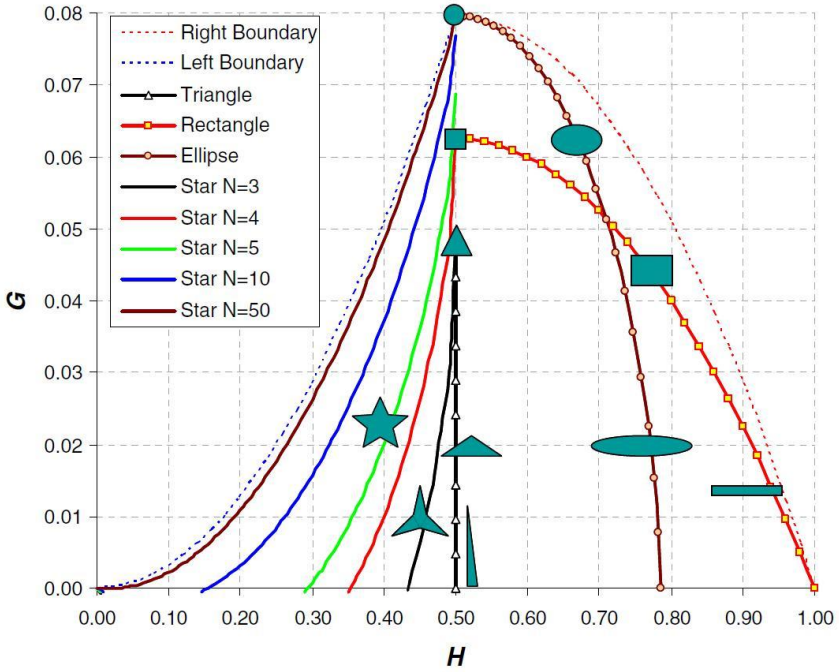

Figure 3.6: Shape factor (G) versus dimensionless hydraulic radius (H) for various shapes. The left boundary and the right boundary are the theoretical limits for the G and H values of any shape (Ryazanov et al., 2009).

3.4 CONDUCTANCE CALCULATIONS

The conductances of different phases that occupy different parts of the pore cross-section area (bulk, layers and corner films) are used to calculate the (relative) permeabilities. For the calculation of these properties, the flow is assumed to be steady state, laminar flow in each phase, with constant viscosity. The fluids are assumed to be incompressible.

3.4.1 *Single-phase conductance*

The single-phase conductance, when one fluid occupies the entire cross-section, can be approximated in the pores with C-T-S shapes as (Øren et al., 1998; Valvatne and Blunt, 2004; Piri and Blunt, 2005a):

$$g = \frac{C_g A^2 G}{\mu}, \tag{3.4}$$

where μ denotes viscosity, C_g is a constant which is equal to 0.6 for arbitrary triangles, 0.5623 for squares and 0.5 for circles.

For an n-cornered star, the single-phase conductances can be calculated numerically (Helland et al., 2006, 2008), see Fig. 3.7. Ryazanov et al. (2009) have derived a new correlation based on the numerical results:

$$g = \tilde{g} A^2, \tag{3.5}$$

where $\tilde{g}$ denotes the dimensionless single-phase conductance for n-cornered stars, given by

$$\tilde{g} = C(n) \left(\frac{G^t_{n,\gamma}}{G^{t,max}_n} \right)^{B(n)}, \tag{3.6}$$

where

$B(n)$ and $C(n)$	fifth order polynomials of n.
$G^t_{n,\gamma}$	the shape factor of the elementary triangle SOB (see Fig. 3.5).
$G^{t,max}_n$	the shape factor of the elementary triangle for the limiting regular n-cornered polygon.

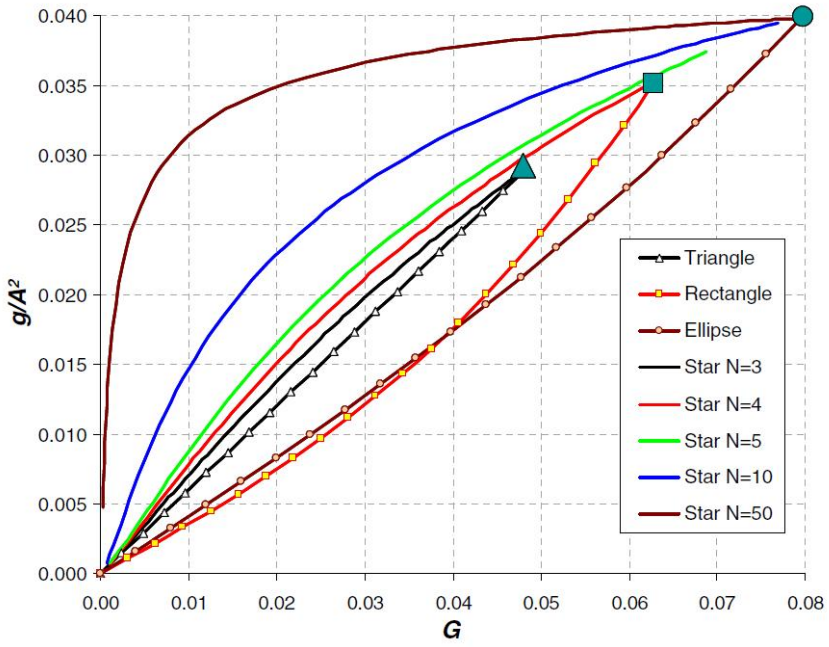

Figure 3.7: Single-phase conductance vs. shape factor (Ryazanov et al., 2009).

3.4.2 *Area and conductance of corner films and layers*

During two- and three-phase flow, more than one fluid can coexist in the same pore. A fluid can exist in a corner of an angular pore as one or two of the following simultaneously: corner film, layer or bulk. Fig. 3.8 shows the general situation in which film, layer and bulk exist at one corner α. The area and conductance are computed for each phase separately. The corner area that is bounded by Arc Meniscus (AM) at the interface of the fluids i and j with radius of curvature r_{ij} at a given corner (α) is calculated as:

$$A_{ij}^{(\alpha)}(r_{ij}, \theta_{ij}) = r_{ij}^2 \left(\theta_{ij} + \gamma^{(\alpha)} - \frac{\pi}{2} + \cos\theta_{ij} \frac{\cos(\theta_{ij} + \gamma^{(\alpha)})}{\sin\gamma^{(\alpha)}} \right), \tag{3.7}$$

where θ_{ij} is the contact angle between the two fluids (i and j).

The film area $A_f^{(\alpha)}$ at a given corner (α) is equal to the corner area that is bounded by AM1:

$$A_f^{(\alpha)} = A_{23}^{(\alpha)}(r_{23}, \theta_{23}). \tag{3.8}$$

The model employs a correlation proposed by Øren et al. (1998) to estimate the films conductance $g_{i,f}$ of phase i for a no-slip boundary condition at AM1:

$$g_{i,f} = nC \frac{\left(A_f^{(\alpha)}\right)^2 G_f}{\mu_i}, C = 0.364 + 0.28 \frac{G_f^*}{G_f}, \tag{3.9}$$

where n is the number of corners, A_f is the area of the film (Eq. 3.8), G_f is the shape factor for the corner cross-section which contains the film, G_f^* is the shape factor in case of zero curvature of the fluid–fluid interface, μ_i is the phase viscosity.

The layer area that is bounded by AM1 and AM2 at given corner (α) can be computed:

$$A_l^{(\alpha)} = A_{12}^{(\alpha)}(r_{12}, \theta_{12}) - A_{23}^{(\alpha)}(r_{23}, \theta_{23}). \tag{3.10}$$

For the layer conductance $g_{(j,l)}$ of fluid j, the model uses a correlation proposed by Valvatne and Blunt (2004):

$$g_{(j,l)} = n\frac{L_j^4 \widetilde{g}_l}{\mu_j}, \tag{3.11}$$

where L_j is the apex distance for the AM2 position, μ_j is the phase viscosity and $\widetilde{g}_l$ is the dimensionless conductance of the layer, given by:

$$ln\widetilde{g}_l = a_1 ln^2\left(\widetilde{A}_l^3 G_l\right) + a_2 ln\left(\widetilde{A}_l^3 G_l\right) + a_3, \tag{3.12}$$

where $\widetilde{A}_l$ is the dimensionless area of the layer, G_l is the shape factor of the layer and $a_i (i = 1...3)$ are the polynomial fitting parameters.

The bulk area can be calculated by:

$$A_b = A - \sum_{\alpha=1}^{n}\left(A_f^{(\alpha)} + A_l^{(\alpha)}\right), \tag{3.13}$$

where n is the number of corners and A is the cross-section area of the pore.

The bulk conductance ($g_{k,b}$) of phase k is estimated from the single-phase conductance as (Øren et al., 1998):

$$g_{k,b} = \frac{A_b}{A} g, \tag{3.14}$$

where A_b is the bulk area given by Eq. 3.13, A is the cross-section area and g is the single phase conductance given by Eq. 3.4 for C-T-S shapes and by Eq. 3.5 for n-cornered star shapes.

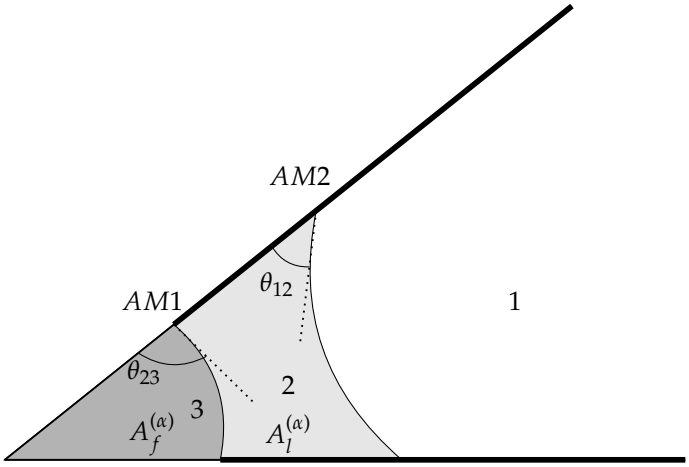

Figure 3.8: General fluid configuration in a pore corner with film, layer and bulk phases separated by arc menisci AM1 and AM2. Dark gray denotes flim phase (3), light gray denotes layer phase (2), white denotes bulk phase (1), $A_f^{(\alpha)}$ denotes film area, $A_l^{(\alpha)}$ denotes layer area, θ_{12} denotes the contact angle between layer and bulk phases, θ_{23} denotes the contact angle between film and layer phases, and bold lines denote the surfaces of altered wettability (section 4.3.2).

3.5 SATURATION CALCULATION

Each element (pore body or pore throat) is allowed to have volumes for each type of phase occupancy (film, layer and bulk),

$$V_e = \sum_{i=1}^{3} \left(v_b^i + v_f^i + v_l^i \right), \tag{3.15}$$

where i denotes the phase ($i = 1 \ldots 3$), V_e is element volume, v_b is bulk volume, v_f is film volume and v_l is layer volume.

The total volume of phase i in the network is given by

$$V_i = \sum_{j=1}^{n} \left(v_{b,j}^i + v_{f,j}^i + v_{l,j}^i \right), \tag{3.16}$$

where $v_{b,j}^i$, $v_{f,j}^i$ and $v_{l,j}^i$ are the bulk, film and layer volumes, respectively, of phase i in element j.

Each element j in the network has some amount of constant clay volume $V_{c,j}$ which is normally not removed during the core floods (Valvatne and Blunt, 2004).

This volume is given in the input data file of the network, Table 3.1. The total clay volume in the network is given by

$$V_{clay} = \sum_{j=1}^{n} \left(V_{c,j} \right), \tag{3.17}$$

where $V_{c,j}$ is the clay volume in the element j and n is the total number of elements in the network.

Therefore, the total volume of the network is given by

$$V_{total} = V_{clay} + \sum_{i=1}^{3} V_i. \tag{3.18}$$

Saturations of oil, gas and water can be calculated as

$$S_o = \frac{V_o}{V_{total}}, \tag{3.19}$$

$$S_g = \frac{V_g}{V_{total}}, \tag{3.20}$$

and

$$S_w = \frac{V_w + V_{clay}}{V_{total}}, \tag{3.21}$$

where volumes of oil V_o, gas V_g and water V_w are computed by Eq. 3.16.

3.6 POROSITY

Porosities are calculated based on the volumes of bonds, nodes, clay and the cubic volume (V_{cv}) occupied by the network:

$$\phi_{net} = \frac{\sum_{i=1}^{n} V_i}{V_{cv}}, \tag{3.22}$$

$$\phi_{clay} = \frac{V_{clay}}{V_{cv}}, \tag{3.23}$$

and

$$\phi_{total} = \phi_{net} + \phi_{clay}, \tag{3.24}$$

where ϕ_{net} denotes net porosity, n denotes the number of elements (bonds+nodes), V_{clay} denotes total clay volume in the network (Eq. 3.17), V_i denotes pore volume, ϕ_{clay} denotes clay porosity and ϕ_{total} denotes total porosity.

3.7 ABSOLUTE PERMEABILITY AND RELATIVE PERMEABILITY CALCULATION

Permeability is a property of porous media. It determines the ability of fluids to flow through the porous media. When a single phase is present in the porous media, it is called absolute permeability. If there are other immiscible phases present, it is called the effective permeability. The ratio of the effective permeability of a particular phase to the absolute permeability of that phase is used to compare different abilities of phases to flow in the presence of each other. This dimensionless ratio is called the relative permeability.

The absolute permeability is calculated by assuming that the network is filled by a single incompressible phase. A pressure drop ΔP is imposed across the network length L, from the inlet of the network to its outlet, to compute the pressure distribution from the set of equations, based on the mass conservation at each node (Øren et al., 1998):

$$\sum_{j=1}^{n} q_{ij} = 0, \text{ for each node } i, \tag{3.25}$$

where n denotes the number of nodes connected to node i, q_{ij} denotes the flow rate between nodes i and j given as

$$q_{ij} = \frac{g_{ij}}{L_{ij}} \Delta P_{ij}, \tag{3.26}$$

where g_{ij} denotes the effective hydraulic conductance between node i and node j given by Eq. 3.27 as the harmonic mean of the conductances of the bond and

the adjoining nodes (Øren et al., 1998), L_{ij} distance between the centres of the nodes i and j and ΔP_{ij} pressure difference between the nodes.

$$\frac{L_{ij}}{g_{ij}} = \frac{1}{2}\frac{L_i^n}{g_i^n} + \frac{L_{ij}^b}{g_{ij}^b} + \frac{1}{2}\frac{L_j^n}{g_j^n}, \tag{3.27}$$

where g_i^n, g_j^n and g_{ij}^b denote conductances of nodes (i and j) and bonds respectively (see section 3.4), L_i^n, L_j^n and L_{ij}^b denote lengths of nodes (i and j) and bond respectively.

The total flow rate Q_x in the direction of the flow x in response to ΔP is used in Darcy's law to calculate the absolute permeability k:

$$Q_x = -\frac{k}{\mu}\frac{\Delta P}{L}A, \tag{3.28}$$

where μ denotes viscosity and A denotes the total cross-sectional area of the model perpendicular to the flow direction.

Similar to absolute permeability calculations, a pressure drop ΔP is imposed across the network to compute the pressure distribution of each hydraulically connected phase i. For each phase, the flow rate in the flow direction is calculated by applying a pressure drop across the network and using the bulk, film and layer pore conductances (section 3.4) for the considered phase only. Finally, the flow rate $Q_{x,i}$ is used in the Darcy type expression to calculate the relative permeability $k_{r,i}$ as

$$Q_{x,i} = -\frac{kk_{r,i}}{\mu_i}\frac{\Delta P}{L}A, \tag{3.29}$$

where k denotes absolute permeability given by Eq. 3.28, μ_i denotes the viscosity of phase i, L denotes the length of the network and A denotes the cross-section of the network.

3.8 SUMMARY AND CLOSING REMARKS

In this chapter, we discussed the shape of the real pores. Previous authors showed that the real pore shapes are irregular with many corners that can accommodate water whereas oil occupies the centre of the pore. Additionally, oil layers surrounded by corner water films and bulk water or gas phases could form. These films and layers help to keep the hydraulic connectivity for their corresponding phases, maintaining pathways for the the phase to escape the system. The networks, which are used as input for our model, consist of pore bodies (nodes) and pore throats (bonds). The dimensionless hydraulic radius of the pore cross-section defines the convexity, which can be used to characterise the cross-sections as (1) Convex Circle, Triangle and Square (C-T-S) shapes and (2) non-convex n-cornered star shapes. These two regular shapes are assigned to the cross-sections of the pores based on the shape factor. They allow for easy analytical calculation of the intra-pore flow properties. Finally, equations for the conductance, porosity, phase saturations, absolute permeability and relative permeability were presented in this chapter. The displacement processes at the pore-scale and the corresponding three-phase capillary entry pressures, demonstrating the key features of the new pore-network model, will be described in the next chapter.

4

THREE-PHASE FLOW PORE-NETWORK MODEL DESCRIPTION

4.1 INTRODUCTION

In the previous two chapters, we have introduced two aspects of the model: the implementation of wettability conditions (chapter 2) and the incorporation of complex network structures (chapter 3). In this chapter, we focus mainly on the displacement processes during different floods at the pore-level. We describe the two most important advancements in the current model. These comprise the implementation of a thermodynamic criterion for oil layer formation and collapse, and multiple displacement chains.

In the displacement processes considered in this study, initially all the pores and throats (network elements) are filled with only water. Then, oil is injected into the network until connate water saturation, S_{wc}. After that, wettability alteration takes place in the oil-filled pores. Note that only the wettability of the oil contacted part of the element surface changes (Kovscek et al., 1993). Then water invades the network until residual oil saturation S_{or} is achieved or until a predefined initial water saturation S_{wi} is reached, at which gas invasion into the system at $S_w = S_{wi}$ takes place. Additionally, WAG injection may be simulated.

Every element with angular cross-section can accommodate up to three different phases (Piri and Blunt, 2005a; van Dijke et al., 2004a, 2007). We considered that the three phases can be present as films in the pore corners, as a bulk phase in centre of the pore, or as layers sandwiched between the bulk phase and the films (van Dijke et al., 2004a, 2007), presented in section 3.4.2. We have not considered the configurations that involve double layers as Piri and Blunt (2005a)

did. Therefore, at any given corner, we allowed a maximum of two arc menisci (AMs) to be present (Fig. 3.8). The formation of the films and layers will be discussed later in section 4.3.

A cluster of phase i is defined as an interconnected set of network elements that accommodate at least one fluid element (bulk, film or layer) of phase i. For instance, a water cluster could have a network element which contains water as corner films, bulk or both. Therefore, every network element can belong to a maximum of three different clusters of different phases at the same time. For example, a network element containing films and bulk of water and layers of oil will belong to both oil and water clusters, implying that films and bulk are from the same water cluster and thus they have the same pressure (Piri and Blunt, 2005a; Ryazanov et al., 2009, 2010).

In this chapter, we present all possible pore fluid configurations (section 4.2) and pore level displacements (section 4.3), which may occur during different floods (primary drainage, imbibition, secondary or tertiary gas injection and WAG injection). In particular, we focus on two levels of displacements: (1) The displacement of one phase by another one in a single pore, emphasising the new implementation of the formation and collapse of oil layers during different floods. We have used the thermodynamic based capillary entry pressure criteria of van Dijke et al. (2004a). They extended the MS-P method (Mayer and Stowe, 1965; Princen, 1969a,b, 1970) to three-phase flow by formulating the balance of virtual work and change of surface free energy for a small displacement. This was done for a three-phase configuration at capillary equilibrium in a pore with angular cross-section. Additionally, they derived a thermodynamic condition for the existence of layers of an intermediate-wetting phase (van Dijke et al., 2004a, 2007). We describe the three-phase capillary entry pressures based on the thermodynamic criterion in section 4.4. (2) The displacement chain that involves a series of clusters which displace each others. This displacement chain is known as the multiple displacements which are an extension of double displacements (Øren and Pinczewski, 1995; Fenwick and Blunt, 1998b; Piri and Blunt, 2005a). The multiple displacements occur when injection of a phase at the inlet leads to movement of a series of phase clusters spanning from the inlet to the outlet. This important three-phase flow phenomenon was revealed by micromodel experiments (Sohrabi et al., 2000, 2001, 2004) in which disconnected clusters of oil,

water or gas, which were formed during different floods (e.g. trapped oil clusters during (imbibition) water flood), were observed to move during three-phase flow (e.g. tertiary gas injection) and reach the outlet of the micromodel. They are the cause of lower residual oil saturations because less oil remains trapped in isolated clusters. van Dijke et al. (2004b) were the first to implement the multiple displacements in a 3D lattice pore-network model, described in section 1.4. We implemented the multiple displacements in the new pore-network model (section 4.5). This allows for accurate modelling of the mobilization of disconnected phase clusters that arise during higher order (WAG) floods.

All floods are assumed to be capillary dominated and are simulated according to invasion percolation principles (Valvatne and Blunt, 2004; Piri and Blunt, 2005a). The displacement events are modelled in invasion-percolation by increasing the pressure of the invading phase at the inlet while keeping the pressure of the outlet connected phases (or reference phase) constant. The pressure boundary conditions are imposed at the inlet and the outlet of the network (Ryazanov et al., 2009). For two-phase flow, during oil and water injections, the overall network capillary pressure $P_{c,ow} = P_o - P_w$ is gradually increased and decreased, respectively (Patzek, 2001; Valvatne and Blunt, 2004). During various three-phase floods, the pressure of the injecting phase (P_{inj}) at the inlet is gradually increased while the pressure of a reference phase (P_{ref}) at the outlet is kept constant. This results in increasing the overall pressure difference $P_{diff} = P_{inj} - P_{ref}$, leading to many possible multiple displacement chains. To find the most favourable displacement chain in the network during the three-phase invasion-percolation process, we implemented a computationally efficient shortest path search algorithm (van Dijke et al., 2008), described in section 4.5.

In the following sections, we present the fluid configurations in an angular pore that are possible during multiphase flow under the wettability assumptions described in chapter 2. Then, the displacement processes at the pore-level are described with the possible changes in the fluid configurations during different floods. After that, we introduce the new thermodynamic criterion to the model to calculate the three-phase capillary entry pressures. Then, we give a full description of the shortest path algorithm, which is used for determination of the preferred multiple displacements, and we describe its advantages. Finally,

we state some of the computational issues that have been encountered during the model development.

4.2 PORE PHASE OCCUPANCIES

To illustrate the fluid configuration and displacements at pore level, we use an equilateral triangular cross-section as an example of pores with angular cross-section (Fig. 4.1). We present all the fluid configurations in the cross-section of an angular pore with equal corners that may arise during three-phase flow (Fig. 4.2). Fluid configurations are included for surfaces with uniform wettability and surfaces with non-uniform wettability. Every pore surface could have two portions of different wettability (water-wet surface and altered wettability surface, e.g. configuration P) (Kovscek et al., 1993). The direction of the curvature of any Arc Meniscus (AM) depends on the underlying surface wettability and the phases that are present at either side of that AM. Generally, AMs curve in unless at the point where wettability changes. Therefore, we define fluid configuration based on the pore surface wettability (uniform unaltered wettability, uniform altered wettability, or non-uniform wettability), phases that are present in the pore (oil, water and gas) and their form (film, layer and bulk).

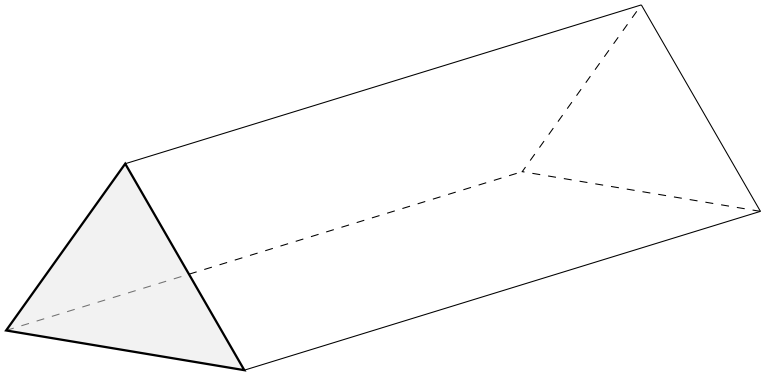

Figure 4.1: A pore with equilateral triangular cross-section.

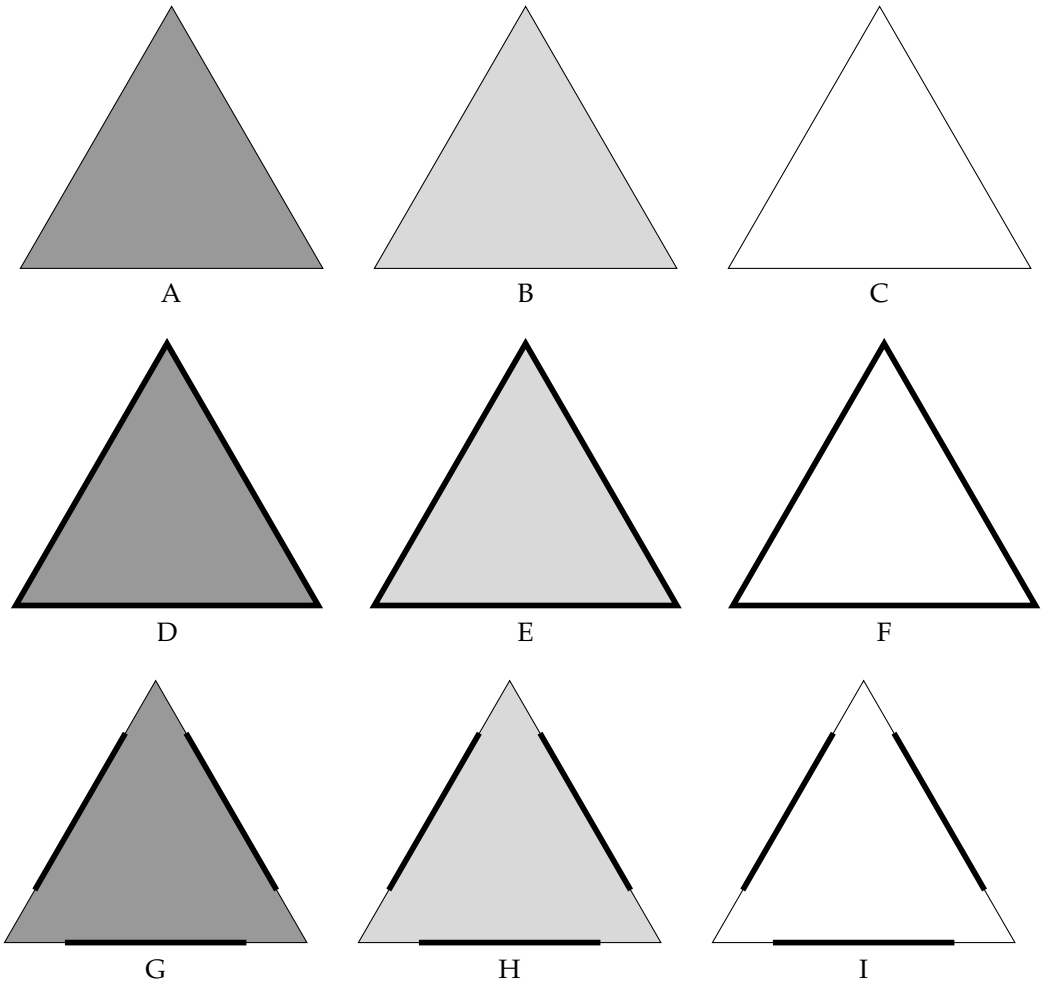

Figure 4.2: *Continued on next page . . .*

. . . continued from previous page

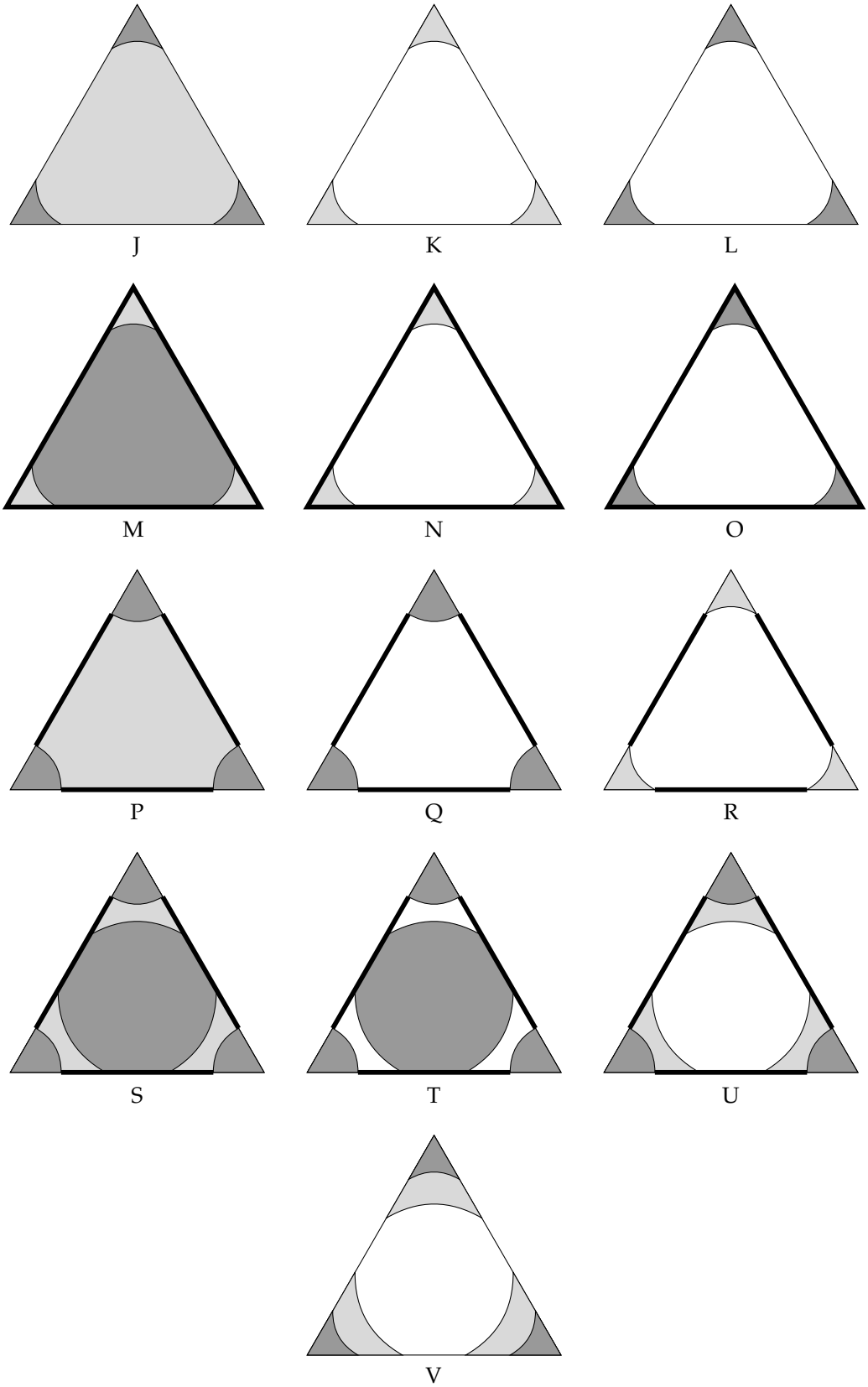

Figure 4.2: Occupancies in an idealised pore of equilateral triangular cross-section for fluid configurations during gas invasion. Dark gray denotes water, light gray denotes oil, white denotes gas and bold lines denote the surfaces of altered wettability. Note that the direction of the curvature for the AMs that bounds the films in configurations of non-uniform wettability (e.g. Q, S, T and U) could be different, depending on the AM contact angle.

4.3 DISPLACEMENT PROCESSES

We define the pore-scale displacement as an event where the fluid configuration of the pore cross-section changes to an essentially different fluid configuration. For instance, when a phase i (e.g. gas) invades a pore, filled with a different phase j (e.g. oil), a possible pore displacement could occur as shown in Figs. 4.3–4.4. There is an entry capillary pressure P_{entry} that must be overcome for each pore displacement to take place. This P_{entry} is defined in terms of an (effective) entry radius r_{entry}:

$$P_{entry} = P_i - P_j = \frac{\sigma_{ij}}{r_{entry}}, \tag{4.1}$$

where i denotes the invading phase, j denotes the defending phase, σ_{ij} denotes the interfacial tension between the two phases, and P_i and P_j are pressures of the phases. The value of r_{entry} depends on the pore shape and the pore displacement. It is defined in terms of two principal radii of curvatures (r_1,r_2) by the Laplace equation:

$$\frac{1}{r_{entry}} = \frac{1}{r_1} + \frac{1}{r_2}. \tag{4.2}$$

There are two types of fluid-fluid interface in the pore (Figs. 4.3–4.4), Main Terminal Meniscus (MTM) and Arc Meniscus (AM).

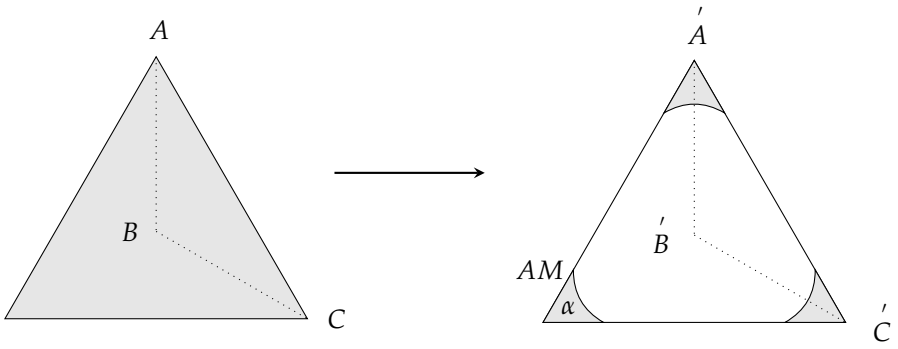

Figure 4.3: Phase j (gray) is displaced by phase i (white) in a pore with equilateral triangular cross-section. Corner α is illustrated in Fig. 4.5.

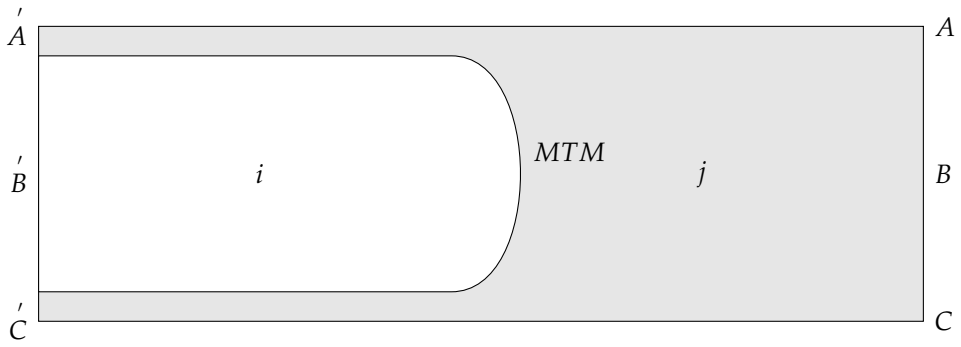

Figure 4.4: Cross-section along a pore showing a small displacement of phase j by i as indicated in Fig. 4.3, showing the MTM.

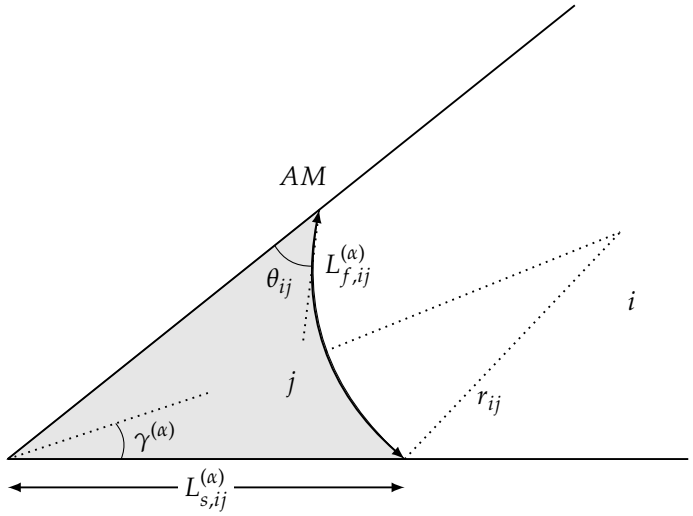

Figure 4.5: Phase occupancy in a corner with corner wetting film phase j and bulk phase i. We call j the inner phase of the AM and i the outer phase of the AM.

For a pore with circular cross-section, only MTM can exist (Fig. 4.6). The entry radius for piston-like displacement is given by

$$r_{entry} = \frac{r_{ins}}{2\cos\theta_{ij}}, \tag{4.3}$$

where r_{ins} is the radius of the circular cross-section. Hence, the entry pressure is

$$P_{entry} = \frac{2\sigma_{ij}\cos\theta_{ij}}{r_{ins}}. \tag{4.4}$$

The AM is limited to the pores with angular cross-section (Fig. 4.5). The AM for a given fluid-fluid combination is present if it satisfies a simple geometrical

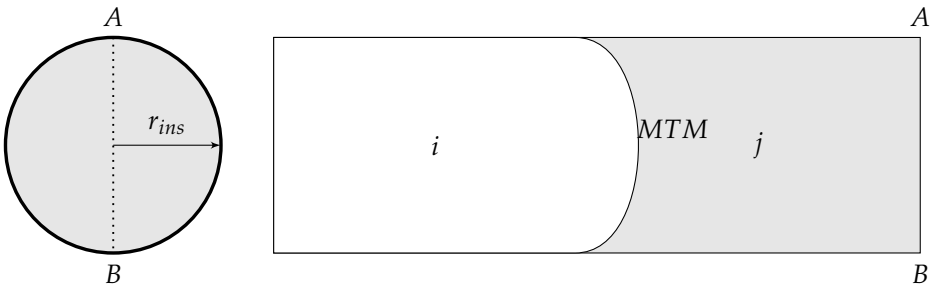

(a) (b)

Figure 4.6: (a) Pore with circular cross-section with radius r_{ins}. (b) Piston-like displacement along a pore with circular cross-section, showing that the MTM is present at the interface between the invading phase i and the defending phase j.

criterion relating the contact angle θ_{ij}, measured through the more wetting phase j, of the AM to the corner half angle $\gamma^{(\alpha)}$ in corner α (Fig. 4.5), given by:

$$\theta_{ij} < \frac{\pi}{2} - \gamma^{(\alpha)}. \tag{4.5}$$

At capillary equilibrium, we define each AM, which separates two phases in the corners, with the radius of curvature r_{ij} that is consistent with the Laplace equation

$$P_{ij} = \frac{\sigma_{ij}}{r_{ij}}, \tag{4.6}$$

where $P_{ij} = P_i - P_j$ denotes the pressure difference between the phases.

The apex distance $L_{s,ij}^{(\alpha)}$ of the AM (Fig. 4.5) is given by

$$L_{s,ij}^{(\alpha)} = r_{ij} \frac{cos(\theta_{ij} + \gamma^{(\alpha)})}{sin\gamma^{(\alpha)}}. \tag{4.7}$$

In the next section, we describe the displacement processes during different floods. These floods correspond to what happens to the reservoir, starting with primary oil migration and ending with the injection of water and gas during the production phase.

4.3.1 *Primary drainage (oil flooding)*

At the start of any simulation, the network is assumed to be occupied by water and to be strongly water-wet. If we take a pore throat (a straight tube) with an equilateral triangle-cross section in the network (Fig. 4.1), then this pore will have fluid configuration A (Fig. 4.2) and is uniformly wetted, i.e. it is water-wet with drainage contact angle $\theta_{ow}^{dr} < \frac{\pi}{2}$. Then the network is invaded by oil during primary drainage. During this flood, oil may displace water from the pore by piston-like displacement, leading to a change in the fluid configuration of the pore cross-section. Water could either be removed completely from the pore (configuration B) or it could remain in the corner as films (configuration J), creating arc menisci at the oil-water interfaces.

For primary drainage, the formation of these arc menisci is determined by the geometrical condition, for θ_{ow}^{dr} (Eq. 4.5). Hence, there are three possible fluid configurations of the pores during primary drainage process A, B and J (Fig. 4.2), and the two possible displacements that can occur during this flood are indicated in Fig. 4.7. The entry radius r_{entry}^{NFF} for the no-film formation (NFF) displacement, A→B, is given by Eq. 4.8 whereas the entry radius r_{entry}^{FF} for the film formation (FF) displacement, A→J, is given by Eq. 4.9 (Ryazanov et al., 2009).

$$r_{entry}^{NFF} = \frac{r_{ins}}{2} \frac{\sin(\frac{\pi}{n})}{\cos(\theta_{ow}^{dr} + \gamma^{(\alpha)})}. \tag{4.8}$$

$$r_{entry}^{FF} = \frac{1}{2} \frac{\cos\theta_{ow}^{dr} L_{n,\gamma} - \sqrt{\cos^2\theta_{ow}^{dr} L_{n,\gamma}^2 - 4nA_\alpha A_{n,\gamma}}}{nA_\alpha}, \tag{4.9}$$

where $L_{n,\gamma}$ and $A_{n,\gamma}$ are the perimeter and area respectively of the n-cornered star shape with half-angle γ. A_α is the dimensionless film area in a single corner α, given by Eq. 4.10 for $\theta_{ow} = \theta_{ow}^{dr}$ (Helland et al., 2006, 2008).

$$A_\alpha = \theta_{ow} + \gamma^{(\alpha)} - \frac{\pi}{2} + \cos\theta_{ow} \frac{\cos(\theta_{ow} + \gamma^{(\alpha)})}{\sin\gamma^{(\alpha)}}. \tag{4.10}$$

r_{entry}^{FF} is smaller than the maximum radius r_{entry}^{sn} associated with snap-off (van Dijke et al., 2007):

$$r_{entry}^{FF} < r_{entry}^{sn} = \frac{L_s}{2n} \frac{\sin \gamma^{(\alpha)}}{\cos(\theta_{ow}^{dr} + \gamma^{(\alpha)})}. \tag{4.11}$$

At the end of the primary drainage process, the maximum oil-water pressure difference is P_{ow}^{dr}. If $P_{ow}^{dr} > P_{entry}$ (Eq. 4.1), oil will have invaded the pore. If AMs exist, their radii of curvature r_{ow} are given by Eq. 4.6.

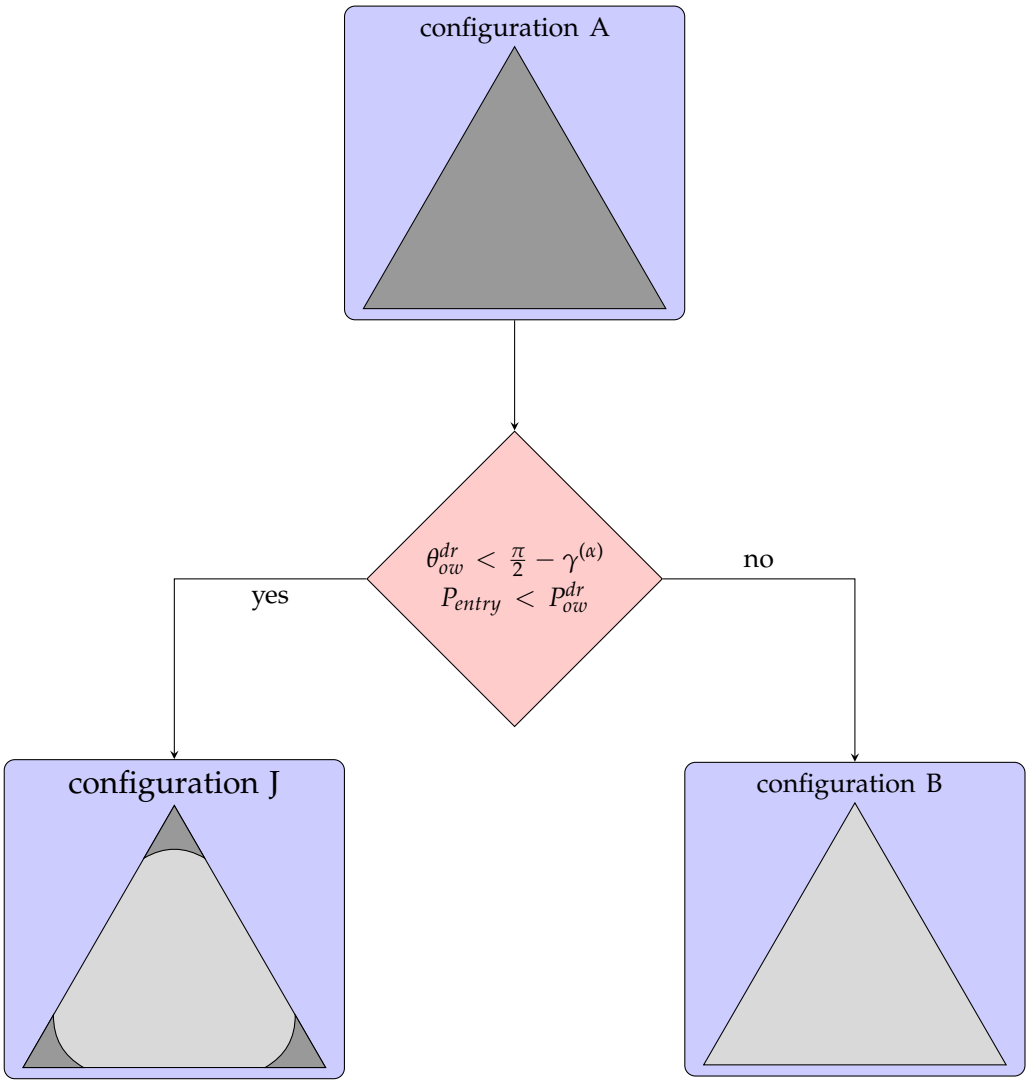

Figure 4.7: Flowchart of the two possible displacements scenarios during primary oil drainage for an angular pore.

4.3.2 *Wettability alteration (ageing)*

After the primary drainage, the wettability of the oil-filled pore surfaces, which are in contact with oil, may have been altered by changing the contact angles. This represents the alteration of the reservoir wettability during ageing. The wettability of the pore surface which stays in contact with water remains unaltered, having the same contact angle as during primary drainage $\theta_{ow}^{w} = \theta_{ow}^{dr}$ whereas the pore surface which is in contact with oil changes its wettability (Fig. 4.8). This pore with two different wettability surfaces is known as a pore with non-uniform wettability (Kovscek et al., 1993). The degree of ageing is modelled by the oil-water contact angle (θ_{ow}^{alt}) of the altered wettability surface.

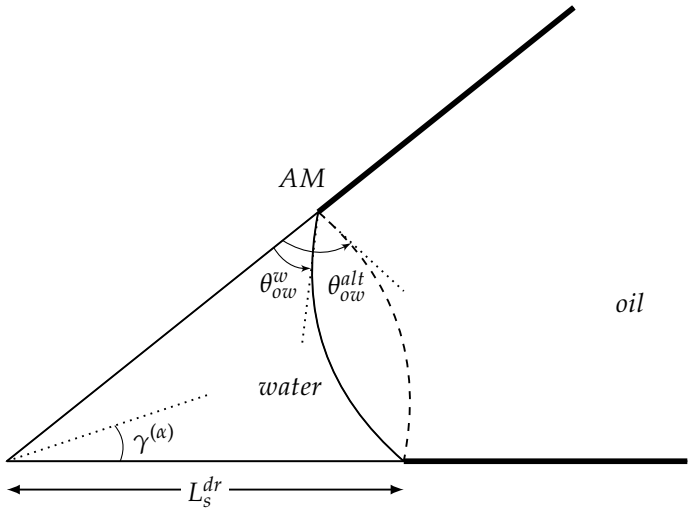

Figure 4.8: Phase occupancy in corner with film phase j and bulk phase i. Bold lines denote the surfaces of altered wettability.

The half length of the unaltered wettability corner surface L_s^{dr} (Fig. 4.8) is given by Eq. 4.7 for $\theta_{ij} = \theta_{ow}^{dr}$ and $r_{ij} = r_{ow}^{dr}$, which is the minimum oil-water radius of curvature. It corresponds to P_{ow}^{dr} that is reached at the end of the primary drainage process. The oil-water AM in the corner is pinned at L_s^{dr} during subsequent water flood with hinging contact angle $\theta_{ow,h}$, for $\theta_{ow}^{w} < \theta_{ow,h} < \theta_{ow}^{alt}$.

4.3.3 *Imbibition (waterflooding)*

During the field life, water is often injected into the reservoir to maintain its pressure and to displace additional oil. At the pore level, water invades the network, displacing oil from the oil-filled pores either by piston-like displacement or by

snap-off. Piston-like displacement (bulk-bulk displacement) takes place when bulk water displaces bulk oil from the center of a pore. In this type of displacement, water must be available as a bulk phase in one of the neighbouring pore bodies. Snap-off occurs when bulk oil is displaced by the surrounding water films (section 4.4.2). In both types of displacement, water must be hydraulically connected to the inlet (i.e. the invading cluster), whereas oil must be connected to the outlet (i.e. oil is not trapped). During piston-like displacement, oil layers sandwiched between bulk water and water films (configuration S in Fig. 4.2) may form. The formation of oil layers is subject to whether or not the new AM satisfy the geometrical condition Eq. 4.5.

Additionally, the radii of curvature of the AMs should satisfy both geometric and thermodynamic conditions; we elaborate on this in section 4.4.1. The piston-like displacement during which the layers are formed is called Layer Formation (*LF*): P→S. This displacement may be followed by another displacement in which water displaces the oil layers, known as Layer Collapse (*LC*): S→G. However, oil could be removed completely at once from the pore by piston-like displacement (i.e. No Layer Formation (*NLF*)): P→G. Fig. 4.10 summaries these displacements. The capillary entry pressures during water invasion in pores with non-uniform wettability for the three displacements have been derived by van Dijke and Sorbie (2006), based on free energy variation. The capillary entry pressures were computed from the corresponding entry radii (Eq. 4.1):

1. Oil layer formation (P→S):

$$r_{entry}^{LF} = \frac{1}{2}\frac{\cos\theta_{ow}^{alt} L_{n,\gamma} + \sqrt{\cos^2\theta_{ow}^{alt} L_{n,\gamma}^2 - 4nA_\alpha A_{n,\gamma}}}{nA_\alpha}, \tag{4.12}$$

   where A_α is the dimensionless film area in the corner α bounded by the new arc meniscus (AM2 in Fig. 4.9), given by Eq. 4.10 for $\theta_{ow} = \theta_{ow}^{alt}$.

2. Oil layer collapse (S→G):

$$r_{entry}^{LC} = L^{dr}\frac{\sin\gamma^{(\alpha)}}{\cos(\theta_h + \gamma^{(\alpha)})}, \tag{4.13}$$

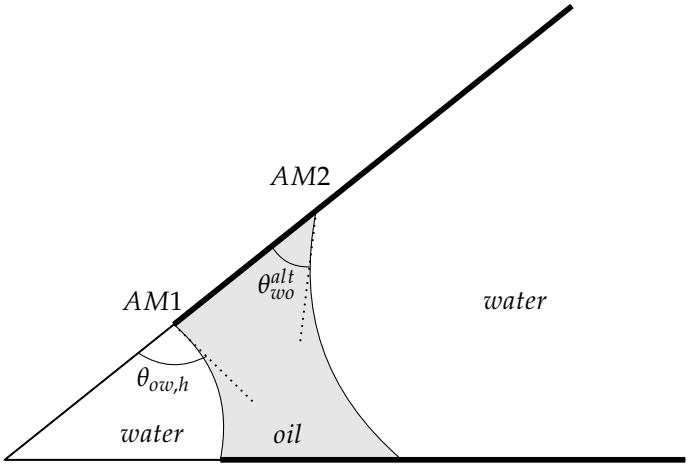

Figure 4.9: General fluid configuration in a pore corner with water film, oil layer and bulk water separated by arc meniscii $AM1$ and $AM2$. Bold lines denote the surfaces of altered wettability (section 4.3.2).

where θ_h is estimated by solving Eq. 4.14 numerically.

$$\pi - \theta_{ow}^{alt} - \theta_h + \cos\theta_{ow}^{alt}\frac{\cos(\theta_{ow}^{alt} - \gamma)}{sin\gamma} + (\cos\theta_h - 2\cos\theta_{ow}^{alt})\frac{\cos(\theta_{ow}^{alt} - \gamma)}{sin\gamma} = 0. \tag{4.14}$$

3. No layer formation (P→G): A system of two equations (Eqs. 4.15–4.16), derived from the MS-P theory, are solved iteratively to compute the entry radius r_{entry}^{NLF} and the hinging contact angle θ_h .

$$\begin{aligned} &-A_{n,\gamma} + r_{entry}^{NLF} L_{n,\gamma}\cos\theta_{ow}^{alt} + n{r_{entry}^{NLF}}^2 \left\{\frac{\pi}{2} - \theta_h - \right. \\ &\left. \gamma + (\cos\theta_h - 2\cos\theta_{ow}^{alt})\frac{\cos\theta_h\cos(\theta_h - \gamma)}{sin\gamma}\right\} = 0. \end{aligned} \tag{4.15}$$

$$r_{entry}^{NLF} = L^{dr}\frac{\sin\gamma^{(\alpha)}}{\cos(\theta_h + \gamma^{(\alpha)})}. \tag{4.16}$$

During this flood, eight possible changes of fluid configuration could occur to the oil-filled pore: P→S, S→G, P→G, E→M, B→A, E→D, H→G and J→A. Therefore, during a water flood the pore could have one of the ten possible fluid configurations: A, B, D, E, G, H, J, M, P and S.

At the end of the water flood, the minimum oil-water pressure difference is P_{ow}^{min}. If $P_{ow}^{min} < P_{entry}$ (Eq. 4.1), water will have invaded the pore. If AMs exist, their radii of curvature r_{ow} are given by Eq. 4.6.

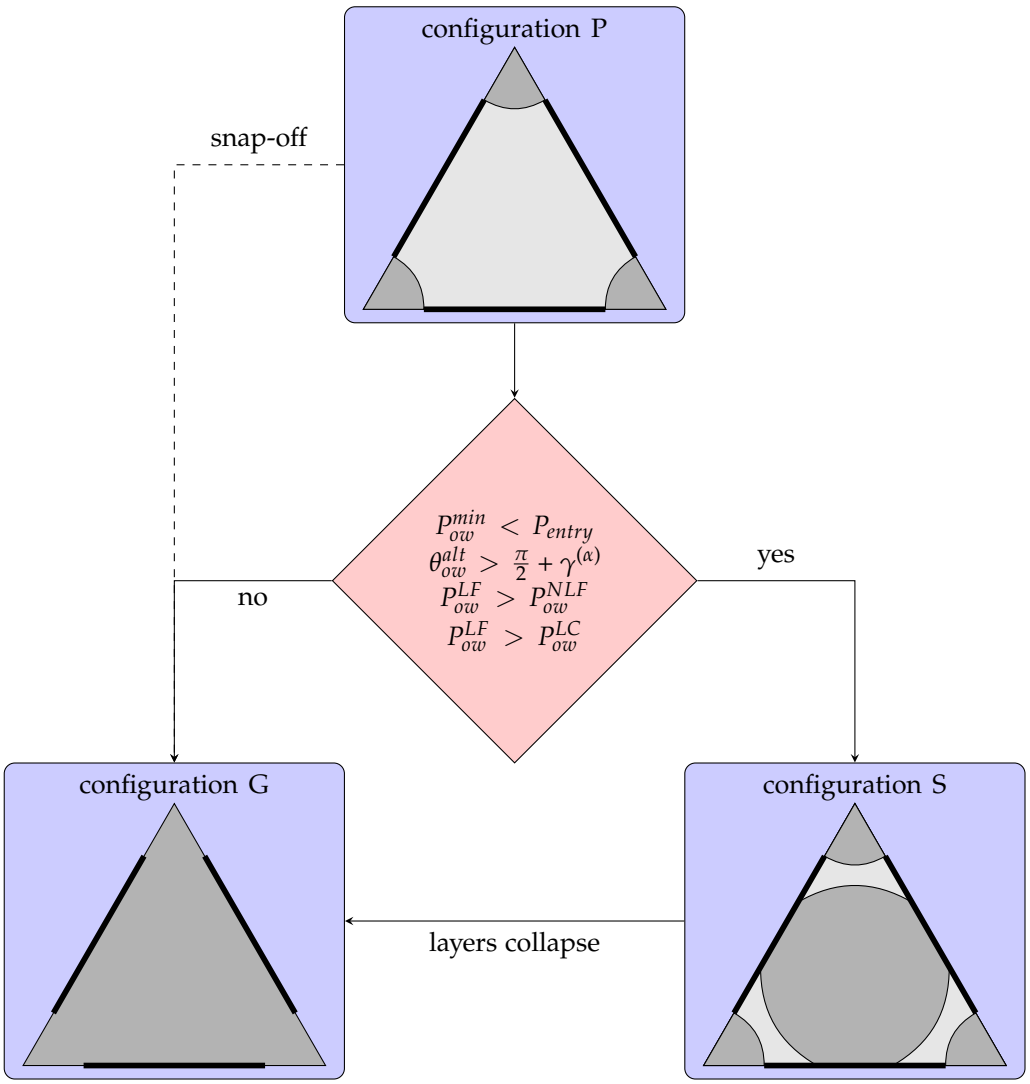

Figure 4.10: Flowchart of the selection of favourable displacement when water invades oil surrounded by water films in pore with equilateral triangular cross-section. Where layers were created, layers collapse may follow. Note that the geometrical condition Eq. 4.5 should be satisfied for all new AMs.

4.3.4 *Gas flood and WAG injection*

During gas and water floods (e.g. WAG injection), a pore can be invaded by any fluid because of multiple displacements (section 4.5) and thus for each displacement there is an invading phase (i), a defending phase (j) (where $i \neq j$), an old configuration, and possible new configurations. Table 4.1 summarizes all displacements, which have been implemented in the current model during gas and water floods. The formation of any new AM, which is associated with some displacements, has to meet the geometrical condition which relates the contact angle to the corner half angle in a given corner (Eq. 4.5). One of the important

displacements that occurs during gas injection is when gas displaces oil that is surrounded by water films (e.g. pore with fluid configuration P). Then, two displacements may take place: (1) Oil is completely displaced by gas (P→Q) with an entry pressure of P_{go}^{NLF} or (2) Oil remains as layers separating the water corner films and bulk gas (P→U) with an entry pressure of P_{go}^{LF}. These layers must satisfy the geometric condition, derived by Fenwick and Blunt (1995) and Firincioglu et al. (1999):

$$\frac{r_{23}}{r_{12}} \leq \begin{cases} \frac{\cos(\theta_{12}+\gamma^{(\alpha)})}{\cos(\theta_{23}+\gamma^{(\alpha)})} & \text{if } \theta_{23} \leq \theta_{12} \\ \frac{\cos\theta_{12}-\sin\gamma^{(\alpha)}}{\cos\theta_{23}-\sin\gamma^{(\alpha)}} & \text{if } \theta_{23} > \theta_{12} \end{cases}, \tag{4.17}$$

where 1 denotes bulk phase, 2 denotes layer phase and 3 denotes film phase.

Additionally, θ_{12} and θ_{23} must satisfy the condition (of Eq. 4.5). When layers have formed, a subsequent layer collapse displacement may take place (U→Q) with entry pressure P_{go}^{LC}. The favourable displacement is selected based on the flow chart in Fig. 4.11. The expressions for these entry pressures will be presented in section 4.4.

The formation of layers maintain the hydraulic connectivity of the oil and provide pathways for the oil to escape to the outlet. However, these layers could collapse at later stages of the flood, reducing the oil connectivity and causing oil to be disconnected and may be trapped. This depends on the capillary pressures of the formation and collapse of these layers. Therefore, finding the precise capillary entry pressures is essential. In next section we show the capillary entry pressures calculations and, specifically, the precise criteria for the formation and collapse of oil layers.

Table 4.1: Possible displacements during WAG injection at pore level.

OLD CONFIG.	i	j	NEW CONFIG.	NOTES
A	o	w	B	NFF
	g	w	C	NFF
	o	w	J	FF
	g	w	L	FF

Continued on next page ...

Table 4.1 – *Continued from previous page*

Old config.	i	j	New config.	Notes
B	w	o	A	NFF
	g	o	C	NFF
	g	o	K	FF
C	w	g	A	NFF
	o	g	B	NFF
D	o	w	E	NFF
	g	w	F	NFF
	g	w	O	FF
E	w	o	D	NFF
	w	o	M	FF
	g	o	F	NFF
	g	o	N	FF
F	w	g	D	NFF
	o	g	E	NFF
G	o	w	H	NFF
	o	w	P	FF
	g	w	I	NFF
	g	w	Q	FF
H	w	o	G	NFF
	g	o	I	NFF
	g	o	R	FF
I	o	g	H	NFF
	w	g	G	NFF
J	w	o	A	PL or SN
	g	o	L	NLF, FU
	g	o	V	LF
K	o	g	B	PL or SN
	w	g	A	PL: film/bulk removed

Continued on next page . . .

Table 4.1 – *Continued from previous page*

OLD CONFIG.	i	j	NEW CONFIG.	NOTES
L	o	g	J	PL, FU
	w	g	A	PL or SN
M	o	w	E	PL or SN
	g	w	N	PL, FU
	g	w	F	PL: film/bulk removed
N	o	g	E	PL or SN
	w	g	M	PL, FU
	w	g	D	PL: film/bulk removed
O	w	g	D	PL or SN
	o	g	E	PL: film/bulk removed
P	w	o	G	PL or SN
	g	o	Q	NLF, FU
	g	o	U	LF
Q	o	g	P	NLF
	w	g	G	PL or SN
R	o	g	H	PL or SN
	w	g	G	film/bulk removed (very rare displacement)
S	o	w	P	PL or SN
	g	w	U	PL, LU
	w	o	G	LC
T	g	w	Q	PL or SN
	w	g	G	LC
U	o	g	P	PL or SN
	w	g	S	LU
	g	o	Q	LC
V	o	g	J	PL or SN
	w	g	A	layer/bulk removed

Continued on next page ...

Table 4.1 – *Continued from previous page*

Old config.	i	j	New config.	Notes
	g	o	L	LC

where

PL	piston-like displacement
SN	snap-off displacement
FF	film formation
NFF	no film formation
LC	layer collapse
LF	layer formation
NLF	no layer formation
FU	film updated
LU	layer updated
o	oil
w	water
g	gas
i	invading phase
j	defending phase

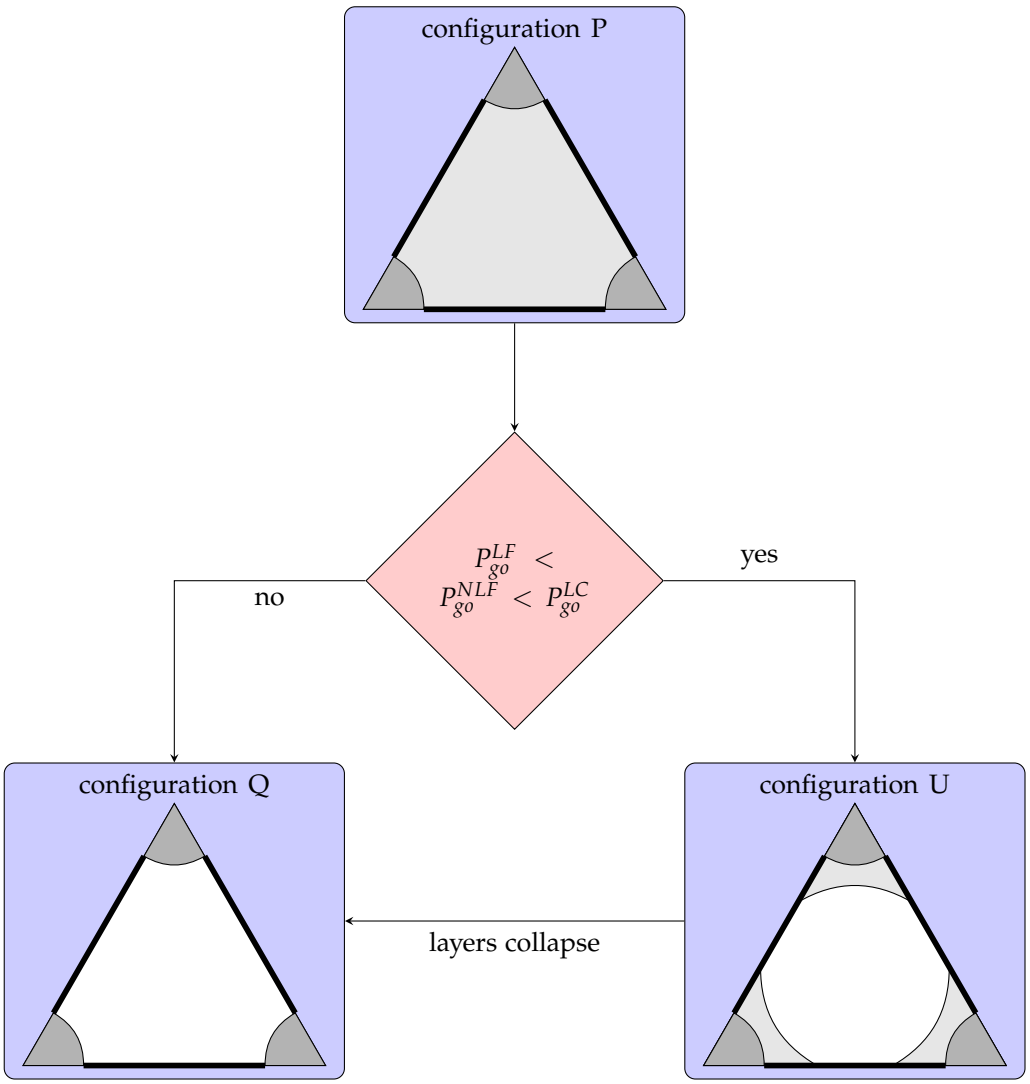

Figure 4.11: Flowchart of the selection of favourable displacement when gas invades oil surrounded by water films in a non-uniformly wetted pore with equilateral triangular cross-section. Where layers were created, layers collapse may follow. Note that the geometrical condition Eq. 4.5 should be satisfied for all new AMs.

4.4 THREE-PHASE CAPILLARY ENTRY PRESSURES

4.4.1 *Thermodynamic criteria*

Accurate modelling of three-phase flow at the pore scale requires determination of the capillary entry pressures that are associated with the phase displacements. This is very important for modelling of oil layers in pores of angular cross-sections. Previous three-phase pore-network models (Piri and Blunt, 2005a,b; Suicmez et al., 2006) modelled these layers based on a geometrical crite-

rion. However, this criterion is not sufficient to accurately predict the oil relative permeability at low oil saturations when the oil flow is controlled by layers (Fig. 1.11). Additionally, novel thermodynamic criteria were introduced by van Dijke et al. (2004a, 2007) for more accurate modelling of oil layers. In this section, we present a brief description of the capillary entry pressures, which have been formulated by van Dijke et al. (2004a, 2007) for displacements at the pore scale.

In the following we give the key general equations that are required to determine the precise capillary pressure for pores of arbitrary wettability for three-phase flow. Then we briefly describe the derivations of the thermodynamic criterion for pores of uniform, but arbitrary wettability.

The three-phase capillary entry pressures are related by:

$$P_{c,gw} = P_{c,go} + P_{c,ow}, \tag{4.18}$$

which can, using the Laplace equation (Eq. 4.6), be written in terms of interfacial tensions and the radii of curvature as:

$$\frac{\sigma_{gw}}{r_{gw}} = \frac{\sigma_{go}}{r_{go}} + \frac{\sigma_{ow}}{r_{ow}}. \tag{4.19}$$

The capillary entry pressures are calculated based on the thermodynamic equilibrium from minimization of the Helmholtz free energy F when one configuration is displaced by another for a small displacement dx along the same pore (e.g. Fig. 4.16) . The free energy change can be expressed as $dF = Gdx$. At equilibrium, the change in free energy $dF = 0$. van Dijke et al. (2004a) and Piri and Blunt (2004) worked out the general formula for the variation of Helmholtz free energy dF, caused by a three-phase displacement in a pore with angular cross-section:

$$\begin{aligned} dF = {} & P_{gw}dV_w + P_{go}dV_o + \sigma_{gw}\left(dA_{gw}cos\theta_{gw}^{MTM}dA_{ws}\right) \\ & + \sigma_{go}\left(dA_{go}cos\theta_{go}^{MTM}dA_{os}\right) + \sigma_{ow}dA_{ow}, \end{aligned} \tag{4.20}$$

where

dV_i the change of volume of phase i

dA_{is} the change of the fluid-solid contact area for phases i

dA_{ij} the change of the fluid-fluid contact area between phases i and j.

The procedure to find the capillary entry pressure is as follows:

1. Determine the new and old configurations for each displacement.

2. Calculate the changes in volume and area as a result of the displacement, taking place from the old and new configuration using the geometrical expression given in appendix A.

3. Solve $dF = 0$ (Eq. 4.20). This equation may require a simple Newton-Raphson method to determine the solutions for some displacements.

4. Use the solution which gives the minimum physically viable capillary entry pressure to be associated with the displacement. By physically viable we mean that the solution must not be larger than the corresponding snap-off value (section 4.4.2) and the geometrical collapse criteria must not be violated.

We give an example of using this procedure in section 4.4.4.

For pores of uniform wettability, van Dijke et al. (2004a) used the energy balance formulation of Mayer and Stowe (1965) and Princen (1969a,b) for two-phase flow to derive a general formula for determination of the precise capillary entry pressures for three-phase flow. They analysed all possible combinations of phase occupancies on either side of the MTM in angular cross-sections of uniform wettability. We briefly describe these derivations:

G is given as a function of the radii of curvature r_{ij}:

$$G(r_{go}, r_{ow}, r_{gw}) = -\sum_{ij=go,ow,gw} \sigma_{ij} g(r_{ij}, \theta_{ij}) \delta_{ij}^{ab} + \sum_{\alpha=1}^{n} \sum_{ij=go,ow,gw} \sigma_{ij} g(r_{ij}, \theta_{ij}) (\delta_{ij}^{(\alpha)^a} - \delta_{ij}^{(\alpha)^b}), \tag{4.21}$$

where

$$\delta_{ij}^{(\alpha)^\beta} = \begin{cases} 1 & \text{if } ij \text{ AM present in corner } \alpha \text{ at } \beta, \\ 0 & \text{otherwise,} \end{cases} \tag{4.22}$$

and where β denotes the cross-sections a and b with different phase occupancies on either side of the MTM

$$\delta_{ij}^{ab} = \begin{cases} 1 & \text{if bulk phase } i \text{ is present at } a \text{ and bulk phase } j \text{ is present at } b, \\ -1 & \text{otherwise.} \end{cases}$$

(4.23)

The geometrical function $g(r_{ij}, \theta_{ij})$ for an angular cross-section is given in Appendix A.

At equilibrium, the change in free energy is $dF = 0$, and hence

$$G = 0. \tag{4.24}$$

Therefore, for one given radius of curvature (e.g. from a previous flood), the two remaining unknown radii of curvature can be calculated by solving Eq. 4.19 and Eq. 4.24.

We have implemented the non-uniform wettability of the pore space as a result of ageing as discussed in section 4.3.2. Under these conditions, oil or gas layers occur in aged oil-wet pores, surrounded by corner water and bulk water or gas phases (see configuration S, T and U, Fig. 4.2). The corresponding thermodynamic criteria for layer collapse have been derived by van Dijke et al. (2007). The first condition for any displacement that includes formation of a new AM is that the AM should satisfy the simple geometrical criterion given in Eq. 4.5.

However, this requires an additional constraint (Eq. 4.7 for $\theta_{ij,h}$) to determine the appropriate contact angles, since in some cases the AM is not a priori known, i.e. when the AM is pinned on unaltered to altered wettability surface (Fig. 4.8).

4.4.2 *Snap-off displacement*

A snap-off displacement refers to an event where a phase occupying the centre of the pore is displaced by another phase surrounding it in the pore corner (i.e. a layer or film of a phase). In a pore with uniform wettability (e.g. configuration J, Fig. 4.2), the radius of curvature is positive and therefore, when the corresponding capillary pressure decreases, the AM moves towards the centre, leading to spontaneous snap-off (Fig. 4.12) when the AMs meet. In a non-uniformly wet pore (e.g. configuration P, Fig. 4.2), if the AM is present on the water-wet surface, then the process of snap-off begins by moving the AM to the centre of the pore. When the AM reaches the point of wettability change, the AM may hinge until the hinging contact angle reaches the contact angle value of the altered wettability

surface θ^{alt}. If $\theta^{alt} < \frac{\pi}{2} - \gamma$, then the AM is forced to move on the altered wettability surface until it meets other AMs at which the pore is filled spontaneously. If $\theta^{alt} > \frac{\pi}{2} - \gamma$, then snap-off takes place immediately (Fig. 4.13).

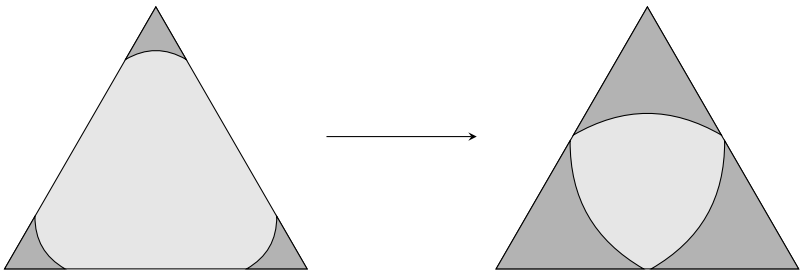

Figure 4.12: Snap-off in an angular pore of uniform wettability.

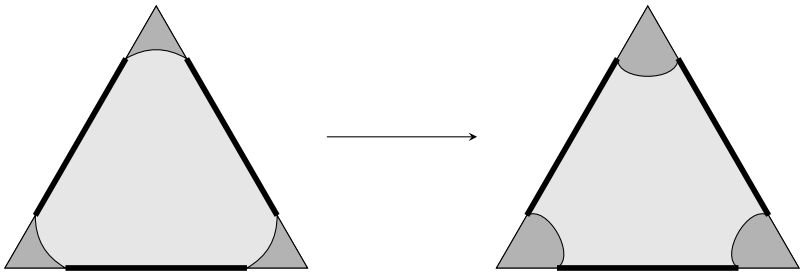

Figure 4.13: Snap-off in an angular pore of non-uniform wettability.

For a regular n-sided angular pore shape, spontaneous snap-off occurs when the whole pore surface becomes contacted by the invading phase from the corners, which is equivalent to $L_s^{(\alpha)} = \frac{L_s}{2n}$. Using Eqs. 4.6 and 4.7, the snap-off threshold capillary pressure is defined as

$$P_{ij}^{sn} = \frac{2n\sigma_{ij}}{L_s} \frac{cos(\theta_{ij} + \gamma^{(\alpha)})}{sin\gamma^{(\alpha)}}. \tag{4.25}$$

However, for snap-off with negative radius of curvature r_{ij}, when the AMs start to move onto the surface of altered wettability, they become unstable, causing the pore to be filled by the invading phase (Fig. 4.13). The corresponding threshold capillary pressure is given by

$$P_{ij}^{sn} = \frac{\sigma_{ij}}{L_s^{dr(\alpha)}} \frac{cos(\theta_{ij}^{sn} + \gamma^{(\alpha)})}{sin\gamma^{(\alpha)}}, \tag{4.26}$$

where $L_s^{dr(\alpha)}$ is defined by Eq. 4.7 and θ_{ij}^{sn} denotes the angle at which collapse of the AMs takes place. $\theta_{ij}^{sn} = \theta_{ij}^{alt}$ if $\theta_{ij}^{alt} \leq \pi - \gamma^{(\alpha)}$ otherwise $\theta_{ij}^{sn} = \pi - \gamma^{(\alpha)}$ (van Dijke et al., 2007).

Finally, note that when the invading phase is present in the center of one of the neighbouring elements, then piston-like displacement is favoured over snap-off.

4.4.3 *Pore body filling*

A pore body filling (PBF) event is defined as a displacement where the non-wetting phase occupying a pore body is displaced by a wetting phase from one or more adjoining pore throats. The process of PBF is complex (Fig. 4.14). The capillary entry pressure of this displacement depends on the number of adjoining pore throats that are occupied by the wetting phase (Lenormand et al., 1983). Different parametric models of pore body filling have been proposed (Blunt, 1997; Øren et al., 1998). The model of Blunt (1998) is used to calculate the capillary entry pressure

$$P_{cap} = \frac{2\sigma\cos\theta}{r_{ins}} - \sigma\sum_{i=1}^{z}(A_i x_i)\,, \tag{4.27}$$

where z denotes the number of adjoining throats that are filled with phases that do not contribute to the invasion of the pore body, σ denotes the interfacial tension, r_{ins} denotes the inscribed radius of the pore, x_i denotes random numbers between 0 and 1, and A_i are arbitrary parameters.

The PBF is similar to piston-like displacement in the situation where there is only one adjoining throat that is occupied by the defending phase, which corresponds to the displacement shown in Fig. 4.14b.

We treated the displacements in pore bodies as piston-like displacements.

4.4.4 *Example of three-phase displacement*

Here we give an example of one displacement to show how the capillary entry pressure is calculated, following the procedure given in section 4.4 to solve Eq. 4.20. We consider a displacement during three-phase flow in a throat with equi-

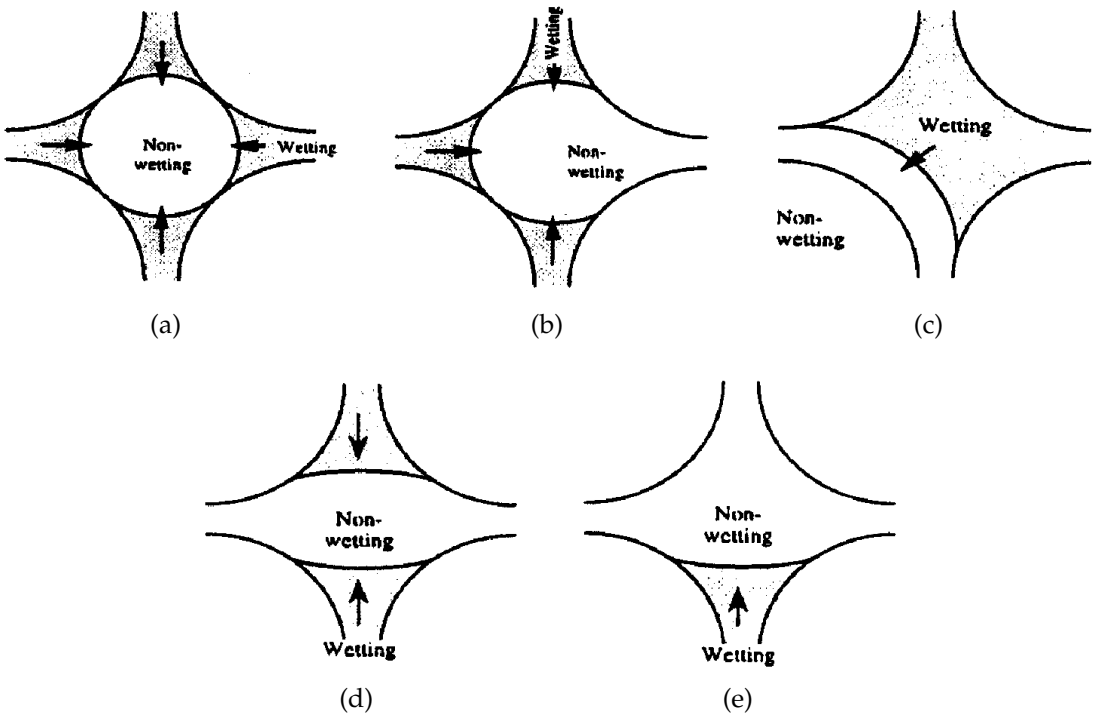

Figure 4.14: Pore body filling events (Blunt, 1997).

lateral triangular cross-section which is occupied by bulk oil and surrounded by water films (configuration P). One of the possible changes of configuration is shown in Figs. 4.15–4.16, where bulk gas displaces bulk oil. All the information of lengths of the unaltered wettability surfaces are taken from the drainage flood and P_{ow} is taken from the water flood. First, we formulate the volume and area changes related to the displacement:

$$dA_{ws} = n\left(L_s^{(\alpha)}(r_{gw}, \theta_{gw}^{AM1}) - L_s^{(\alpha)}(r_{ow}, \theta_{ow}^{AM1})\right) dx \tag{4.28a}$$

$$dA_{os} = -\left(L_s - nL_s^{dr}\right) dx \tag{4.28b}$$

$$dA_{gs} = (L_s - nL_s^{(\alpha)}(r_{gw}, \theta_{gw}^{AM1}))dx \tag{4.28c}$$

$$dA_{ow} = -nL_f^{(\alpha)}(r_{ow}, \theta_{ow}^{AM1})dx \tag{4.29a}$$

$$dA_{go} = 0 \tag{4.29b}$$

$$dA_{gw} = nL_f^{(\alpha)}(r_{gw}, \theta_{gw}^{AM1})dx \tag{4.29c}$$

$$dV_w = \left(nA^{(\alpha)}(r_{gw}, \theta_{gw}^{AM1}) - nA^{(\alpha)}(r_{ow}, \theta_{ow}^{AM1})\right) dx \tag{4.30a}$$

$$dV_o = -\left(A - nA^{(\alpha)}(r_{ow}, \theta_{ow}^{AM1})\right) dx \tag{4.30b}$$

$$dV_g = \left(A - nA^{(\alpha)}(r_{gw}, \theta_{gw}^{AM1})\right) dx \tag{4.30c}$$

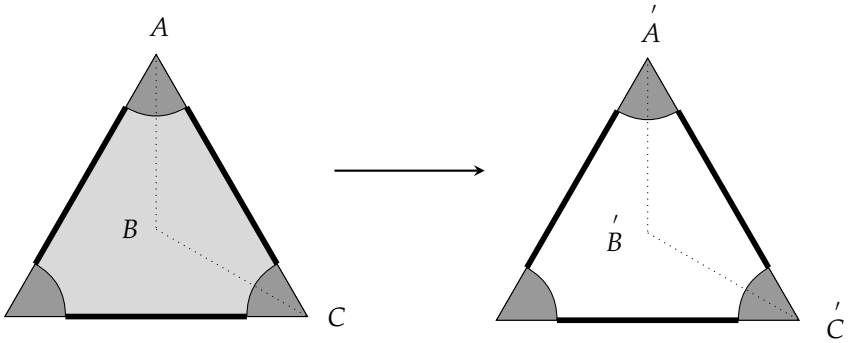

Figure 4.15: Gas displaces oil surrounded by water films in a pore with equilateral triangular cross-section, displacement P→Q, Fig. 4.2. Dark gray denotes water, light gray denotes oil, white denotes gas and bold lines denote the surfaces of altered wettability.

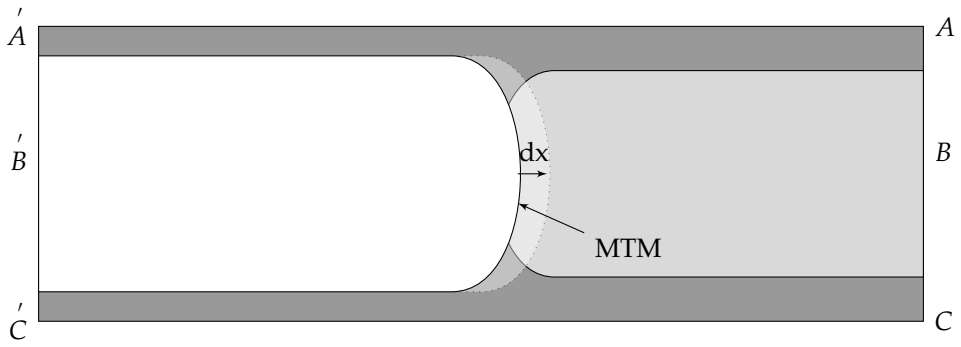

Figure 4.16: Cross-section in a pore showing a small displacement dx of the MTM, corresponding to Fig. 4.15.

Eqs. 4.28–4.30 are substituted for the volume and area terms in Eq. 4.20. The oil-water capillary pressure, P_{ow}, and $\theta_{ow,h}$ are obtained from the previous flood from which r_{ow} can be calculated using Eq. 4.7. At the MTM, the contact angles are taken as the contact angles of the altered wettability surface: $\theta_{go}^{MTM} = \theta_{go}^{alt}$ and $\theta_{gw}^{MTM} = \theta_{gw}^{alt}$. However, it is not known whether the new gas-water AM will sit on the water-wet surface, the altered wettability surface, or will be pinned with hinging contact angle $\theta_{gw,h}$. Therefore, the term $\cos\theta_{gw}^{MTM} dA_{ws}$ is split between the two surfaces as

$$cos\theta_{gw}^{MTM} dA_{ws} = cos\theta_{gw}^{w} dA_{ws}^{w} + cos\theta_{gw}^{alt} dA_{ws}^{alt}, \tag{4.31}$$

where

$$dA_{ws}^{w} = n\left(L_s^{(\alpha)}(r_{gw}, \theta_{gw}^{w}) - L_s^{dr}\right) dx, \tag{4.32}$$

and

$$dA_{ws}^{alt} = n\left(L_s^{dr} - L_s^{(\alpha)}(r_{ow}, \theta_{ow,h})\right) dx. \tag{4.33}$$

The additional constraint in Eq. 4.34, relates the two unknowns r_{gw} and $\theta_{gw,h}$, is taken.

$$L_s^{dr} = r_{gw}\frac{cos(\theta_{gw,h} + \gamma^{(\alpha)})}{sin\gamma^{(\alpha)}}, \text{ for } \theta_{gw}^{w} < \theta_{gw,h} < \theta_{gw}^{alt}. \tag{4.34}$$

We used a simple Newton-Raphson method to solve Eq. 4.20, resulting in two solutions of r_{gw}, which were tested against the snap-off radius of curvature

(section 4.4.2) to determine the final solution. This solution is used to calculate the capillary pressure, $P_{c,gw} = \frac{\sigma_{gw}}{r_{gw}}$, and $P_{c,go}$, using Eq. 4.18.

4.5 MODELLING OF THE MULTIPLE DISPLACEMENTS

The network consists of (phase) clusters of interconnected pores that accommodate the same phase as defined in section 4.1. The pressure within each cluster is uniform. The cluster pressures are determined through the entry pressures of the pores, as described in sections 4.3–4.4, at the boundaries between the network clusters. These clusters can be connected to the inlet, the outlet, both, or not connected to either the inlet or the outlet. The latter are called disconnected clusters. If these disconnected clusters are formed during two-phase flow, they are usually trapped and immobile (Ryazanov et al., 2009). However, disconnected clusters are very common to form during three-phase flow (e.g. WAG injection). These disconnected clusters of oil, water or gas which are formed during different floods, has been observed to move by multiple displacements during three-phase flow (Sohrabi et al., 2000, 2001, 2004), Fig. 4.17.

Fig. 4.18 shows the (bulk) fluid distributions in the pore-network. Note that films and layers are not displayed on the pore-network but pores that contain only film or layer of a phase are still part of the corresponding phase clusters. Layers and films play a crucial role in connecting large (bulk) clusters, providing pathways between clusters. Layer collapse could lead to break up of clusters and possibly forming smaller, disconnected clusters. Fig. 4.18 can be simplified as map of clusters (Fig. 4.19), taking gas as invading phase at the inlet. The arrows indicate a possible cluster-cluster invasion. Note that there is no cluster that can invade cluster (1). This is because cluster (1) is the inlet invading cluster and hence its pressure is always increasing relative to one or more of the outlet connected clusters, (5), (8) and (9). The latter type of clusters are always defending clusters only, indicated by arrows into them.

Two types of displacements can occur:

1. Single displacement: This is a direct displacement during which a phase cluster connected to the inlet displaces a phase cluster connected to the outlet. If we consider an idealised map of the phase distribution within a

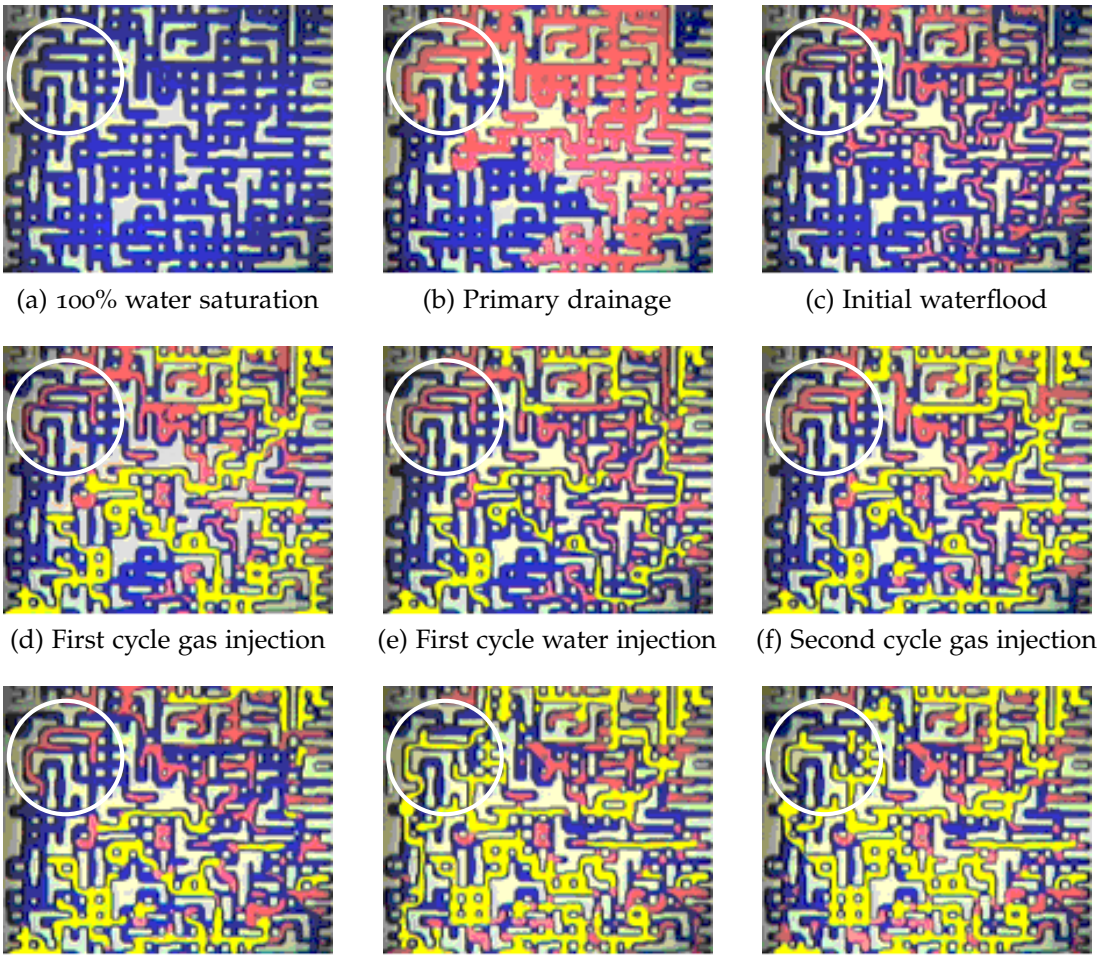

(a) 100% water saturation (b) Primary drainage (c) Initial waterflood

(d) First cycle gas injection (e) First cycle water injection (f) Second cycle gas injection

(g) Second cycle water injection (h) Fifth cycle gas injection (i) Fifth cycle water injection

Figure 4.17: An example of a section of the micromodel, showing the fluid distributions after different floods. The oil cluster in the white circle is formed initially during primary drainage (b). It becomes disconnected (completely surrounded by water) during second cycle water injection (g). However after a few WAG cycles (h), the cluster has moved out (captured by the reported videos of the experiment) of the system by multiple displacement. Blue denotes water, oil denotes red and yellow denotes gas. Note that the micromodel was scanned vertically in separate sections. What shown here is only the image of the middle section at the end of different floods. Images taken from Sohrabi et al. (2000).

network (Fig. 4.19), then a possible single displacement is when the inlet connected gas cluster (1) displaces the outlet connected oil cluster (5).

2. Multiple displacement: This is an extension of the double displacement during which a phase cluster connected to the inlet displaces a disconnected phase cluster, which displaces a phase cluster connected to the outlet. For example, in Fig. 4.19, a possible multiple displacement involves gas cluster (1), connected to the inlet, displacing the disconnected oil cluster (2),

which in turn displaces the disconnected gas cluster (6), which displaces oil cluster (8), connected to the outlet. In section 4.5.3, we explain how to find the preferred displacement chain such that the sum of the capillary entry pressures at the boundaries between the clusters from the inlet to the outlet is the lowest.

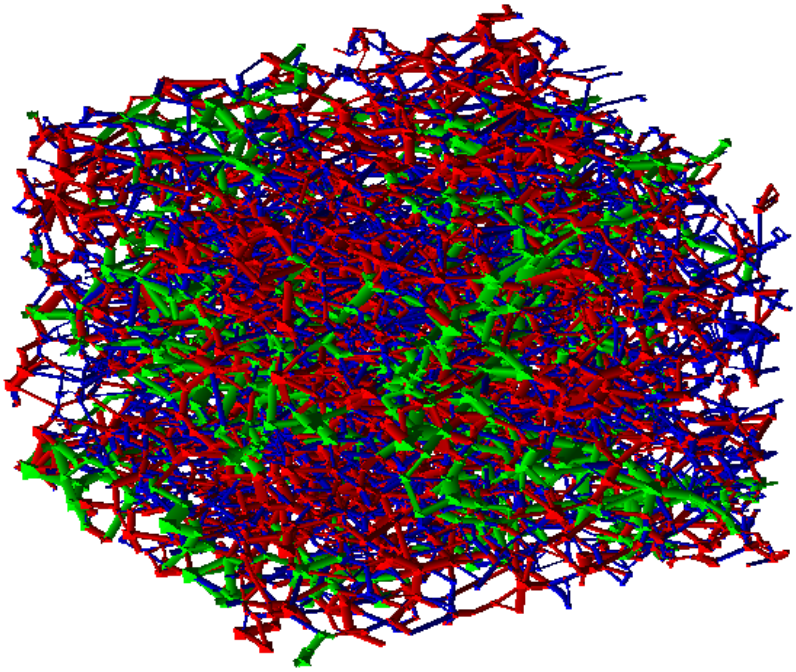

Figure 4.18: Fluid distribution as phase clusters in a pore-network. Blue denotes water, red denotes oil and green denotes gas. The phase clusters can be represented as a conceptual map (Fig. 4.19). Note that films and layers are not displayed in this figure.

4.5.1 *Partial volume filling*

As a result of the multiple displacement mechanism, the network will have pores that are partially filled by different fluids. A multiple displacement leads to a change in the volumes of the phases in all pores that are part of the displacement chain. Over the entire displacement chain, we calculate which pore filling requires the smallest phase displacement. We use this minimum volume to fill the pores in the chain, leading to a change in the configuration of the pore with the smallest phase displacement. The configurations of other pores in the chain remain unchanged unless the volume of displacement phase in the pore becomes negligible, which is determined by a cut-off value. In this case, the pore configuration changes to a new one.

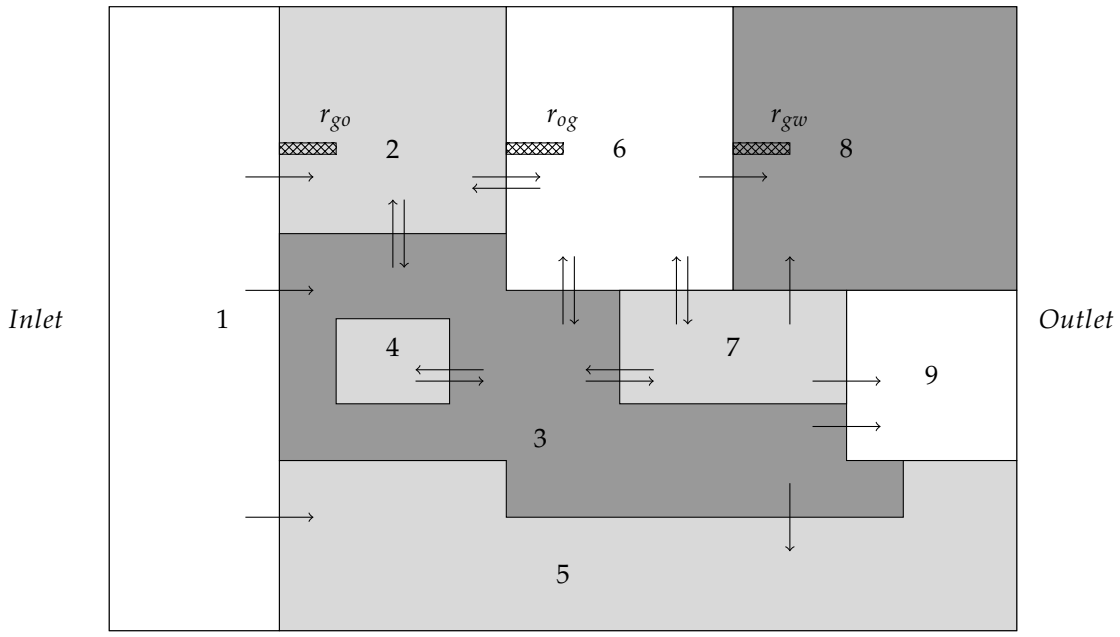

Figure 4.19: Conceptual map of a network of phase clusters with cluster-cluster connections, showing their connectivity to inlet and outlet. Dark gray denotes water, light gray denotes oil and white denotes gas. A possible multiple displacement chain, involving clusters 1, 2, 6 and 8, is indicated by the pores that are labelled by the entry radii r_{go}, r_{og} and r_{gw}, correspoinding to minimum capillary entry pressures, at cluster-cluster interfaces. A possibele single displacement could occur though the invasion of gas cluster 1 to oil cluster 5. Arrows indicate the direction of invasions, i.e. invading and defending clusters.

For instance, consider the triple displacement chain involving clusters 1, 2, 6 and 8 in the phase cluster map of Fig. 4.19. The displacement chain takes place through the pores at cluster-cluster interfaces (indicated in Fig. 4.19). It comprises gas (at the inlet) displacing oil, then oil displacing gas and then gas displacing water through the outlet, shortly $g \rightarrow o \rightarrow g \rightarrow w$. Let us consider that the pores (configuration) of lowest capillary pressure for each cluster-cluster interface over the entire displacement chain are P, R, A in Fig. 4.2, respectively. Then, we first calculate the volume difference to complete the displacement (P→U, R→H, A→L) for each pore in the chain. We select the smallest phase displacement to cause a change in the pore configuration. This could be, for example, the volume of the oil phase due to layer formation displacement in displacement P→U. The phase volumes of all pores in the chain will change but only the configuration of pore P will change to the new configuration U.

To conserve the volume of the individual phases, we take the detailed film and layer configurations into account by allowing each pore to have volumes for

each type of phase occupancy (see Eq. 3.15 in section 3.5). We also describe some issues resulting from partial volume filling in section 4.5.5.

4.5.2 *Outlet boundary conditions*

We impose pressures at the outlet boundary for each phase by the pressure differences P_{ij}^{out}, where $ij = go, ow, gw$. We assume that the network model represents an entire micromodel or core sample, for which the pressure difference between the two phases other than the invading phase P_{ij}^{out} is kept constant. The other pressure differences for outlet clusters are assumed to be equal to the target pressure difference of the latest chain of displacements. For instance, during gas injection, the gas pressure increases, whereas the pressures of oil and water clusters at the outlet remain constant. Therefore, the pressure difference between oil and water P_{ow}^{out} is kept constant (taken from the previous flood), whereas the other two pressure differences P_{go}^{out} and P_{gw}^{out} vary based on the target pressure of the latest chain of displacements.

4.5.3 *Shortest path algorithm*

The multiple displacement events involve a chain of clusters where the beginning of the chain is the inlet invading phase cluster and the end is a cluster connected to the outlet. This means that there are many possible chains. To find the most favourable displacement chain in the network during the three-phase invasion-percolation process, we use a computationally efficient shortest path search algorithm (van Dijke et al., 2008).

Initially, the map of network phase clusters with cluster-cluster connections (such as Fig. 4.19) is converted to a graph (Fig. 4.20). We have added a virtual cluster of a chosen reference phase at the outlet (section 4.5.2). Connections between clusters connected to the outlet and the virtual cluster have been added. These connections represent P_{ij}^{out}, the difference between the pressure in the outlet connected cluster in the chain with phase i and the pressure in the reference outlet phase j. First, we find the pore with lowest capillary entry pressure (section 4.4) for each cluster-cluster connection of the graph. Then we use a "shortest-

path" tree-search algorithm (Algorithm 4.1) to find the minimum target pressure difference between the invading phase at the inlet and the reference phase at the outlet. For instance, in the multiple displacement $g \rightarrow o \rightarrow g \rightarrow w$ that was considered in the previous section, the target pressure difference between gas, the invading phase at the inlet, and oil, assuming that oil is the reference phase at the outlet, is

$$P_{go}^{trgt} = P_{c,go} + P_{c,og} + P_{c,gw} + P_{wo}^{out}. \tag{4.35}$$

In general, for a multiple displacement chain that consists of n clusters $(x_1, x_2 \dots x_n)$ with invading phase cluster x_1 at the inlet and reference (virtual) cluster x_{ref} at the outlet, the target pressure difference $P_{x_1 x_{ref}}^{trgt}$ is given by

$$P_{x_1 x_{ref}}^{trgt} = P_{c,x_1 x_n}^{eff} + P_{x_n x_{ref}}^{out}, \tag{4.36}$$

where $P_{c,x_1 x_n}^{eff}$ is the sum of the capillary entry pressures for the clusters along the displacement chain, given by

$$P_{c,x_1 x_n}^{eff} = \sum_{e=1}^{n-1} P_{c,x_e x_{e+1}}, \tag{4.37}$$

where $P_{c,x_e x_{e+1}}$ is the lowest capillary entry pressure between invading cluster x_e and defending cluster x_{e+1}.

The clusters of the network are represented by the list V of vertices (clusters) v. The cluster-cluster connections are represented by the list E of edges e. The distance of each edge is the lowest capillary entry pressure between the invading cluster and the defending cluster that are connected by the edge. The distance of the edges that connect the outlet clusters with the virtual outlet cluster is P_{ij}^{out}. The invading inlet cluster is used as the source vertex s and the virtual outlet vertex (cluster) is r. Therefore, the problem of determining the displacement chain with the minimum target pressure difference becomes finding the path from s to r that has the minimum distance. The classic Bellman-Ford-Moore (BFM) algorithm (Bellman, 1958; Ford, 1956; Moore, 1959) is normally used to solve the shortest path problem. However, a common feature occurs during finding the shortest path from s to r, the so-called negative (distance/cost) cycle. The nega-

tive cycle occurs when a closed loop of displacement chain has a negative effective pressure difference (Eq. 4.37). The displacement within the negative cycle is equivalent to a spontaneous displacement. Despite that BFM algorithm indicates the presence of negative cycles, BFM algorithm can not locate them (Cherkassky and Goldberg, 1999). van Dijke et al. (2008) used a cycle detection strategy in combination with Tarjan's subtree disassembly algorithm (Tarjan, 1981). The shortest path algorithm used in this work is capable of detecting the negative cycles and can resolve them (van Dijke et al., 2008). If negative cycles are not detected, the algorithm produces the shortest path from s to every vertex v in graph G.

The shortest path algorithm is presented in Algorithm 4.1. In brief, the algorithm takes graph G as input, which consists of V and E. The task is to determine the minimum cost/distance from s to all other vertices. There are two lists: A is the list of vertices which will be scanned in the current pass, B is the list of vertices which will be scanned in the next pass. Initially, the algorithm assigns a distance, i.e. target pressure difference, $d(s) = 0$ to the source vertex, i.e. the inlet cluster, and distance $d(v)$ of infinity for all other vertices (algorithm 4.2). Then s is added to B. At the beginning of every pass, all the vertices are transferred from B to A. The algorithm takes every vertex u in the list A for a scanning process. In the scanning process, every edge from vertex u to vertex v is checked. If the distance $d(v)$ can be shortened by summing up the distance for u plus the distance $l(u, v)$ for the edge between u and v, then v is updated. The algorithm checks first if u is one of the descendants of v, i.e. the subtree ($L_{children}(v)$) of shortest paths rooted in vertex v is traversed (Algorithm 4.3). If u is found in $L_{children}(v)$, a cycle is created. The cycle is located and the algorithm reports it and stops. The cycle is resolved by carrying out the displacement along it. However, if the vertex u is not found, $L_{children}(v)$ is cleared (i.e. disassembled in Algorithm 4.4) and v is added to $L_{children}(u)$. If v is not scanned and not in the current scanning list A, then it will be added to A so it can be scanned in the current pass. Otherwise, v will be added to B for the next pass. At the end of the scanning process for u, u is marked scanned and removed from the current scanning list A. When A becomes empty, a pass is completed. The next pass starts by transferring all the vertices from B to A. The algorithm stops when B is empty at the end of a pass.

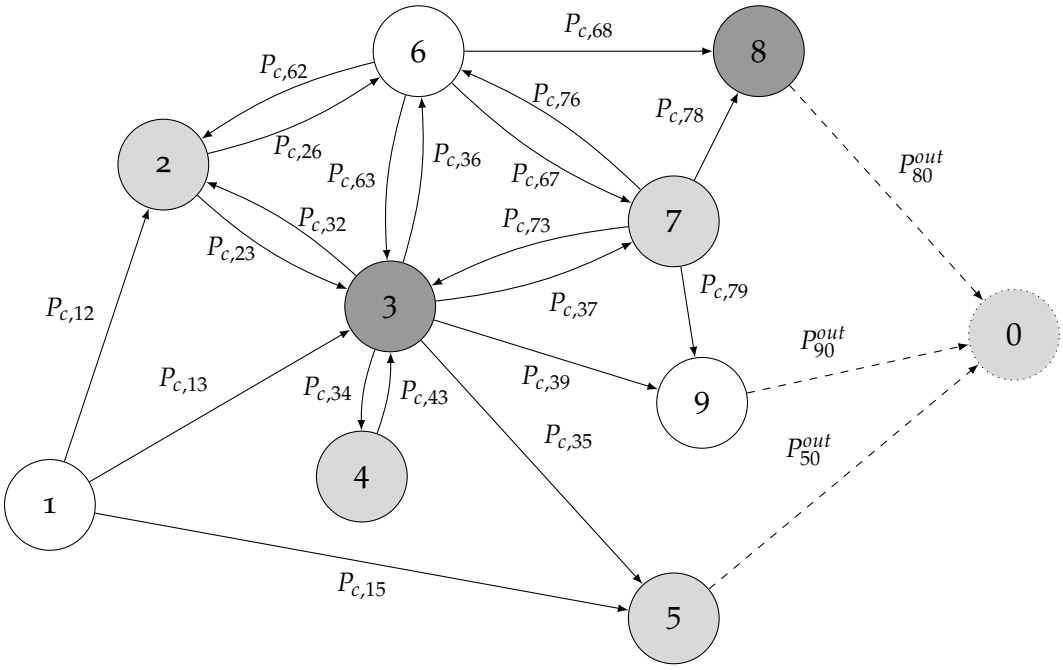

Figure 4.20: The equivalent graph for the map of network phase clusters in Fig. 4.19. Clusters are presented as vertices connected by edges. An additional (virtual) vertex is added to represent the outlet (reference phase). Edges represent the cost for each direction of each cluster-cluster connection.

4.5.4 *Pressure determination of each cluster*

As mentioned above, one of the advantages of using the shortest path algorithm is that it provides the shortest path tree from the source vertex, the invading cluster to all other other vertices, phase clusters. Knowing the reference pressure (P_{ref}^{out}) of the outlet (vertex 0 in Fig. 4.20), the pressures of the clusters along the entire displacement chain can be calculated recursively by retracing the shortest path from the outlet to the inlet:

$$P_i = P_j + P_{c,ij}, \tag{4.38}$$

where ij denote connections that are part of the shortest path chain, starting with the reference outlet cluster. By doing so, the pressure of the invading cluster (marked 1) can be determined and, hence, the pressures of all other clusters can be calculated by traversing the shortest path tree from the inlet using Eq. 4.38, starting with the invading cluster, i.e. of the source vertex.

For instance, Fig. 4.21 shows the solution for a possible shortest path tree of the graph (Fig. 4.20). We give arbitrary pressure for the reference phase cluster

$P_0^{out} = 0$. Then we calculate the cluster pressures through the shortest path chain, indicated in red colour backward from reference outlet cluster 0 to the inlet cluster 1 as follows: $P_8 = P_0 + P_{80}^{out}$, $P_6 = P_8 + P_{c,68}$, $P_2 = P_6 + P_{c,26}$ and finally $P_1 = P_2 + P_{c,12}$. Now the cluster pressures along the chain are known and therefore the cluster pressures along the branches, indicated in blue colour, of the main chain can be calculated as follows: $P_7 = P_6 - P_{c,67}$, $P_9 = P_7 - P_{c,79}$, $P_3 = P_2 - P_{c,23}$, $P_4 = P_3 - P_{c,34}$ and $P_5 = P_3 - P_{c,35}$.

When a negative cycle is detected by the shortest path algorithm, no pressure calculation is performed because of the absence of a shortest path from the inlet to the outlet. Therefore, apart from pressure changes arising from merger or break-up of clusters that may occur during resolution of the negative cycle, we do not update the pressure of the network clusters during a spontaneous displacement. This will enable us to avoid any instabilities in the presence of films and layers. Previous authors like Piri and Blunt (2005a) and Suicmez et al. (2007) considered similar decisions in their models. Note that they only considered single and double displacements and, hence, they do not encounter the problem of negative cycles.

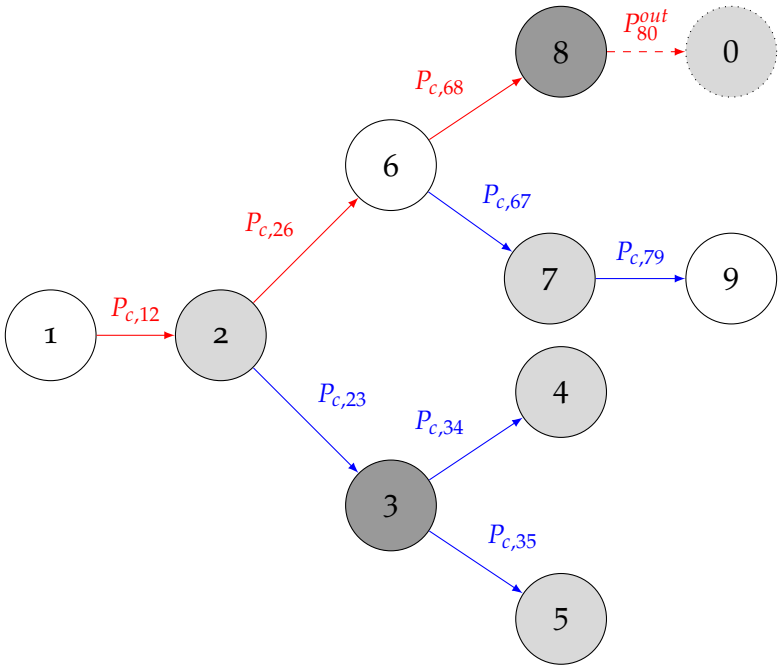

Figure 4.21: A possible shortest path tree of the graph shown in Fig. 4.20.

4.5.5 *Computational Issues*

Here we list some of the computational issues that have been encountered during the network modelling of the three-phase flow:

1. Cluster disappearing: This feature arises during the partial volume filling as a result of multiple displacements. This situation occurs when there is a cluster in the displacement chain, consisting of one element only that carries the smallest phase displacement volume (section 4.5.1). For instance, consider the situation in Fig. 4.22. Three elements are involved in a double displacement during gas flood: element e1 belongs to an inlet gas cluster, element e2 belongs to a disconnected oil cluster and element e3 belongs to an outlet water cluster. If e2 requires the smallest phase volume to complete the displacement, then oil is displaced completely by gas from e2 and thus e2 is removed from oil cluster and added to the gas cluster. However, e3 is partially filled by oil because the oil volume is not large enough to complete the displacement in e3. Thus it will not be added to the oil cluster yet. This means that there is no element that belongs to the oil cluster, i.e. the cluster is empty, at the end of this multiple displacement. Therefore, the oil cluster is removed from the network clusters list. However, the volume of oil in e2 is preserved (see section 3.5). This allows to resume the pore filling of e3 by oil if it is invaded by another oil cluster ("rescue cluster") at some point during the current flood or subsequent floods. The volume of oil in the element will increase until, eventually, the displacement is completed. This feature is not common to happen (not before the first WAG cycle at least) and thus it does not have a significant impact on the overall results.

2. Merger of clusters and fluid re-distribution: One of the key features of the multiple displacement in three-phase flow is that all the clusters within the network can move, i.e. are active. This increases the possibility of merger and breakup of clusters. For instance, a series of multiple displacements (g→o→w→o) involving clusters (1), (2), (3) and (5), see Fig. 4.19, could cause cluster (2) to move towards the trapped cluster (4) and eventually reach cluster (4) and merge with it. Additionally, this multiple displacement could break cluster (5), by invasion of cluster (3), into two smaller

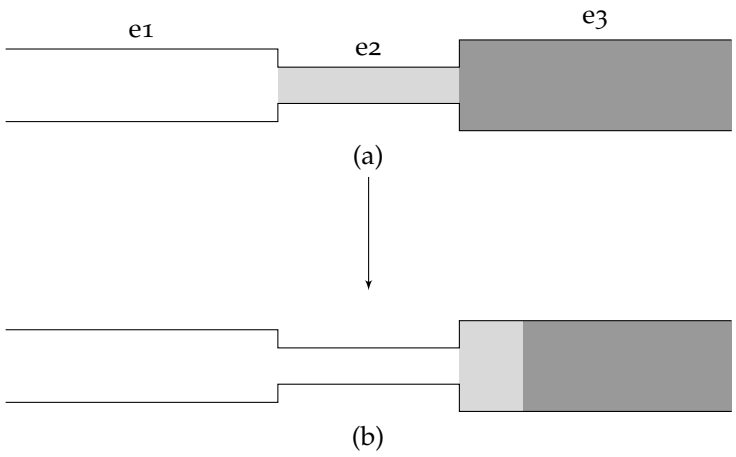

Figure 4.22: Conceptual double displamcement, $g \rightarrow o \rightarrow w$, where the displacement in e2 is completed. (a) 3 elements belong to three different cluster, (b) 3 elements belong to two clusters. Dark gray denotes water, light gray denotes oil and white denotes gas.

clusters, one disconnected cluster and another cluster connected to the outlet. In particular, merger of clusters could cause a change in the pressure of the involved clusters. If the pressure of a disconnected cluster changes, the phase volumes (film/layer/bulk) in the pore or throat that is connected to this cluster should change. In other words, the volume of the cluster should be redistributed between its elements, leading to change in the phase volume in the cluster elements. This implies that the volumes of the other phases in these elements need to be adjusted. This requires volume redistribution for the merged clusters and their neighbouring clusters. This might be more accurate but is difficult to implement and computationally expensive. Additionally, the pressure change of the cluster could lead to another chain of displacements, possibly starting from a disconnected cluster where layers could collapse and trigger a chain of displacements, which is not part of main chain that was found by shortest path algorithm.

3. Pressure of trapped film cluster: Updating the pressure of a trapped water cluster in which none of its element has a bulk water (Fig. 4.23a). In a more complicated case, this film cluster could be interacted with more than one cluster (Fig. 4.23b). The issue arises during the construction of the graph, which is used to find the shortest path and update clusters pressures (section 4.5.4), because such disconnected (film) cluster has no incoming (and thus no outgoing) edges (arcs) in the graph. In other words, the cluster

is isolated in the graph. The pressure of the film trapped cluster will be changed by the same amount of the pressure change in the trapping cluster. If it is trapped by more than one cluster, then the cluster with the maximum pressure (or the cluster with maximum pressure change) will be considered as the trapping cluster. However, given that the network is initially filled with water (strongly water-wet), water is likely to be connected by the films through the network and therefore the formation of trapped film cluster is rare to occur and, if it happened, it usually produce small clusters. In other words, the effect of this issue is negligible and does not have a noticeable impact on the overall results.

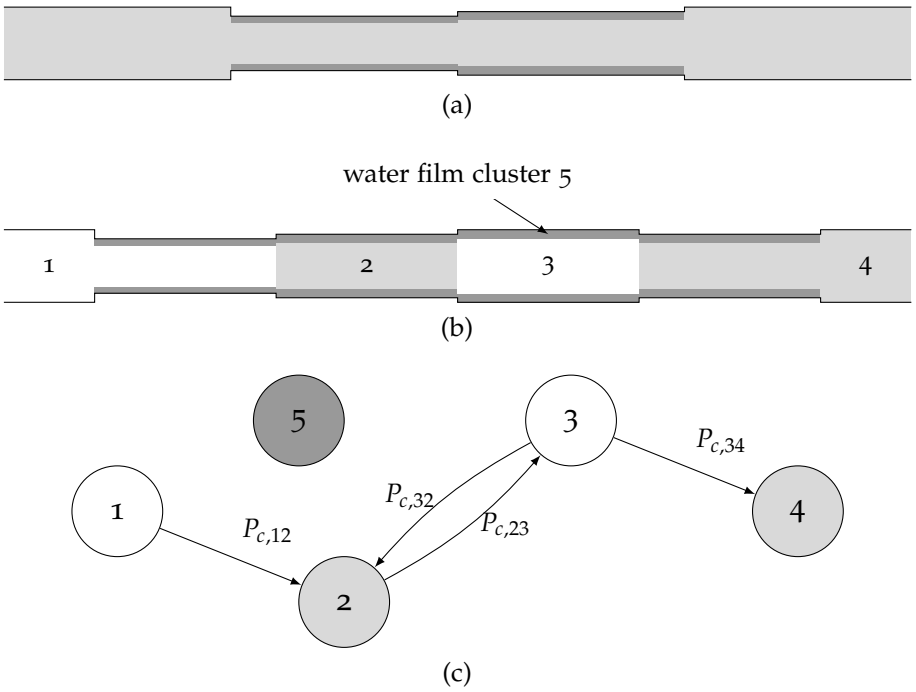

Figure 4.23: (a) Film water cluster is trapped by One (oil) cluster. (b) Film water cluster is trapped by four clusters. (c) The equivalent graph for phase clusters in (b). Clusters are presented as vertices, connected by edges. Edges represent the cost for each direction of each cluster-cluster connection. Dark gray denotes water, light gray denotes oil and white denotes gas.

The computational issues that we encountered are not limited to the ones we mentioned in this section. The purpose of this section is just to show that implementing pore-scale physics (e.g. multiple displacement) is a non-trivial exercise, which requires careful treatment of the pressure and the volume conservation for a disconnected phase that can be present as bulk, film or layer.

Algorithm 4.1: Shortest Path Algorithm

Data: Graph $G = (V, E)$, Start $s \in V$
Result: The minimum distance between each vertex ($s \in V$) and s

initialization; `// shown in Algorithm 4.2`
while $B \neq \emptyset$ **do**
    A=B
    $B \leftarrow \emptyset$
    while $A \neq \emptyset$ & $cycle = false$ **do**
        `// Scan the current first vertex` u `from List` A
        scan (u)
            foreach $e(u, v) \in E_{out}(u)$ **do**
                if $d(u) + l(u, v) < d(v)$ **then**
                    if $L_{children}(v) \neq \emptyset$ **then**
                        CheckSubtree(u,v) given by Algorithm 4.3
                    end
                    if $p(v) > 0$ **then**
                        remove v from $L_{children}(p(v))$
                    end
                    $inE(v) \leftarrow e(u, v)$
                    add v to $L_{children}(u)$
                    $d(v) \leftarrow d(u) + l(u, v)$
                    $p(v) \leftarrow u$
                    Disassembly(v)
                        `// Disassembly the subtree rooted at vertex v using Algorithm 4.4.`
                    end
                    if $v \notin A$ & $v \notin B$ **then**
                        `// Check if vertex v is going to be scanned`
                        if $S(v) \neq scanned$ **then**
                            add v into A
                        else
                            add v into B
                        end
                    end
                end
            end
            remove u from A
            $u \leftarrow scanned$
        end
    end
end

Algorithm 4.2: Initialization

```
Initialization
    A ← ∅ B ← ∅
    foreach v ∈ V do
        p(v) ← 0
        d(v) ← ∞
        S(v) ← unscanned
        E_children(v) ← ∅
        inE(v) ← 0
        if v = s then
            d(s) ← 0
            add s to B
        end
    end
end
```

Algorithm 4.3: Check that u is not one of descendants of vertex v

```
CheckSubtree(u,v)
    forall the w ∈ L_children(v) do
        if w=u then
            cycle ← true
            // Stop, report and resolve ! break
        else
            CheckSubtree(u,w)
        end
    end
end
```

Algorithm 4.4: Disassembly the subtree rooted at vertex v

```
Disassembly(v)
    Remove v from A and B
    foreach m ∈ L_children(v) do
        Disassembly(m) // Disassembly the subtree rooted at vertex m
        p(m) ← 0
        d(m) ← ∞
    end
    L_children(v) ← ∅
end
```

4.6 SUMMARY AND CLOSING REMARKS

In this chapter we have described the two most important advancements in the current model. These comprise the implementation of a thermodynamic criterion for oil layer formation and collapse and multiple displacement chains. We have presented all possible fluid configurations in the cross-section of an angular pore with equal corners that may arise during three-phase flow, including surfaces with uniform wettability and surfaces with non-uniform wettability. The displacement processes that occur at the reservoir scale have been modelled at the pore scale, including primary drainage, imbibition and WAG injection. For the latter, we have presented all possible fluid configuration changes at the pore-level for a pore with angular cross-section. The shortest path algorithm, used to model multiple displacements, has been described. This algorithm is capable of detecting the negative cycles, which correspond to the spontaneous displacements at the pore-scale. Additionally, the algorithm is used to determine the pressure of the network clusters.

5

COMPARISON OF NETWORK SIMULATIONS WITH EXPERIMENTAL DATA

5.1 INTRODUCTION

In the previous chapter, we described our new pore-network model in detail. This chapter presents the model validation against experimental data. The two-phase flow routine of the model is based on the work by Ryazanov et al. (2010), so we revisit the previous validation of the two-phase pore-network model conducted by Ryazanov et al. (2010) for different wetting systems. Ryazanov et al. (2010) had run an extensive validation analysis of the model, using the water-wet, oil-wet and mixed-wet two-phase experimental results of Oak (1990), Valvatne and Blunt (2004) and Jadhunandan and Morrow (1995) respectively.

For three-phase flow, we use the experimental results of Oak (1990) for a water-wet system to validate the model. First, we obtain the contact angles from two-phase matching. Then, the contact angles are used for three-phase simulations. After that, we compare the measured and predicted three-phase relative permeabilities for the water-wet system.

To benchmark the model for oil-wet systems, we use the micromodel experiments of Sohrabi et al. (2000, 2001, 2004). We generate different realisation of 2D network model with properties that are statistically similar to those of the full micromodel. Then we compare the predicted and measured recovery profiles and fluid distributions. Moreover, the effect of the advancements in our model is demonstrated by comparing our network validation results with those of previously published network models.

5.2 PREVIOUS TWO-PHASE VALIDATION OF THE MODEL

5.2.1 *Water-wet system*

Fig. 5.1 shows the two-phase relative permeability calculations of Ryazanov et al. (2010) for a water-wet system, which were used to match the relative permeabilities of the experiments conducted by (Oak, 1990) on water-wet Berea sandstone. Ryazanov et al. (2010) used Network A, described in section 3.2. For the primary drainage, Ryazanov et al. (2010) imposed a constant contact angle, $\theta_{ow}^{dr} = 0^o$, reflecting strongly water-wet system. During water flood, the oil-water contact angles were uniformly distributed between 56^o and 76^o. The simulated relative permeabilities during the primary drainage and water flood were in a very good agreement with the experimental data (Fig. 5.1). These predictions were similar to those of Valvatne and Blunt (2004).

5.2.2 *Oil-wet system*

To validate the model for an oil-wet system, Ryazanov et al. (2010) used oil-wet sandstone data modelled by Valvatne and Blunt (2004). The BereaPB network (Fig. 3.1) was modified, following the approach used by Valvatne and Blunt (2004). They matched the experimental drainage capillary pressure curve by adjusting the pore and throat size distributions. The difference between the models of Ryazanov et al. (2010) and Valvatne and Blunt (2004) concerns criteria for existence of oil layers, discussed in section 4.3.3. Ryazanov et al. (2010) used the thermodynamic criterion as opposed to the geometrical criterion used by Valvatne and Blunt (2004).

Initially, Ryazanov et al. (2010) used the same wettability scenario as Valvatne and Blunt (2004): contact angles were uniformly distributed between 20^o and 60^o during drainage (oil flood) and uniformly distributed between 90^o and 173^o during the water flood. All input parameters are as shown in Table 5.1 (case 1).

The prediction of relative permeability by Valvatne and Blunt (2004) and Ryazanov et al. (2010) were very good (Fig. 5.2). Valvatne and Blunt (2004) slightly overpredicted the oil relative permeability at high water saturation. Furthermore, it un-

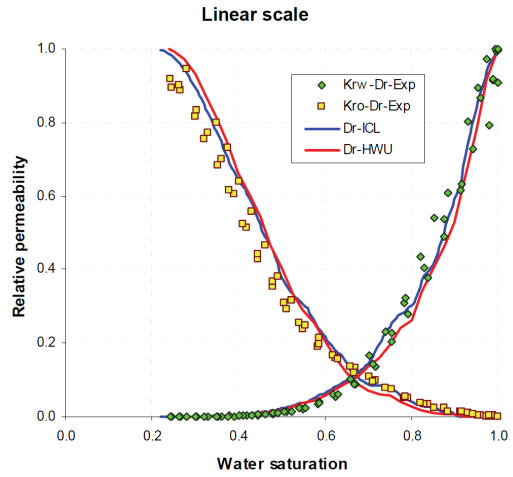

(a) Two-phase relative permeabilities during primary drainage

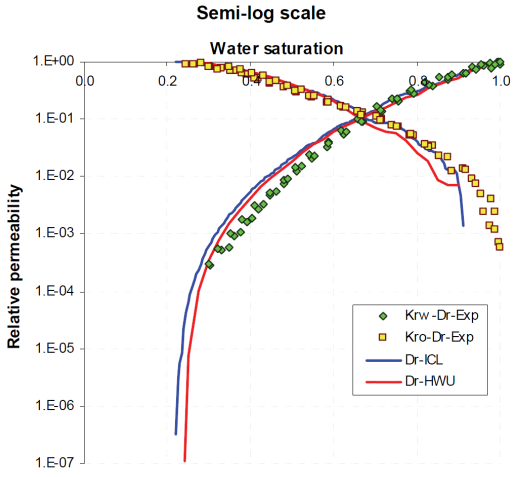

(b) Two-phase relative permeabilities during primary drainage on semi-log scale

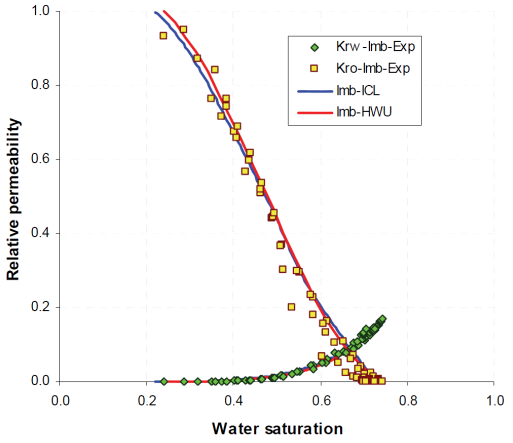

(c) Two-phase relative permeabilities during Imbibition

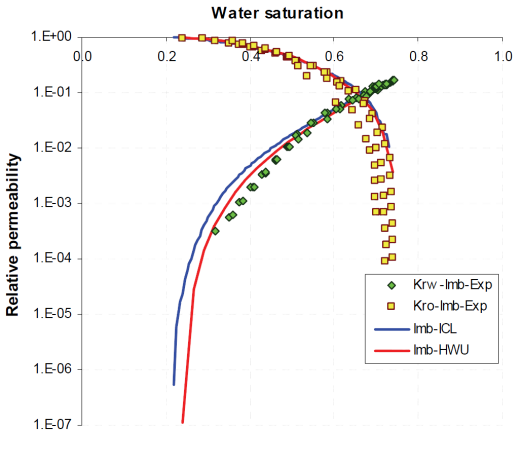

(d) Two-phase relative permeabilities during Imbibition on semi-log scale

Figure 5.1: Comparison of the relative permeabilities predictions by the network model (Ryazanov et al., 2010) with the experimental data (Oak, 1990) for the two-phase flow experiments during primary drainage and imbibition. ICL denotes the prediction by Valvatne and Blunt (2004) at Imperial College London and HWU denotes the prediction by Ryazanov et al. (2010) at Heriot-Watt University.

derpredicted residual oil saturation (S_{or}). On the contrary, Ryazanov et al. (2010) managed to predict S_{or} more accurately. This was attributed to accurate modelling of oil layers using the thermodynamic criterion. However, the Ryazanov et al. (2010) model underpredicted the water relative permeability.

A better prediction was obtained (Fig. 5.3) by making the system slightly less oil-wet during water flood as shown in Table 5.1 (case 2). This showed that the accuracy of the relative permeabilities predictions strongly depends on the wettability distribution, which could be obtained by matching other data (e.g. waterflood capillary pressures). However, in both cases the improved modelling of oil layers lead to a significantly more accurate prediction of the water flood residual oil saturation.

Table 5.1: Input parameters used for prediction of oil- wet experiments (Ryazanov et al., 2010)

PARAMETERS	CASE 1	CASE 2
Contact angles for Drainage (θ^{dr}_{ow}), degree	20-60	0
Contact angles for Imbibition (θ^{a}_{ow}), degree	90-173	96-158
Connate water saturation (S_{wc})	0.0	0.0
Initial water saturation (S_{wi})	0.03	0.02
Water viscosity, $10^{-3}Pa/s$	1.0	1.0
Oil viscosity, cP	0.29	0.29
Interfacial tension (σ_{ow}), $10^{-3}N/m$	51.8	51.8

5.2.3 *Mixed-wet system*

To validate the model for mixed-wet system, Ryazanov et al. (2010) used the experimental data of (Jadhunandan and Morrow, 1995) for slow-rate waterfloods in Berea sandstone core samples. The core samples were initially flooded with oil until prescribed initial water saturations S_{wi}. Then, the systems were aged and up to 20 pore volumes of water were injected. The oil recoveries were measured and the Amott-Harvey wettability index was calculated from the experimental Pc data using the modified Amott approach (Boneau and Clampitt, 1977).

Ryazanov et al. (2010) used the same network (Network A, described in section 3.2) and input data as Valvatne and Blunt (2004). However, Ryazanov et al. (2010) did not include pore bodies and, more importantly, they used the ther-

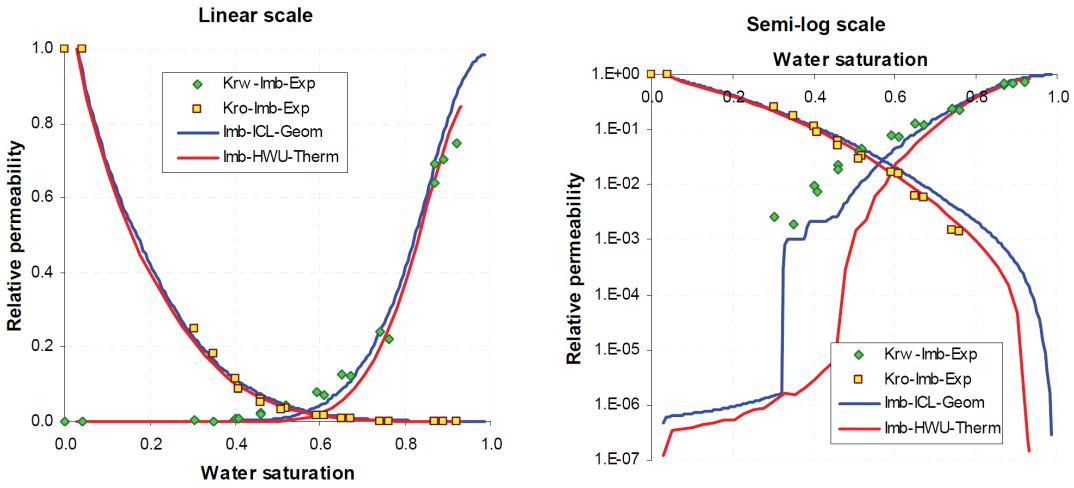

(a) Two-phase relative permeabilities during Imbibition

(b) Two-phase relative permeabilities during Imbibition on simi-log scale

Figure 5.2: Comparison of the water flood relative permeability predictions of the network model (Ryazanov et al., 2010), using parameters of case 2 in Table 5.1, with the experimental data (Valvatne and Blunt, 2004) for the oil-wet system. ICL denotes the prediction by Valvatne and Blunt (2004) at Imperial College London and HWU denotes the prediction by Ryazanov et al. (2010) at Heriot-Watt University.

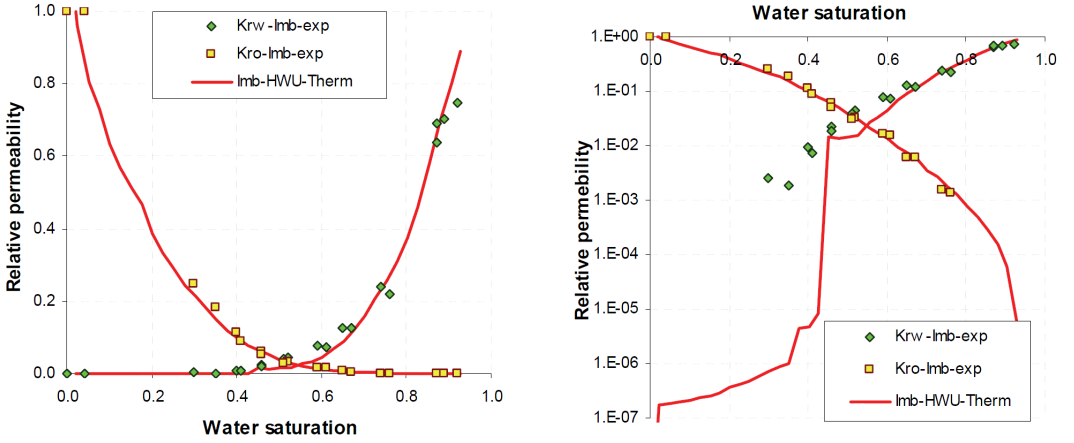

(a) Two-phase relative permeabilities during Imbibition

(b) Two-phase relative permeabilities during Imbibition on simi-log scale

Figure 5.3: Comparison of the water flood relative permeabilities predictions by the network model (Ryazanov et al., 2010), using parameters of case 2 in Table 5.1, with the experimental data (Valvatne and Blunt, 2004) for the oil-wet system. HWU denotes the prediction by Ryazanov et al. (2010) at Heriot-Watt University.

modynamic criterion for oil layer existence instead. Initially, the network was assumed water-saturated with contact angles of 0^0. Then, the network was flooded with oil until the predefined (experimental) initial water saturation S_{wi}. The network was aged and the contact angles were altered to reflect a mixed-wet large

(MWL) distribution (largest pores are oil-wet). The advancing contact angles for the water-wet faction of the oil-filled pores were uniformly distributed between 56^o and 76^o and for the oil-wet fraction the contact angles were distributed between 117^o and a maximum value $\theta_a^{ow,max}$ that was adjusted to match the Amott-Harvey wettability indices. $\theta_a^{ow,max}$ ranged between 167^o and 178^o. The waterflooding was simulated in the network and the corresponding k_r and S_{or} were calculated.

The remaining oil saturation and corresponding oil recoveries were estimated, after breakthrough (BT), after 3 and after 20 pore volumes of water injected, by using the network waterflooding relative permeability in the Buckly-Leverett analysis (Dullien, 1992). Fig. 5.4 shows the remaining oil saturations and oil recoveries as a function of the Amott-Harvey wettability index after different pore volumes injected, obtained from the experiments and from the network simulations (using Buckly-Leverett analysis). In general, good quantitative agreement between simulations and experiments was achieved.

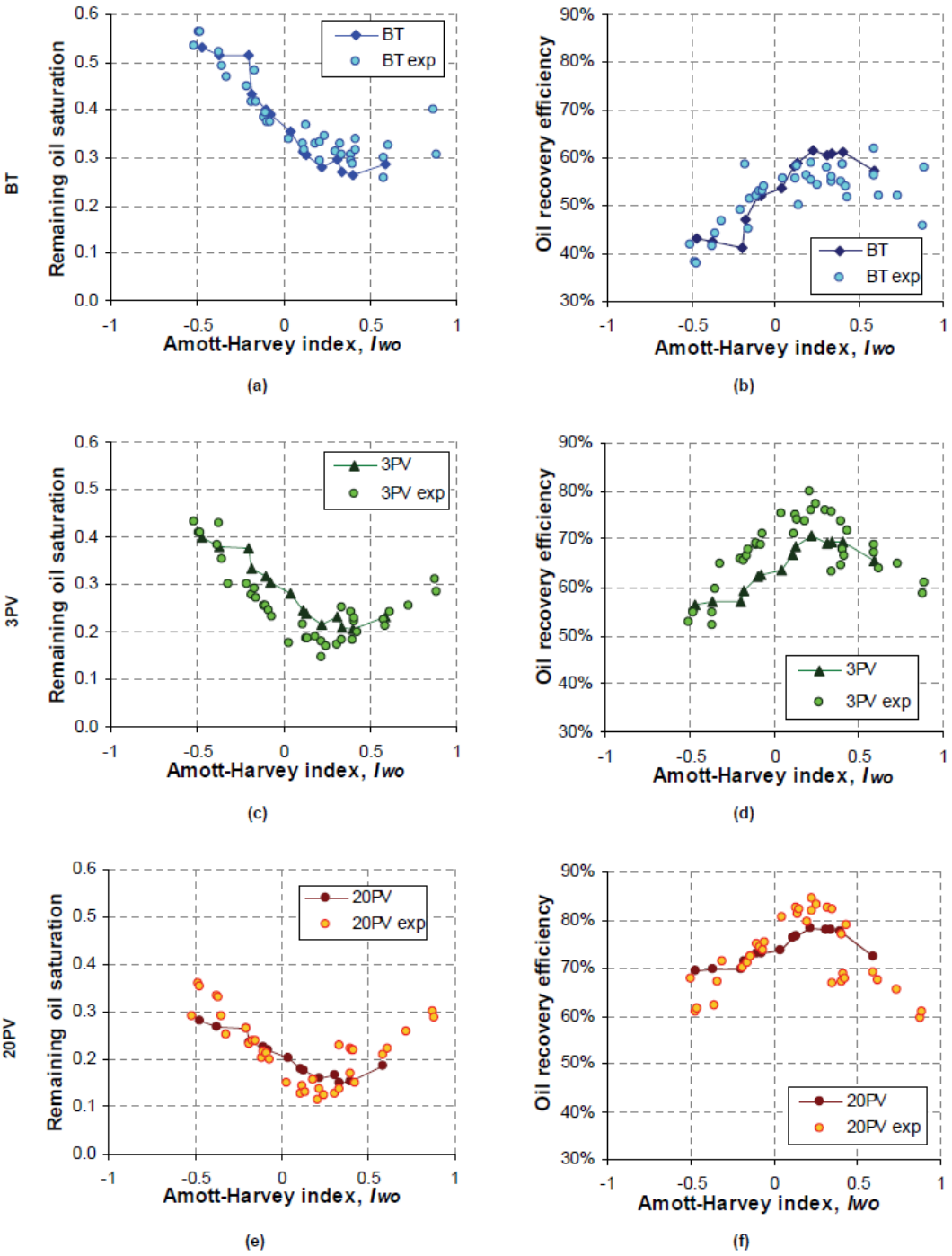

Figure 5.4: Calculated (Ryazanov et al., 2010) and experimental (Jadhunandan and Morrow, 1995) remaining oil saturations (a,c,e) and oil recovery efficiencies (b,d,f) vs. Amott-Harvey wettability index I_{wo}.

5.3 THREE-PHASE VALIDATION OF THE MODEL

5.3.1 *Water-wet system*

We used the two- and three-phase experimental data obtained by Oak (1990) to validate the current three-phase network model for water-wet systems. We consider the relative permeability data obtained from three water-wet Berea core samples (Samples 6, 13 and 14, which have absolute permeabilities of 200, 1000, and 800 mD, respectively). The porosities of the samples were not reported. The fluid systems that were used in Oak's experiments for the three samples are given in Table 5.2.

Oak did not report any measurement of interfacial tensions. However, Blunt (2000) and Lerdahl et al. (2000) suggested that the fluid system used by Oak (1990) was a spreading system because of low oil saturations that were reached in the experiments and the quadratic behaviour of the oil relative permeability at these low saturations. Piri and Blunt (2005b) used the interfacial tensions for a spreading hexane-water-air system to validate their model against Oak's experiments. We employ the same values that were used by previous authors: σ_{ow} =48mN/m, σ_{ow} =19mN/m and σ_{gw} =67mN/m. Oak did not report values for the contact angles. Therefore, these values must be estimated. Oak found that the two-phase relative permeability data of samples 13 and 14 were very similar. However, these were different from the relative permeabilities for the less permeable sample 6.

The network (Network A, described in section 3.2) used here was extracted from a process based reconstruction of Berea sandstone (Øren and Bakke, 2003), preserving both topology and pore shapes of the rock. We also compared the permeability of the network with the permeabilities of the core samples. The network has a permeability of 2673 mD, which is 13, 2.5 and 3 times higher than the permeability of samples 6, 13, and 14 respectively. Therefore, we used the relative permeabilities data of the more permeable samples 13 and 14 to validate our model.

Table 5.2: Fluid systems reported by Oak (1990)

SAMPLES	OIL	WATER	GAS
Sample 6	deodorized mineral spirit+5% iodobenzene; viscosity: 1.77 cp.	55,000 ppm brine+10% CsCl; viscosity: 1.06 cp	nitrogen at 800 psig; viscosity: 0.0187 cp
Sample 13 and 14	Dodecane+10% iodooctane; viscosity: 1.39 cp.	55,000 ppm brine+10% CsCl; viscosity: 1.05 cp	nitrogen at 800 psig; viscosity: 0.0187 cp.

5.3.1.1 *Revisiting two-phase validation*

We focused on choosing the contact angles that give a good match for the three-phase model rather than using the same contact angles which had been used by Ryazanov et al. (2010) for two-phase validation (section 5.2). For primary drainage, we assumed that the system is strongly water-wet; hence the oil-water contact angle is 0^o. We did not tune any other parameters of the network. The clay content was given in the input data files of the network (see section 3.5) and we did not change it; this clay content then dictates the initial water saturation for the network. For the water flood, we imposed a uniform distribution (uncorrelated to spatial location and pore size) of the oil-water contact angles with a minimum of 20^o and a maximum of 72^o, implying a weakly water-wet system. Fig. 5.5a and Fig. 5.5b show the relative permeabilities calculated by the model, as well as the experimental data for primary drainage and imbibition, respectively. The calculated curves are in good agreement with the experimental data.

5.3.1.2 *Gas Injection*

For the "prediction" of the three-phase relative permeabilities, we used the same oil-water contact angles as used for the water flood. We calculated the contacts angles for gas-oil (0^o) and gas-water ($16.9^o - 59.7^o$) according to the linear relationships; Eqs. 2.7a and 2.7b.

A true comparison of the three-phase relative permeabilities for a given saturation path obtained from the experimental data would require the network model to produce the same saturation path. Since we could not force our simulations, which were obtained from gas injection, to follow the experimentally derived sat-

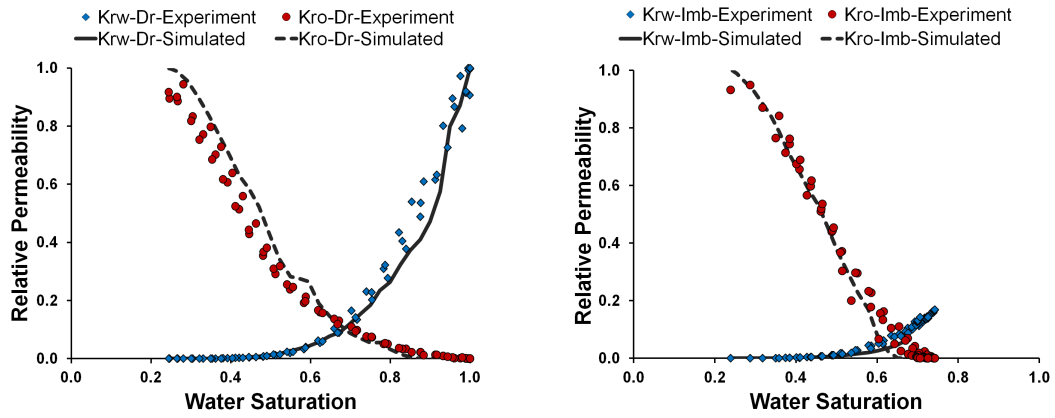

(a) Two-phase relative permeabilities during drainage

(b) Two-phase relative permeabilities during imbibition

Figure 5.5: Comparison of the relative permeabilities predictions by the network model with the experimental data (Oak, 1990) for the two-phase flow experiments during drainage and imbibition floods for water-wet system.

uration paths exactly, which were obtained from so-called steady state injection of multiple phases, we produced a set of saturation paths (Fig. 5.6a) that cross in the same region of the saturation space as the experimental paths. Consequently, we compared the three-phase relative permeabilities derived from the network model with a cloud of the experimental data for numerical and experimental saturation paths that cover the same region (Svirsky et al., 2007).

Fig. 5.6b shows the three-phase oil relative permeability curve predicted by the network model, compared to the experimental data (Oak, 1990). The predicted oil relative permeabilities are scattered in a similar manner as the measured oil relative permeability. The experimental data are scattered because in a water-wet system, where oil is the intermediate-wetting phase, the oil relative permeability is expected to be a function of saturation history and initial oil saturation (Oak, 1990; Hui and Blunt, 2000b; Piri and Blunt, 2005b).

Fig. 5.6c shows the three-phase water relative permeability curve predicted by the network model, compared to the experimental data of Oak (1990). The predicted water relative permeability matches the measured values perfectly. The water relative permeability behaves as expected for a water-wet system. In a water-wet system, where water is the most wetting phase, the water relative permeability is a function of its own saturation.

Fig. 5.6d shows the three-phase gas relative permeability predicted by the network model, compared to the experimental data (Oak, 1990). In a water-wet

system, where gas is the least wetting phase, the gas relative permeability is a function of its own saturation. However, because of experimental difficulties (Oak, 1990), the measured gas relative permeability values are scattered at low gas saturations. The predicted and measured data become less scattered at high gas saturation. The predictions are in good agreement with the measured values. These predictions are similar to those obtained by Piri and Blunt (2005b). We could not match the non-zero gas relative permeability at very low gas saturations due to the finite size of the network used in this work.

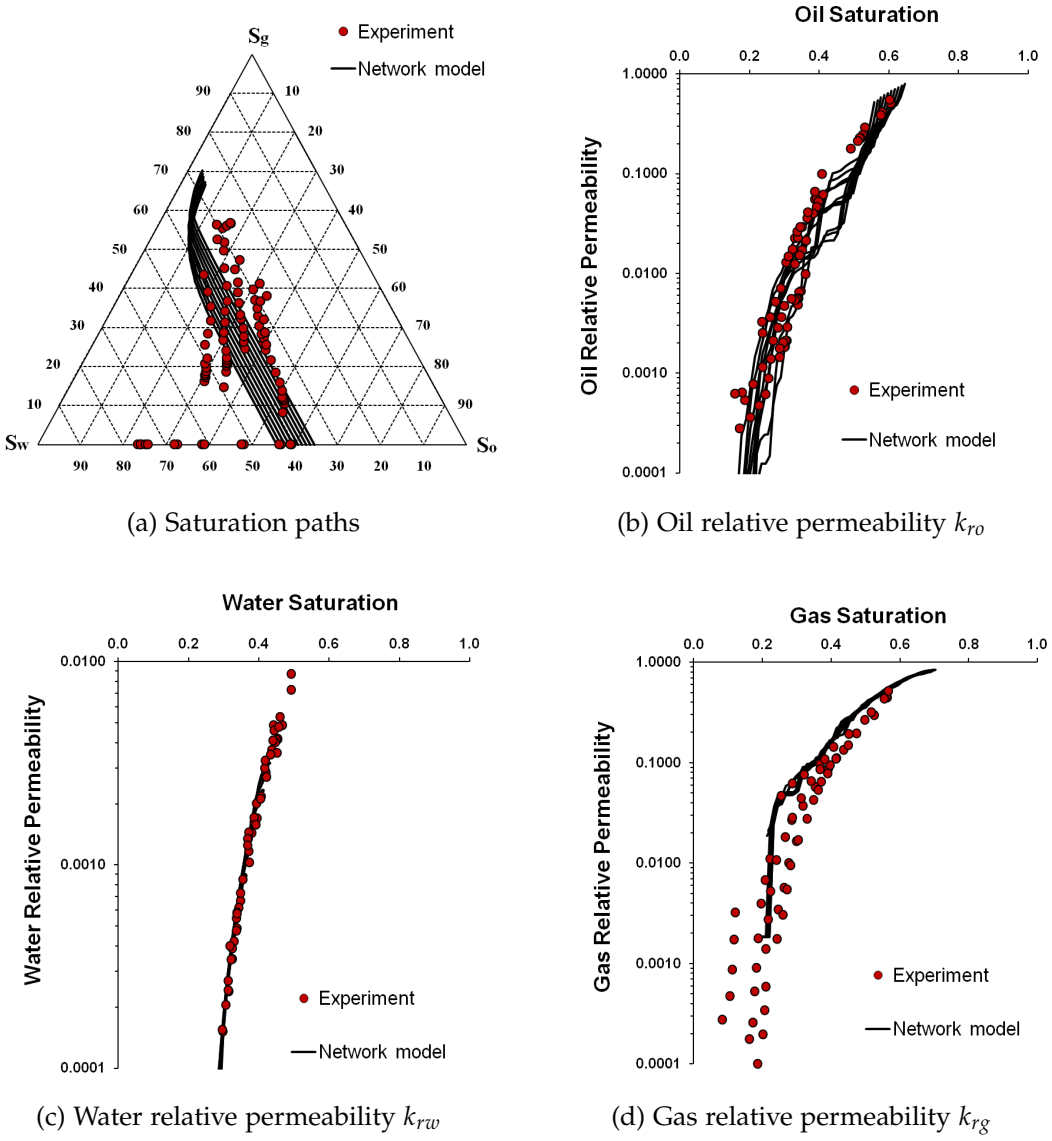

(a) Saturation paths

(b) Oil relative permeability k_{ro}

(c) Water relative permeability k_{rw}

(d) Gas relative permeability k_{rg}

Figure 5.6: Saturation paths and the relative permeabilities predictions by the network model compared with the experimental data (Oak, 1990) for the three-phase flow experiments on samples 13 and 14 during tertiary gas injection.

5.3.1.3 *Comparison with predictions by previous three-phase network model*

As discussed in section 1.4, different studies have concluded that three-phase properties (relative permeabilities) strongly depend on the phase saturations and the saturation path history. Therefore, to predict the experimental results it would be necessary to reproduce the same saturation paths. Piri and Blunt (2005a,b) used an algorithm to track the saturation paths of the experiment, by injecting slugs of oil, water and gas into their pore-network model.

To demonstrate the improvements of our model in predicting the three phase microscopic properties, we consider one of the experiments that was matched by Piri and Blunt (2005b). However, we run the simulation without forcing the saturation path to go in a prescribed direction or to terminate at a specific gas saturation. In this case, we assume that the network, initially water-saturated, has an oil-water contact angle of 0^o, implying strongly water-wet system. Then, the network is flooded with oil until a predefined water saturation, taken from the experiment, (S_{wi} = 0.252). After that, the oil-water contact angles of the oil-filled pores are altered. Since we are preforming a rigorous comparison rather than a comparison of clouds of data, we use contact angles, distributed between 56^o and 76^o, which are based on the model validation for two-phase flow, carried by Ryazanov et al. (2010), as discussed in section 5.2. The corresponding three-phase contact angles are simply calculated using the linear relationships (Eqs. 2.7). We used the same interfacial tensions that were used by Piri and Blunt (2005a,b), shown in Table 2.1. Finally, gas was injected into the network and the simulation stopped at residual oil saturation. Fig. 5.7a, shows the measured and predicted saturation paths. Both network models reproduced the same saturation path. The corresponding oil relative permeabilities are shown in Fig. 5.7b. Both models overpredicted the oil relative permeabilities. However, the prediction of our model is much closer to the measured values. The better prediction is attributed to the new thermodynamic criterion which was used to model the oil layer formation and collapse.

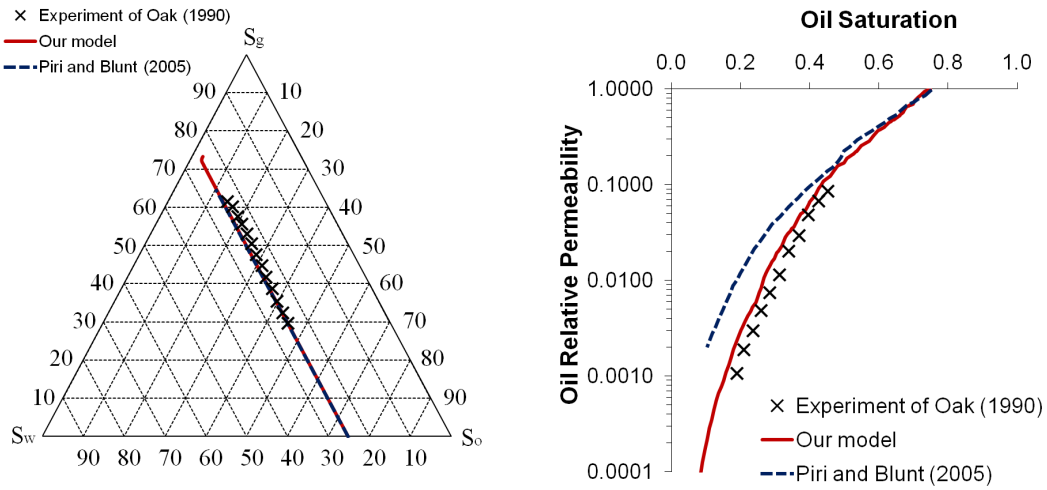

(a) Saturation paths

(b) k_{ro}

Figure 5.7: Comparison of measured and predicted three-phase properties for experiment 10, sample 14, of experiments of Oak (1990).

5.3.2 *Oil-wet System*

5.3.2.1 *Micromodel experiments*

To validate our model for oil-wet systems, we used experimental data from a WAG micromodel for oil-wet system (Sohrabi et al., 2001, 2004). The WAG experiments were conducted using high-pressure acid-etched glass micromodels for different wettability conditions (water-wet, oil-wet and mixed-wet). Table 5.3 shows the main parameters of the micromodel and fluid properties. Further experimental details are given by Sohrabi et al. (2001, 2004). The experiments revealed some important phenomena in three-phase flow physics, for example multi-displacement processes and thickening of oil films, which have a major impact on the flow behaviour of three phases and subsequent oil recovery. In an oil-wet micromodel, water is the non-wetting phase relative to oil and thus had to be forced into the model. Contrary to a water-wet system, in which water displaces oil through corner filament flow (water imbibition), in the oil-wet system water displaces oil in a piston-like manner. These two different displacement mechanisms lead to different patterns of the residual oil. After water injection, the injected gas was observed to invade the oil-filled pores rather than the water-filled pores.

Table 5.3: Main Micromodel Parameters

MODEL PARAMETERS	VALUES
Nodes	120x20
Coordination number	2.67
Pore cross-section Shape	Rectangular
Pore width[1]	90 to 280 μm
Pore depth	50 μm
Pore length	350 μm
ρ_w, kg/m^3	1000
ρ_o, kg/m^3	706
ρ_g, kg/m^3	21
σ_{ow}, mN/m	41
σ_{go}, mN/m	15
σ_{gw}, mN/m	65
Injection rate, cm^3/h	0.01

[1] Distributed randomly.

Initially, the micromodel was fully filled with oil and there was no water present in the model. Then, water was injected into the model to mimic the initial waterflood. After that, gas was injected into the model followed by another water injection (WAG cycle). In total, five WAG cycles were performed. All floods were stopped at the breakthrough of the invading phase. No contact angles were reported but the observation of the experiments suggested that gas was the intermediate-wetting phase, water was the non-wetting phase and oil was the wetting phase in the system.

5.3.2.2 *Comparison of numerical results and experimental observations for the oil-wet micromodel*

van Dijke et al. (2006) used the above micromodel experiments to validate an older three-phase pore-network model. They generated a single 2D network and simulated half of the micromodel. As there was uncertainty related to the degree of wettability, which was a key input parameter for their simulations, they compared the direct observation at the pore-scale in the micromodel with the theory on wetting order and the presence or absence of wetting films. They ran a limited number of simulations to obtain realistic input values for these param-

eters (the wetting order of the phases and the presence or absence of oil wetting films) and were able to achieve a satisfactory distribution of fluid phases and oil recoveries when compared to experimental data. For this they had to allow oil wetting films around water to form only in a fraction of the pores. This fraction was an additional tuning parameter.

In this work, we used the same interfacial tensions as used by van Dijke et al. (2006). However, in contrast to the latter, the only parameter we needed to tune to match the experimental data were the contact angles. Since the exact pore-network geometry of the micromodel could not be recreated with our pore-network model, we generated ten random 2D networks (N1-N10) with properties that were statistically similar to those of the full micromodel (Table 5.3). The generated 2D networks consist of pores bodies (nodes) and pores throats (bonds). Each pore had a regular square shape.

We used the interfacial tensions and the contact angles given in Table 5.4 to simulate the oil-wet micromodel experiments. Note that the interfacial tensions indicate that oil is spreading and also note that the contact angles satisfy Eqs. 2.6 and 2.7. The chosen range of contact angles implies that oil wetting films can only be present in a fraction of all water filled pores and should be present in all gas filled pores. However, this is not always the case, especially for higher order WAG cycles during which oil has been removed completely by water from some pores. In these pores, we do not allow oil wetting films to form when gas is introduced to them. This has a great impact on the phase connectivity and, therefore, manifests the importance of the multiple displacements during higher order WAG cycles.

All networks have the same wettability state and were subjected to the same flooding sequence. We averaged the residual oil saturation of all networks after each flood as shown in Fig. 5.8 and compared the averages with the corresponding values from the oil-wet micromodel (Fig. 5.9). Overall we achieved a good match between the experiments and the network model simulations in terms of oil recovery. In the experiment the oil saturation decreases from $S_{o,initial} \approx 48\%$ to $S_{o,final} \approx 24\%$ while in the simulation the average oil saturation decreases from $S_{o,initial} \approx 52\%$ to $S_{o,final} \approx 22\%$. Fig. 5.10 show how our prediction of the oil recovery compared with the prediction of van Dijke et al. (2006). In general,

we predicted the oil recovery more accurately than the prediction of van Dijke et al. (2006).

Table 5.4: Wettability Parameters for the comparison with the micromodel experiments.

WETTABILITY STATE	VALUES
θ_{ow}, degree	120.0-180.0
θ_{go}, degree	0.0
θ_{gw}, degree	95.6-117.7
σ_{ow}, mN/m	41
σ_{go}, mN/m	15
σ_{gw}, mN/m	56
Wetting order[1]	oil-gas-water

[1] From most to least wetting phase.

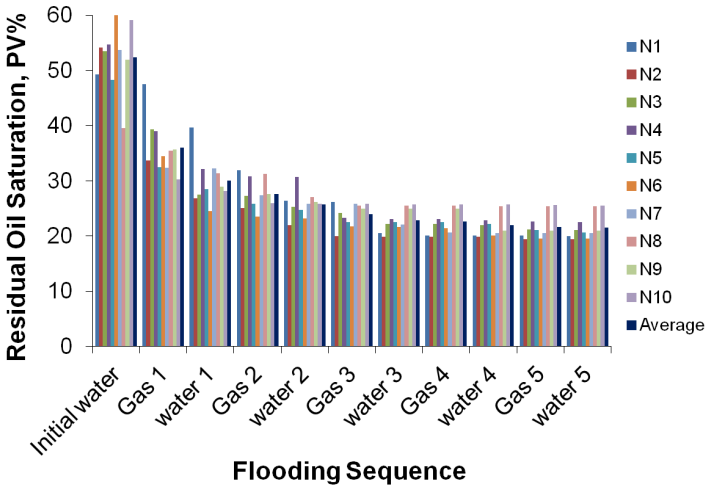

Figure 5.8: Simulated residual oil saturations in an oil-wet micromodel for ten randomly generated 2D networks. All networks have statistically similar geometries as the micromodel.

Fig. 5.11 shows the fluid distributions in the oil-wet micromodel after the initial water flood and subsequent WAG floods. Since we have used ten different, but statistically equivalent, micromodel geometries for our simulations and computed the average oil recovery after each flood, it is difficult to compare the fluid distribution of the micromodel experiment directly to the corresponding simulated distributions. For a qualitative visual comparison of simulated and experimental fluid distributions we have selected network N9, because its oil residual is very similar to the average residual oil saturation. Fig. 5.12 shows the sim-

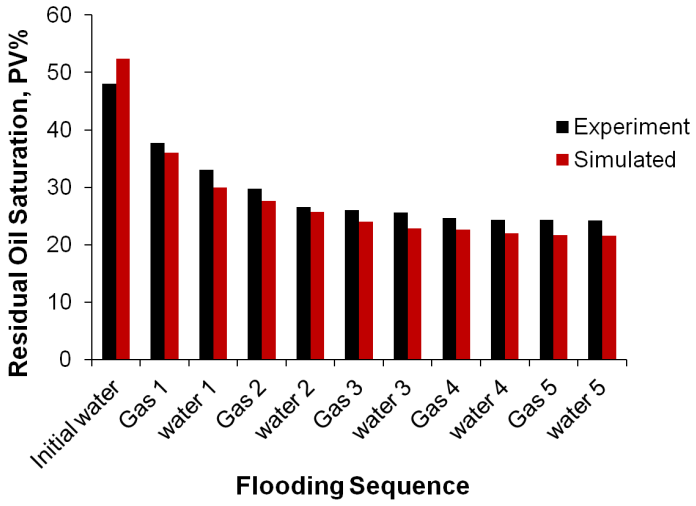

Figure 5.9: Simulated and experimental residual oil saturation for the oil-wet micro-model, computed after each individual WAG cycle. Note that the simulated residual oil saturations represent the averages for the ten networks.

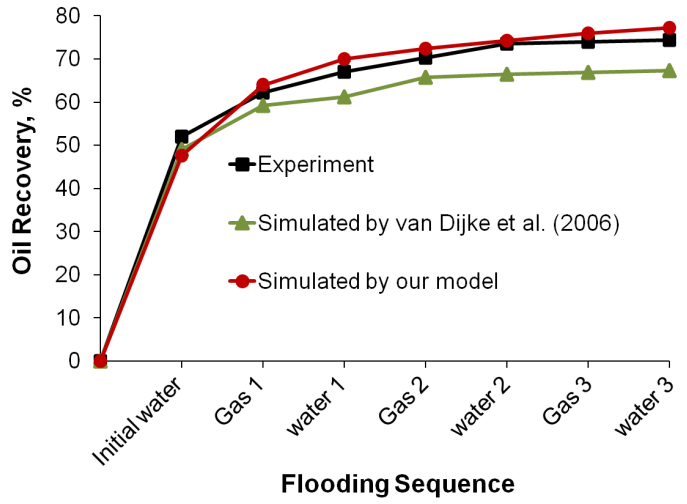

Figure 5.10: Comparison of oil recovery predicted by our model and previous model of van Dijke et al. (2006).

ulated fluid distribution in the oil-wet system after the initial water flood and subsequent WAG floods for network N9.

For the initial water flood, the simulated residual oil is slightly higher than the experimental value. However, the fluid distribution is very similar in the simulation and the experiment. During the first gas flood a significant amount of oil is produced, both in the simulation and in the experiment. Gas displaces both oil and water, which is a direct consequence of the wetting order of the system. The gas distribution pattern is very similar in the experiment and in the simulation. There are some parts of the model that have a dense cluster of gas and they are connected through fingers of gas. During the first water flood, water

clusters can be observed to reconnect and retain their initial distributions. The amount of the additional oil recovered by the simulation and the experiment is approximately the same for the subsequent floods. However, the additional amount of recovered oil decreases from one flood to the next until it becomes insignificant after the second WAG cycle.

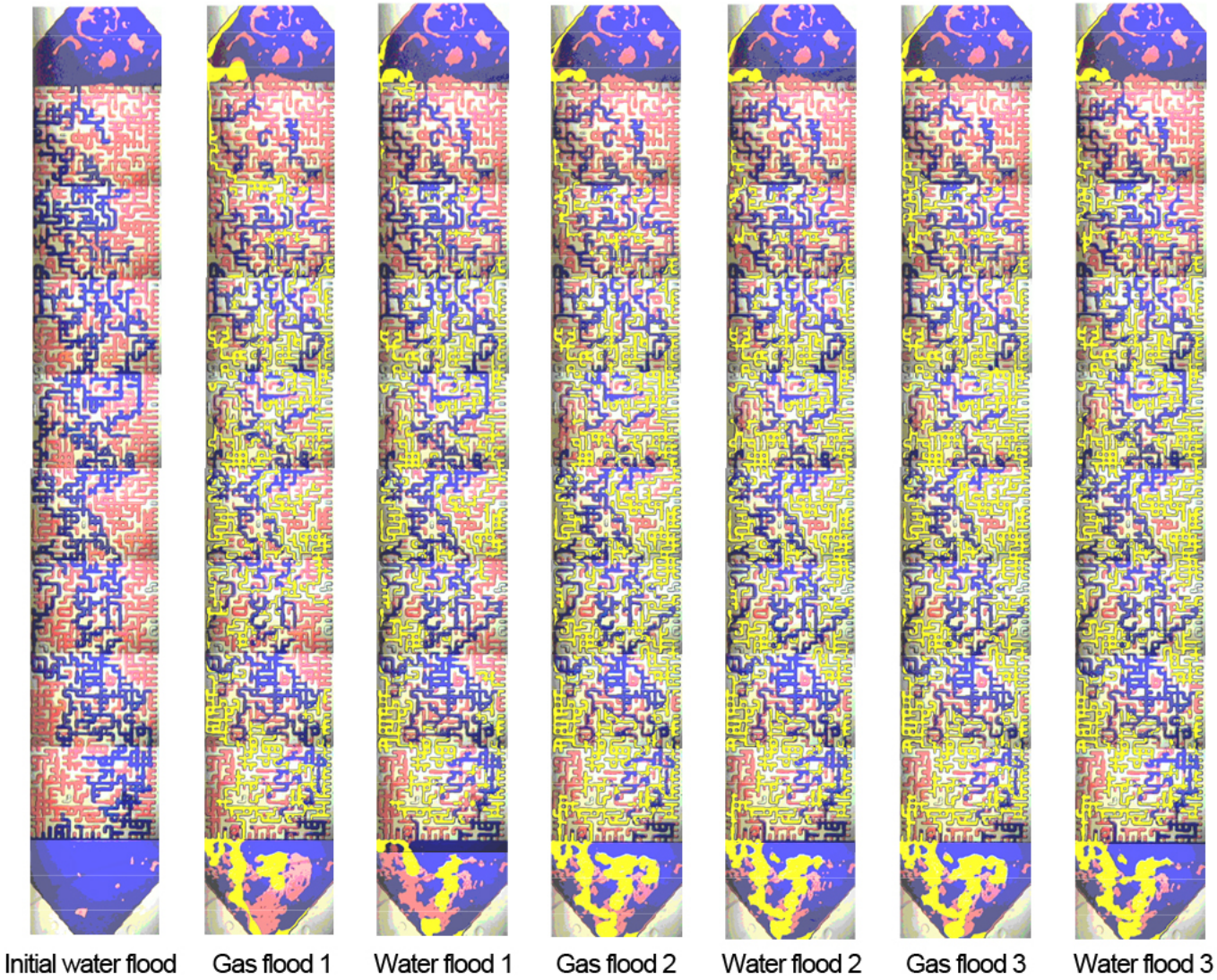

Figure 5.11: Experimentally observed fluid distribution during WAG injection in an oil-wet micromodel for the initial water flood and 3 WAG cycles (Sohrabi et al., 2004). Blue denotes water, red oil and yellow gas. Fluids are injected at the bottom (inlet) and recovered at the top (outlet) of the micromodel.

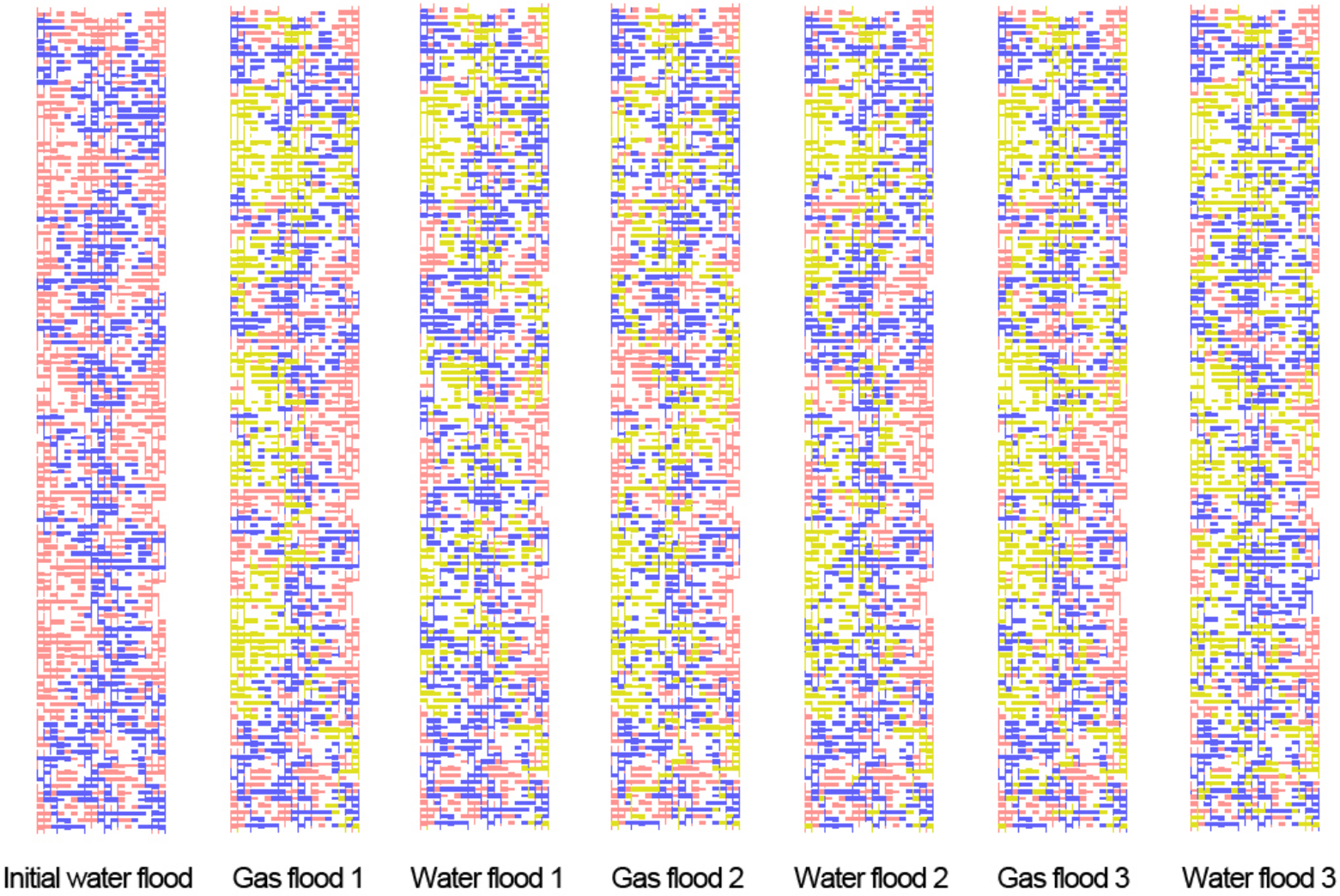

Figure 5.12: Simulated fluid distribution after the initial water flood and first three WAG cycles in an oil-wet network model that is statistically equivalent to the original micromodel. See Fig. 5.11 for comparison with the experimental data.

5.4 SUMMARY AND CLOSING REMARKS

In this chapter, we have presented the validation of our model against experimental data. To validate the model, two- and three-phase relative permeability experimental data of a Berea sandstone sample, reported by Oak (1990), were used. For two-phase flow, the predicted values of relative permeability of both oil and water are in good agreement with the experimental data. For the three-phase flow, the predicted three-phase water relative permeability curves are in perfect agreement with the measured data. The predicted three-phase gas relative permeability gives a good match with the experimental data. The predicted oil relative permeabilities are scattered in a similar manner as the measured oil relative permeability, which is caused, both experimentally and numerically, by the different saturation histories. Additionally, we demonstrated the impact of implementing the thermodynamic criteria for oil layer formation and collapse. This was done by comparing the predictions of our model and a previous model of Piri and Blunt (2005a,b) with the experimental data. Our model gave a more accurate prediction, which was attributed to the accurate modelling of oil layers.

For an oil-wet system, we simulated the micromodel experiments that were conducted by Sohrabi et al. (2000, 2001, 2004). The pore-network model produced very similar oil recovery profile to the experimental ones. These predictions were better than the prediction of a previous pore-network model developed by van Dijke et al. (2006). We performed a qualitative visual comparison of simulated and experimental fluid distributions. For the initial water flood, the fluid distribution is very similar in the simulation and the experiment. During the first gas flood, some parts of the model were observed to have dense clusters of gas which were connected through fingers of gas, both in the experiment and in the simulation. During the first water flood, water clusters reconnected and retained their initial distribution.

From these validation, we conclude that the model is able to capture the main detailed physics of three-phase flow at the pore-scale adequately and is ready to be put in use for simulation of different networks with arbitrary wettability.

6

PORE-SCALE SIMULATIONS

6.1 INTRODUCTION

In this chapter, we show the capability of our new model to compute the relative permeabilities for realistic 3D pore-networks, extracted from pore-space reconstruction methods and CT images, by carrying out a number of three-phase water-wet and oil-wet simulations. We use four different networks (Figs. 3.1–3.2): network A represents the pore-space structure for Berea sandstone rocks and the other three networks (B, C and D) represent carbonate rocks. Further detail of the networks can be found in chapter 3.

6.2 WETTING SYSTEMS AND FLOODING SEQUENCE

We considered three wetting systems for which the parameters are presented in Table 6.1, one is water-wet and the other two are weakly and strongly oil-wet, respectively. The three systems have same interfacial tensions (Table 2.1).For the water-wet simulation, we assumed that the network is fully filled with water as the initial state. Then, we flooded it with oil (primary drainage) until the irreducible water saturation, contained in the clay porosity (Valvatne and Blunt, 2004), was reached. After that, we simulated water invasion (imbibition) up to a predefined water saturation, S_{wi}. Finally, we injected gas into the network until the residual oil saturation was reached. We repeated the simulation for different S_{wi} to generate a data set that represents the full range of three-phase relative permeabilities in the three-phase saturation reasonably well.

For the two oil-wet systems, we assumed that the network is fully filled with oil at the connate water saturation as the initial state. Then, we flooded it with water up to a predefined water saturation, S_{wi}. Finally, we injected gas into the network until residual oil was reached. We repeated the simulation for different S_{wi} to generate the three-phase relative permeabilities.

Table 6.1: Properties of the wetting systems

CASES	1	2	3
Wettability state	strongly water-wet	weakly oil-wet	strongly oil-wet
θ_{ow}, degree	0.0	90.5-110	120-150
θ_{go}, degree	0.0	0.0	0.0
θ_{gw}, degree	0.0	73.9-87.8	94.2-109.6
Wetting order[1]	water-oil-gas	oil-water-gas	oil-gas-water

[1] From most to least wetting phase.

6.3 SIMULATION RESULTS AND DISCUSSION

Figs. 6.1-6.4 show the saturation paths resulting from gas injection at different S_{wi} with the corresponding three-phase relative permeabilities k_r for the four networks A, B, C and D (Figs. 3.1-3.2), respectively. The following emergent behaviours and resulting three-phase flow properties can be observed for the different networks and different wettability states:

6.3.1 *Saturation paths*

The carbonate networks exhibit some discontinuities in the saturation paths. This is caused by a small number of pores with large volume ("vugs"). Invasion of such pores causes an immediate large change in the phase saturation (Fig. 6.2). Furthermore, in the strongly oil-wet cases, the saturation paths show that gas displaces oil, except for high water saturations, because water is preventing gas from invading the oil-filled pores. However, oil can be mobilised by a double displacement g→w→o. Hence some of these oil-filled pores become accessible to gas near the end of the saturation path and, therefore, gas can now displace oil directly (g→o). In network C, significant water displacement occurs for the

weakly oil-wet system. In the weakly oil-wet system, gas is the least wetting phase and is therefore expected to displace mainly water. For network C, the water saturations that are reached after the water flood are larger than for the other networks. This results in continuity of the water phase for a significant range of saturations during gas injection.

6.3.2 *Residual oil*

The common feature for all four networks is that the residual oil saturation reaches very low values for strongly water- and oil-wet systems during the gas flood. In the water-wet system, oil is the intermediate wetting phase and can be present as a bulk phase, occupying the central part of the pores, or as layers sandwiched between water wetting films and gas bulk phase (Fig. 4.2V). This maintains hydraulic connectivity for the oil at very low oil saturation, providing pathways for the oil to escape to the outlet, which results in low residual oil saturations. In the oil-wet system, oil is the wetting phase and can be present as a bulk phase or as corner wetting films (e.g. Fig. 4.2M and Fig. 4.2E), which maintain connectivity of the oil phase. However, in the weakly oil-wet case, a smaller number of oil films formed around the water compared to the strongly oil-wet case (and therefore also around the gas phase in the subsequent gas flood). This results in a lower oil connectivity and hence higher residual oil saturations. For instance, carbonate network B has less than 1% residual oil for the strongly oil-wet system, while this can be as high as 32% for the weakly oil-wet system.

6.3.3 *Three-phase region*

The size of the three-phase region, i.e. the saturation values where all three phases are present, is determined by the connate water saturation and the minimum residual oil saturation during the water flood. In the strongly oil-wet case, a larger number of oil wetting films formed around water during the water flood compared to the weakly oil-wet case. Therefore, the oil phase is more connected in the strongly oil-wet case compared to the weakly oil-wet case, leading to lower

residual oil saturations during the water flood. Hence the saturation paths cover a larger region, causing a wider three-phase region for the strongly oil-wet system. The difference in three-phase regions between the water-wet and weakly oil-wet systems is large for networks C and D whereas for networks A and B it is much smaller. This is related to the residual oil saturations during the water flood, which is in turn related to the network connectivity. Indeed, based on their respective coordination numbers the network connectivities decrease from network A to network D (Table 3.2), while the water flood residual oil saturations show the opposite trend in the water-wet systems. Surprisingly, the water flood residual oil saturations in weakly oil-wet systems are not simply correlated to the network connectivity.

6.3.4 *Oil relative permeability*

The oil relative permeability in the strongly oil-wet case is enhanced by the presence of additional films around water compared to the weakly oil-wet case, in which the oil phase is less well-connected, resulting in a lower oil relative permeability. For example for the Berea network at S_o=0.59, S_w=0.3 and S_g = 0.11, the oil relative permeability k_{ro} is 0.146 for the weakly oil-wet case and k_{ro} is 0.242 for the strongly oil-wet case.

6.3.5 *Gas relative permeability*

In the homogeneous Berea network (Network A), the gas relative permeability is comparable for both oil-wet cases, strongly and weakly oil-wet. However, for the carbonate networks the gas relative permeability is generally higher for the weakly oil-wet system compared to the strongly oil-wet system at identical saturation combinations. A noteworthy feature of the gas relative permeability behaviour for the weakly oil-wet systems is that the saturation paths intersect; hence different relative permeabilities can occur for the same saturation combination. This feature can be observed particularly well in the carbonate sample from network B (Fig. 6.2.) The multiple values of the gas relative permeability are caused by the dependence of the relative permeabilities on the flow history,

i.e. the saturation path. Note that this is not only a numerical feature but occurs in laboratory experiments as well.

6.3.6 *Water Relative Permeability*

In the water-wet systems, water is connected by water wetting films which yield small non-zero values for the water relative permeability for a wide range of saturation paths. On the contrary, in the oil-wet systems the water relative permeability quickly drops to zero for relatively large water saturations, because of the poor phase connectivity due to the absence of water films.

6.3.7 *Oil recovery by water and gas flood*

In the water-wet system, gas injection leads to a significant improvement in oil recovery. For example, waterflood in the Berea Sandstone (Network A) leads to 40% residual oil saturation but injection of gas can lead to a residual oil saturation of as low as 1%. The reason for this dramatic improvement in recovery is that during the water flood snap-off displacements disconnect oil clusters and hence trap them. The resulting disconnected oil clusters cause the high residual oil saturation. In contrast, during the gas flood, oil is displaced mainly by piston-like displacements. This creates oil layers which maintain oil connectivity and thus cause the lower residual oil saturation. However, in the oil-wet system there is no significant improvement in oil recovery due to gas injection because snap-off during water injection does not occur. Hence oil can be drained by either water or gas injection through the oil films.

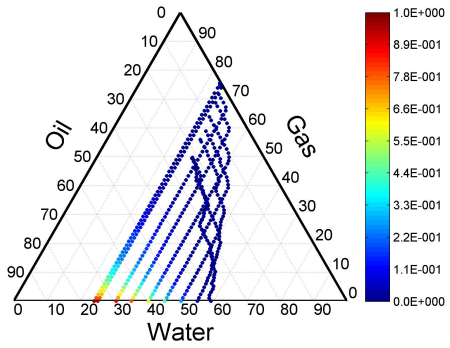

(a) k_{ro}

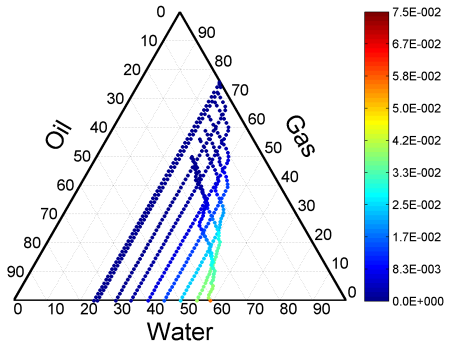

(b) k_{rw}

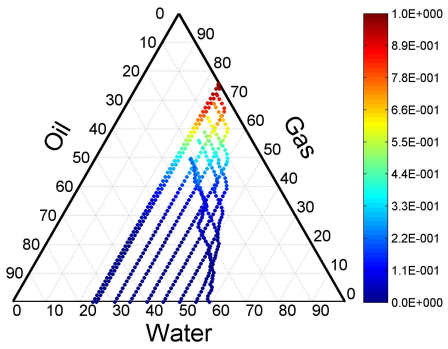

(c) k_{rg}

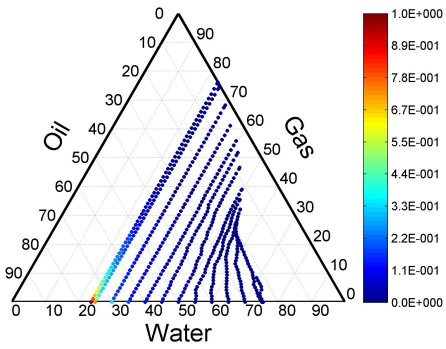

(d) k_{ro}

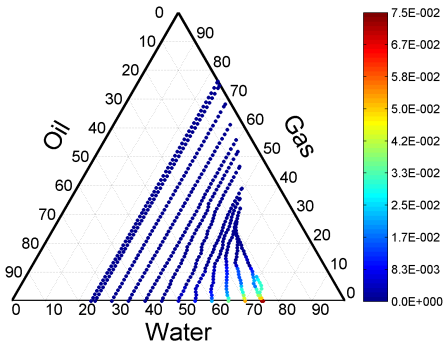

(e) k_{rw}

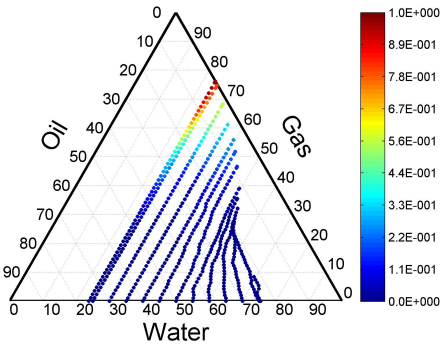

(f) k_{rg}

Figure 6.1: *Continued on next page . . .*

. . . continued from previous page

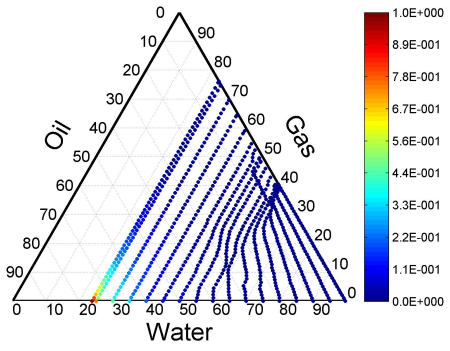

(g) k_{ro}

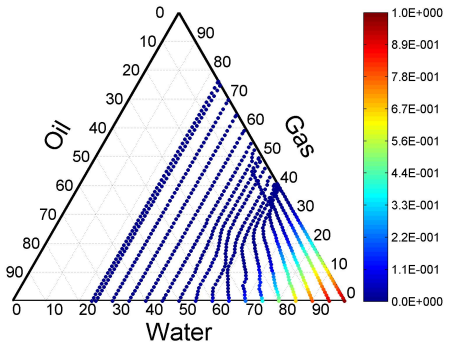

(h) k_{rw}

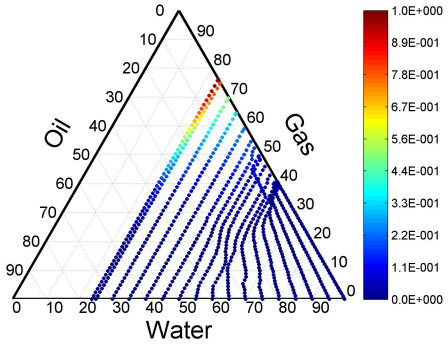

(i) k_{rg}

Figure 6.1: Simulated relative permeabilities of network A: (a)-(c) for strongly water-wet (case 1), (d)-(f) for weakly oil-wet (case 2) and (g)-(i) for strongly oil-wet (case 3) conditions. Note the difference in the scale of the individual relative permeabilities.

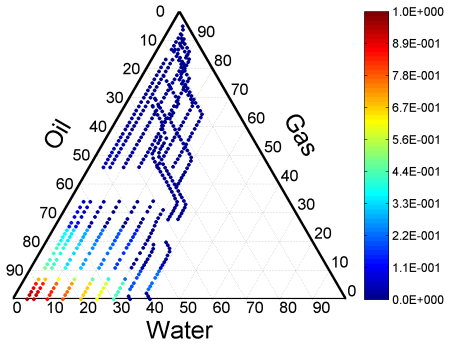

(a) k_{ro}

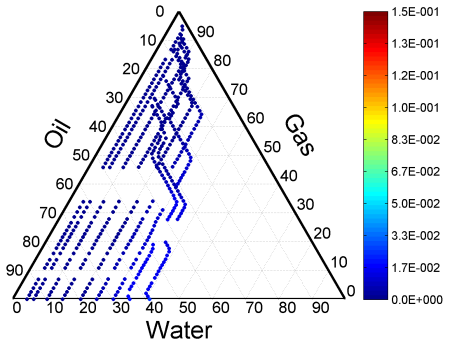

(b) k_{rw}

Figure 6.2: *Continued on next page . . .*

. . . continued from previous page

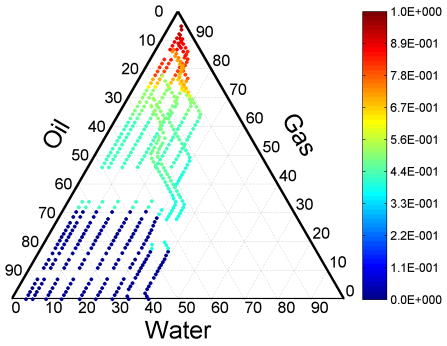

(c) k_{rg}

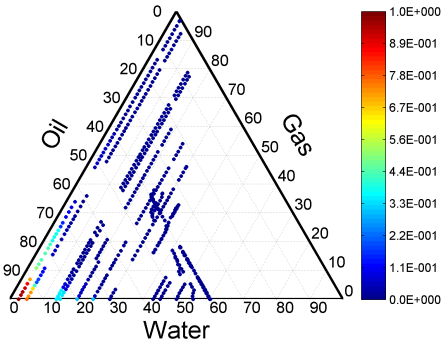

(d) k_{ro}

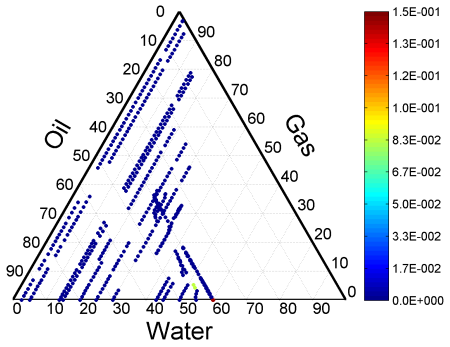

(e) k_{rw}

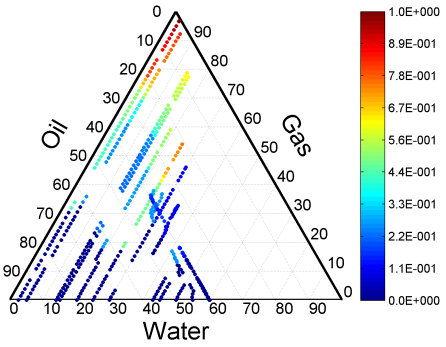

(f) k_{rg}

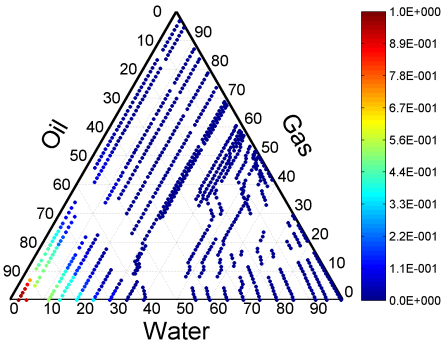

(g) k_{ro}

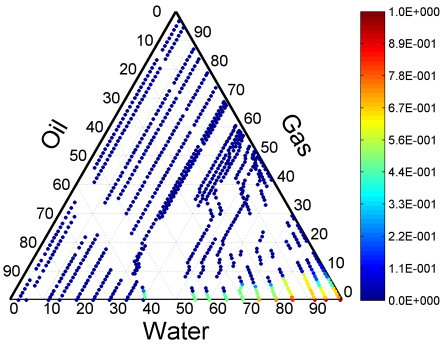

(h) k_{rw}

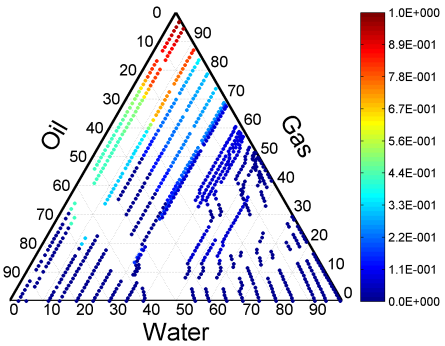

(i) k_{rg}

Figure 6.2: Simulated relative permeabilities of network B: (a)-(c) for strongly water-wet (case 1), (d)-(f) for weakly oil-wet (case 2) and (g)-(i) for strongly oil-wet (case 3) conditions. Note the difference in the scale of the individual relative permeabilities.

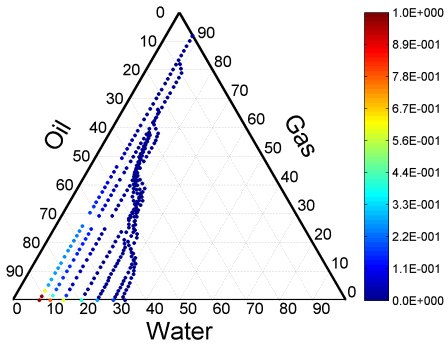

(a) k_{ro}

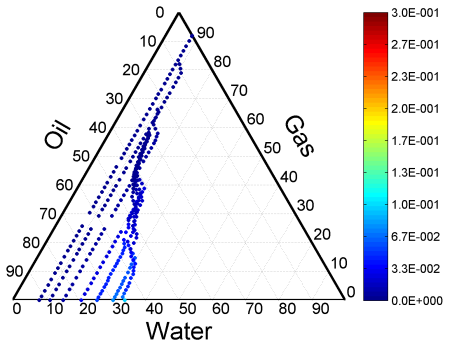

(b) k_{rw}

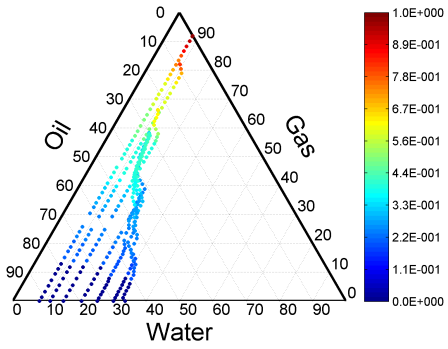

(c) k_{rg}

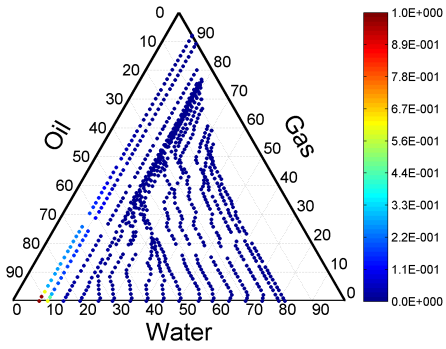

(d) k_{ro}

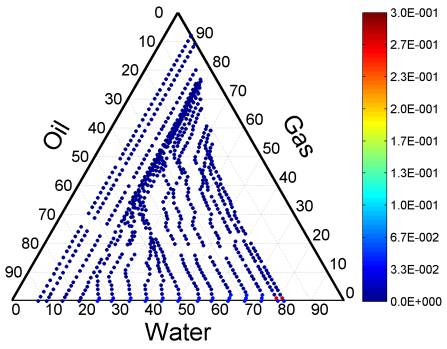

(e) k_{rw}

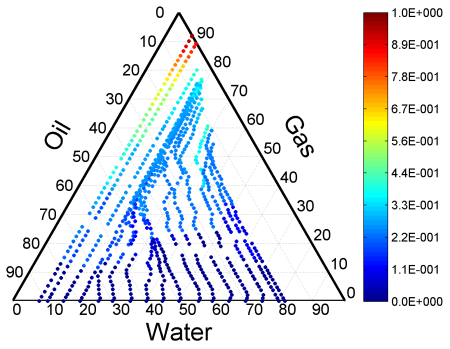

(f) k_{rg}

Figure 6.3: *Continued on next page . . .*

. . . continued from previous page

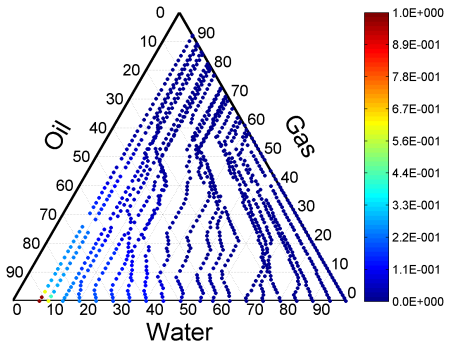

(g) k_{ro}

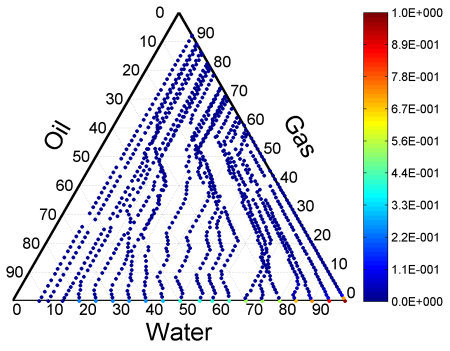

(h) k_{rw}

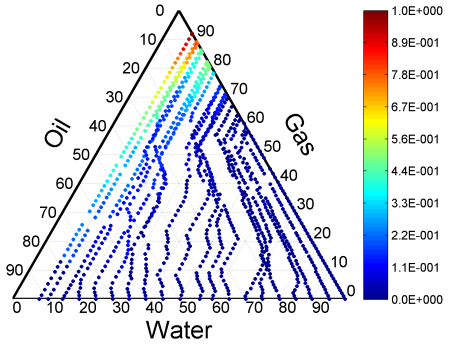

(i) k_{rg}

Figure 6.3: Simulated relative permeabilities of network C: (a)-(c) for strongly water-wet (case 1), (d)-(f) for weakly oil-wet (case 2) and (g)-(i) for strongly oil-wet (case 3) conditions. Note the difference in the scale of the individual relative permeabilities.

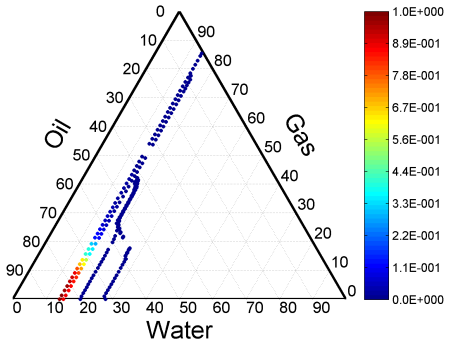

(a) k_{ro}

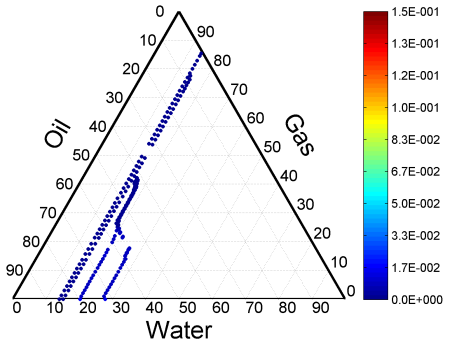

(b) k_{rw}

Figure 6.4: *Continued on next page . . .*

. . . continued from previous page

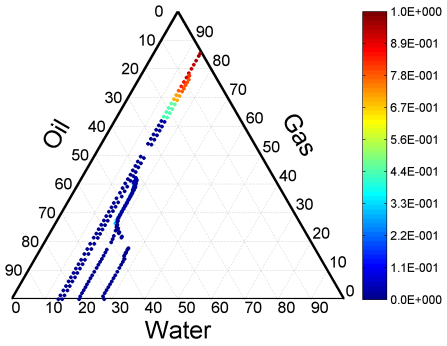

(c) k_{rg}

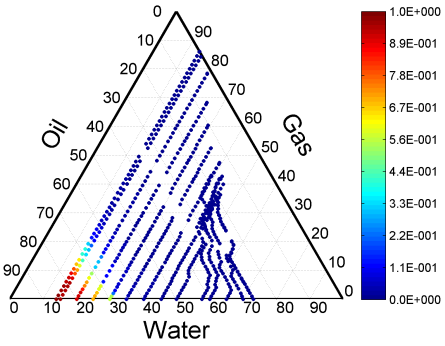

(d) k_{ro}

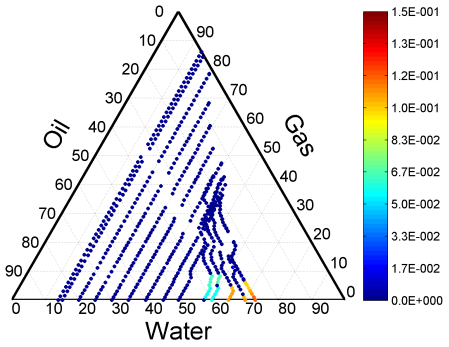

(e) k_{rw}

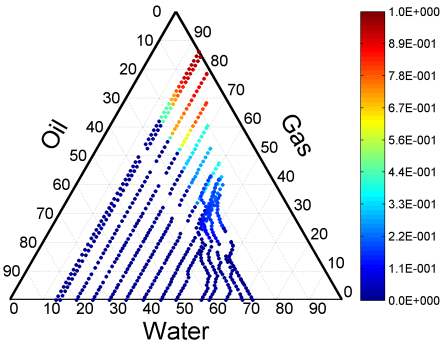

(f) k_{rg}

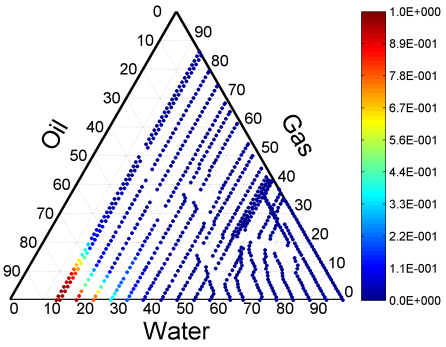

(g) k_{ro}

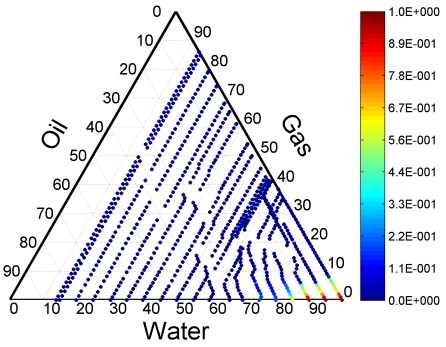

(h) k_{rw}

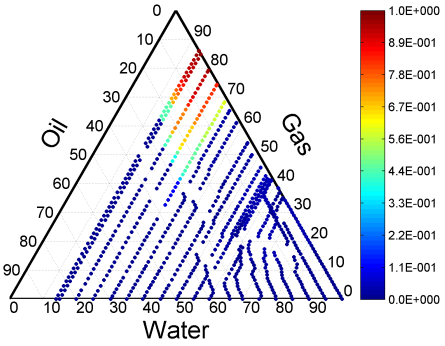

(i) k_{rg}

Figure 6.4: Simulated relative permeabilities of network D: (a)-(c) for strongly water-wet (case 1), (d)-(f) for weakly oil-wet (case 2) and (g)-(i) for strongly oil-wet (case 3) conditions. Note the difference in the scale of the individual relative permeabilities.

6.4 COMPARISON BETWEEN SINGLE- AND MULTI-DISPLACEMENT

To demonstrate the impact of single- vs. multi-displacement on the estimation of residual oil, we used network A (Berea Sandstone). We assumed that the network is fully filled with water as the initial state. The oil-water contact angle $\theta_{ow}^{dr} = 0^o$ is assigned to all the pores. Then, the network was flooded with oil (primary drainage) until the irreducible water saturation, contained in the clay porosity (Valvatne and Blunt, 2004), was reached. After that, we changed the contact angles of the pores that have been invaded by oil to mimic ageing. The oil/water contact angles were distributed uniformly with a minimum of 20^o and a maximum of 72^o. Then, we ran the water invasion up to a predefined water saturation of 50%. Finally, we injected gas into the network until no more oil was produced at the outlet of the network. At this point the simulations were stopped. The interfacial tensions are given in Table 2.1 and the saturation paths of the two types of displacement during gas flood are presented on the ternary diagram of Fig. 6.5. At the early stages of gas injection, gas displaces oil only from the largest pores that are part of an outlet connected to an oil cluster. This is represented in the straight part of the saturation path in both displacements. In the single-displacement scenario, oil becomes trapped because the oil that is still connected to the outlet is contained in small pores which have a high capillary entry pressure. This leads gas to displace both, oil and water, forming the curved part of the saturation path. Finally, all oil becomes trapped and cannot be produced any longer. However, the water phase is still connected to the outlet, leading the gas to displace water only. This results in a predicted residual oil saturation of 17.5%. However, in the multi-displacement scenario, the trapped oil is still able to move within the network and can reach the outlet. In this case, both oil and water are produced simultaneously and, hence, significantly lower residual oil saturation of 5.5% can be achieved. This is a major difference compared to the corresponding single-displacement scenario.

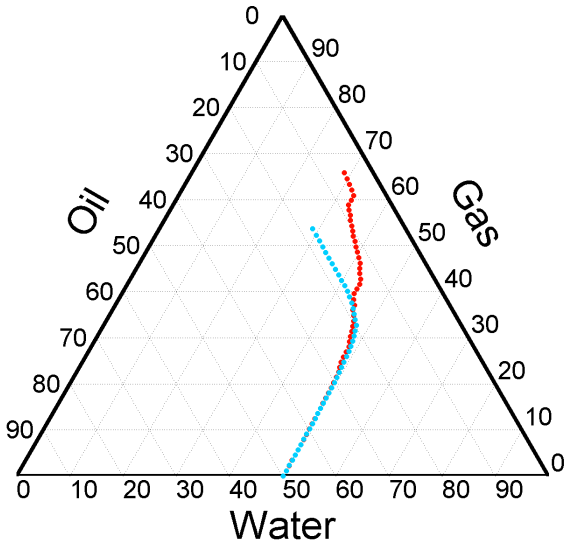

Figure 6.5: Simulated saturation paths using single-displacement (blue path) and multi-displacement (red path) during tertiary gas injection.

6.5 SUMMARY AND CLOSING REMARKS

In this chapter, we used four different realistic 3D pore-networks, extracted from pore-space reconstruction methods and CT images, to demonstrate the capability of our new model to compute the relative permeabilities for three wetting systems. The networks represented sandstone and carbonate rocks. We studied the emergent behaviours and resulting flow properties of the networks and wetting systems. The carbonate networks exhibited some discontinuities in the saturation paths. This was attributed to large pore volumes ("vugs"). In the strongly oil-wet cases, the saturation paths showed that gas displaces oil, except for high water saturations. The residual oil saturation reached very low values for strongly water- and oil-wet systems during the gas flood in all the four networks. This was because that the hydraulic connectivity of oil was maintained by the oil layers and films in the water-wet and oil-wet systems respectively. The size of the three-phase region was controlled by the connate water saturation and the minimum residual oil saturation during the water flood. Based on their respective coordination numbers as the network connectivities decrease, the water flood residual oil saturations increases in the water-wet systems. However, the water flood residual oil saturations in weakly oil-wet systems are not simply correlated to the network connectivity. The oil relative permeability in the strongly oil-wet case was enhanced by the presence of additional films around water, compared

to the weakly oil-wet case in which the oil phase was less well-connected. This resulted in a lower oil relative permeability at identical saturation combinations. We observed a numerical feature that also occurs in laboratory experiments: The saturation paths in the weakly oil-wet system intersect each other at different gas relative permeabilities. This emphasised the importance of the flow history. The water relative permeability held a non-zero value in the water-wet systems. In contrast, in oil-wet systems the water relative permeability dropped to zero. This behaviour was attributed to the presence or absence of water wetting films. Gas injection led to a significant improvement in oil recovery, compared to water injection. This was attributed to the favourable displacements types which occurred in each flood. Finally, we ran a simple simulation to manifest the impact of single- and multi-displacement on residual oil. A significantly lower residual oil saturation was reached using multi-displacement scenario compared to the corresponding single-displacement scenario.

Part II

PORE- TO RESERVOIR-SCALE SIMULATIONS

In this part we apply the network model and employ its three-phase flow functions in continuum-scale reservoir simulations to investigate different three-phase flow effects which occur at field-scale. As an application example, we consider WAG injection for different wetting systems, demonstrating the uncertainties inherent to three-phase flow functions and hence the importance of applying the "correct" relative permeability model, even if the reservoir was subjected to history-matching and uncertainty analysis and the geology is thought to be well-understood.

7

PORE- TO RESERVOIR- SCALE

7.1 INTRODUCTION

In this chapter, we show the capability of our pore-network model to provide three-phase flow function (relative permeabilities and capillary pressures) that can be fed into continuum-scale reservoir simulations. Our pore-network model is used to generate the flow functions for different wetting systems. We use the 3D pore-network extracted from pore-space reconstruction methods of Berea sandstone (Fig. 3.1) as input in our pore-network model to compute the flow functions. The main network parameters are shown in Table 3.2. The data structure for this network was discussed in chapter 3. The flow functions are then employed in a commercial reservoir simulator to model field-scale WAG injection and address the following points: (1) It is well-known that uncertainty in predicting oil recovery depends on the uncertainty in the geological model and hence novel workflow exist which aim to reduce uncertainty and optimise recovery (Peters et al., 2010). However, if the the geology of the reservoir is thought to be well understood, is the choice of the relative permeabilities and capillary pressures still critical to forecast the oil recovery accurately, especially during tertiary gas injection? In other words, how large is the uncertainty in flow functions compared to the uncertainty in a history-matched geological model? To answer this question we analyse the effects of different three-phase relative permeabilities models, i.e. from network model and from empirical models, on field-scale recovery during WAG injection for different reservoir wettability conditions. We use a geological model with different equiprobable stochastic realisation of permeability and porosity. We then compare the uncertainty arising from the relative

permeability models to uncertainty in the geological model. (2) As we have seen in chapter 6, different wetting systems give different saturation paths and flow functions. If these flow functions are used in a reservoir model, how will they affect oil recovery? (3) What is the incremental oil recovery due to WAG injection in a given reservoir model?

In the following sections, we describe the reservoir model. After that, we present the wetting systems that are considered in this chapter. We then discuss the simulations at the pore scale, explaining how the flow functions are derived from the pore-network model. Then, we show the results for numerical simulations of WAG injection at the reservoir scale to demonstrate the impact of pore-scale generated three-phase flow functions vs. empirical flow functions on the sweep efficiency after gas injection for a range of realistic wettability scenarios.

7.2 RESERVOIR MODEL DESCRIPTION

We used a completely synthetic field model, the Brugge field, which has been constructed by the Dutch Organization for Applied Scientific Research (TNO) as a benchmark study for closed-loop reservoir optimization (Peters et al., 2010). The dimensions of the Brugge filed are approximately 10 x 3 km. The field consists of four main reservoir zones: Schelde, Maas, Waal, and Schie. The properties of these zones are typical for a North Sea Brent-type field (Table 7.2). The field has a large boundary fault at its northern edge and one internal fault. The reservoir model contains 30 wells in total, 20 producers and 10 injectors. The "truth" model consists of 20 million grid cells and was populated with the common reservoir description properties such as sedimentary facies, NTG thickness ratio, porosity, permeability and water saturation. Then this model was upscaled to a 450,000 grid-cell model, with average cell dimensions of 75x75x2.5m. The upscaled model was used to obtain synthetic production data, which comprise the input for history matching. This model has not been disclosed. Hence well data and regional knowledge of the geology are used to generate a new geological model comprising 60,000 grid cells (Fig. 7.1). The main parameters of the model are shown in Table 7.1. Indeed, 104 equiprobable stochastic realizations

of the reservoir properties were created, using four selected control parameters: facies, fluvial, porosity and permeability. This reflects the geological uncertainty. Further details on the modelling are given by Peters et al. (2010).

Table 7.1: Main reservoir simulation parameters.

PARAMETERS	VALUES
Pressure	2,466 psi at 5577 ft depth
Free water level	5505 ft
OWC	5498.5 ft
GOC	4900.15 ft
Capillary pressures	Fig. 7.2
Pore compressibility	3.5x10-8 1/psi
Well constraints	Producers 5000 rb/d, 725 psi
	Injectors 10000 rb/d, 2611 psi
Water cut constraint	90% on the producers

We used the 60,000 cell reservoir model to run different WAG injection scenarios, which are summarised in Table 7.3. In all scenarios, we simulate a primary depletion for the first 21 months before commencing the first flood. There is no gas cap in the model.

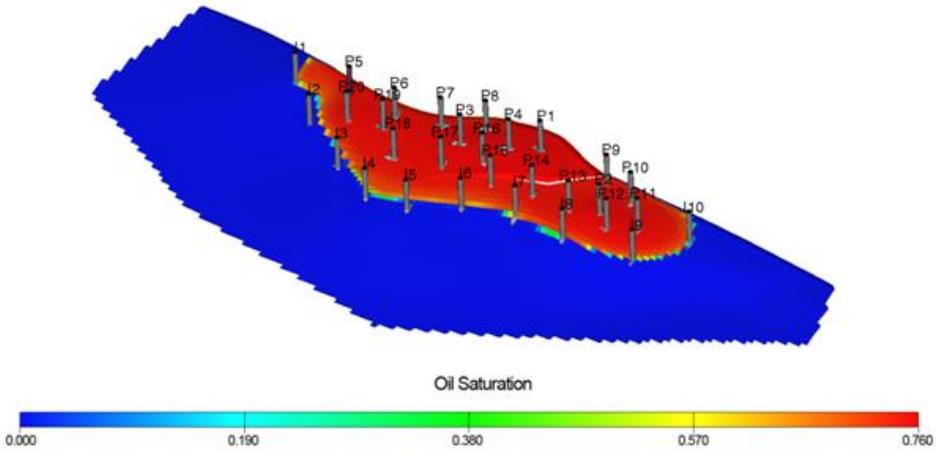

Figure 7.1: Initial oil saturation of the Brugge field.

Table 7.2: Main reservoir zones properties (Peters et al., 2010).

FORMATION[1]	SCHELDE	MAAS	WAAL	SCHIE
Average thickness, m	10	20	26	5
Average porosity, %	20.7	19.0	24.1	19.4
Average permeability, mD	1105	90	814	36
Average NTG, %	60	88	97	77
Depositional environment	Fluvial	Lower shoreface	Upper shoreface	Sandy shelf

[1] The zones are ordered from the top to bottom of the reservoir.

Table 7.3: WAG injection Scenarios.

SCENARIO INDEX	FLOODING SEQUENCE	FIRST FLOOD
1 (base case)	Waterflooding for 42.6 years	Water
2	Only gas injection for 42.6 years	Gas
3	21 WAG cycle, Water 1 year, Gas 1 year	Water
4	21 WAG cycle, Water 1 year, Gas 1 year	Gas
5	7 WAG cycle, Water 3 year, Gas 3 year	Water
6	7 WAG cycle, Water 3 year, Gas 3 year	Gas
7	4 WAG cycle, Water 5 year, Gas 5 year	Water
8	4 WAG cycle, Water 5 year, Gas 5 year	Gas

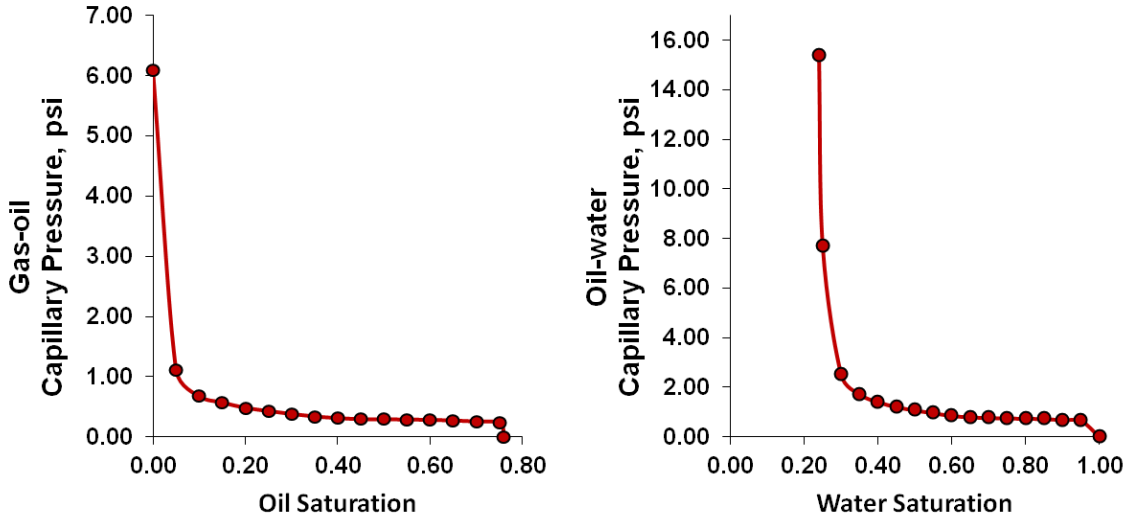

(a) Gas-oil capillary pressure

(b) Oil-water capillary pressure

Figure 7.2: Capillary pressures obtained for two-phase gas-oil and oil-water systems using our network model.

7.3 TWO-PHASE RELATIVE PERMEABILITY

We used our network model to obtain the two-phase relative permeability for oil-water and gas-oil systems. In the oil-water system, we injected oil into the fully water-saturated network to obtain $k_{ro(w)}$, k_{rw} and P_{cow}. In the gas-oil system, we injected gas into the fully oil-saturated network at connate water to obtain $k_{ro(g)}$, k_{rg} and P_{cgo}. The resulting capillary pressures curves were used for initialising the reservoir model.

7.4 THREE-PHASE RELATIVE PERMEABILITY BY NETWORK MODEL

We used our network model to mimic the reservoir wettability state and the flooding sequence. Initially, the network is fully saturated with water (water-wet rock). The network is then flooded with oil up to connate water saturation, S_{wc} to mimic oil migration into the reservoir, during primary drainage. This represents the initial state of the reservoir model. Then, contact angles are changed, modelling the alteration of the reservoir wettability during ageing. Different degrees of ageing, from water-wet to oil-wet, were modelled. After that, we ran the imbibition process up to a predefined water saturation S_{wi} to model reservoir production during waterflooding. Finally, we simulated gas injection (tertiary gas injection) in the network to model oil production in the reservoir during gas injection. We repeated the network simulation for different S_{wi} to generate a data set that reasonably represents the full range of three-phase relative permeabilities in the three-phase saturation region.

7.5 THREE-PHASE RELATIVE PERMEABILITY USING EMPIRICAL MODELS

We used the two-phase relative permeability generated by the network model (section 7.3) to calculate three-phase relative permeability from the empirical models of Stone (1970, 1973). Stone proposed these two empirical models to calculate three-phase relative permeabilities. He used two sets of two-phase relative permeabilities, for oil-water and gas-oil, to compute the three-phase relative permeabilities. He made two important assumptions: (1) the relative permeabilities

of water and gas are function of their own saturations only. (2) The flow of oil is blocked by water and gas, which is follow from the assumption that the system is water-wet. Hence, oil relative permeability is a function of water and gas saturations. The equations of Stone I (Stone, 1970) and Stone II (Stone, 1973), which were used to calculate oil relative permeability are given in Appendix C.

7.6 WETTING SYSTEMS

We used the generated two- and three-phase relative permeabilities and capillary pressures as inputs for the reservoir model. We considered two different wetting systems for which the parameters are presented in Table 7.4. The first system is water-wet, the second is strongly oil-wet. For the latter, we generate relative permeability in two ways:

1. Non-uniform wettability of the pore space (case 2a) as a result of ageing as proposed by Kovscek et al. (1993). Under these conditions, oil layers can be present in aged oil-wet pores, surrounded by corner water and bulk water or gas phases. The corresponding thermodynamic criteria for layer collapse have been derived by van Dijke et al. (2007).

2. Uniform wettability (case 2b) where oil can be present as a very stable corner film surrounding bulk water or gas phases. The layers in the non-uniform wettability system are conditionally stable as opposed to the oil wetting films in the uniform wetting system. For the uniform wettability case, we ran the simulation slightly different from what has been described in section 7.4; here we assumed that the initial state is a network which is fully saturated with oil at connate water saturation. Then, we flooded it with water up to a predefined water saturation S_{wi}. Finally, we simulate the gas injection (secondary gas injection) in the network until residual oil was reached.

Figs. 7.3–7.5 show the saturation paths resulting from gas injection at different S_{wi} with corresponding three-phase relative permeabilities k_r are generated by the network model for water-wet system, oil-wet system with non-uniform wettability, and oil-wet system with uniform wettability, respectively. There are

several important observations: For the water-wet system, the residual oil saturation is higher after waterflooding than after the corresponding gas injection. The high residual oil saturation after the waterflooding is attributed to the snap-off of oil filled pores by the surrounding water wetting films. This causes oil clusters to break into smaller ones, some of which become trapped. This reduces the phase connectivity. For the oil-wet system, the uniform wettability case leads to very low residual oil for both, water injection and gas injection. This is because of the presence of oil wetting films at the pore corners, which are stable and thus enhance the connectivity of oil throughout the network. However, in the non-uniform wettability case, the residual oil is higher compared to the uniform wettability case because of the presence of oil layers, which are less stable than oil wetting films.

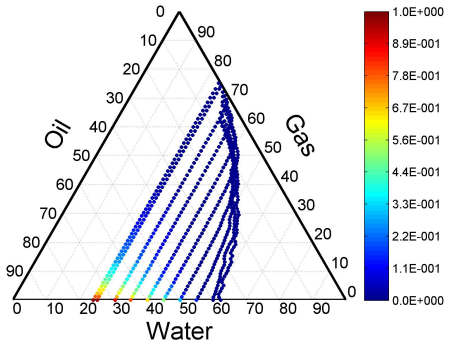

(a) k_{ro}

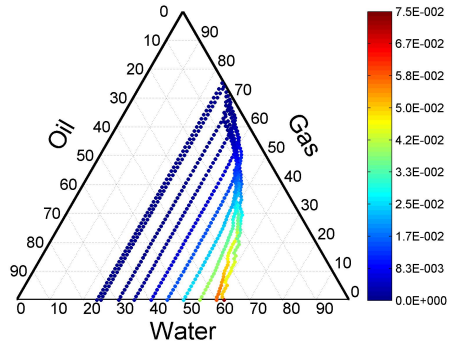

(b) k_{rw}

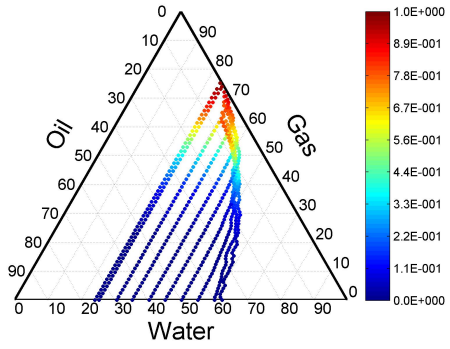

(c) k_{rg}

Figure 7.3: Network derived saturation paths and relative permeabilities during tertiary gas injection for water-wet system (case 1). Colour scale indicates the value of the respective relative permeability along the saturation path.

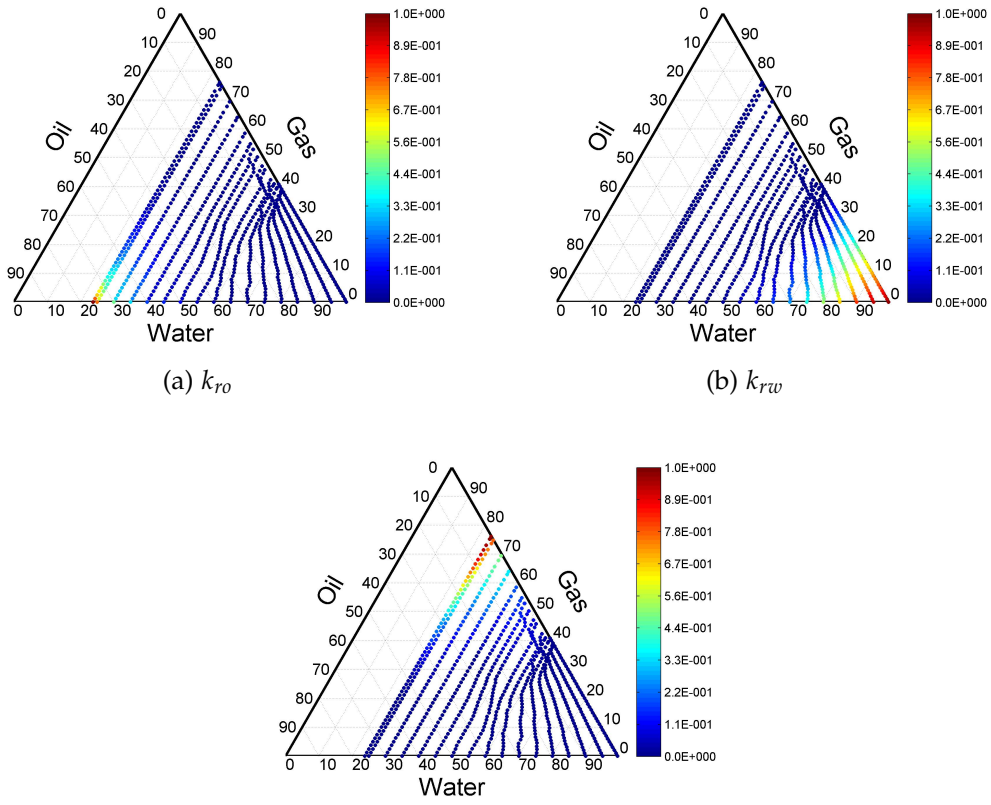

(a) k_{ro} (b) k_{rw}

(c) k_{rg}

Figure 7.4: Network derived saturation paths and relative permeabilities during tertiary gas injection for oil-wet system with non-uniform wettability (case 2a). Colour scale indicates the value of the respective relative permeability along the saturation path.

Table 7.4: Properties of the wetting systems

WETTABILITY STATE	CASE 1	CASE 2
θ_{ow}, degree	0-30	140-160
θ_{go}, degree	0.0	0.0
θ_{gw}, degree	0-25.3	105.4-112.9
σ_{ow}, mN/m	48	48
σ_{go}, mN/m	19	19
σ_{gw}, mN/m	67	67
Wetting order[1]	water-oil-gas	oil-gas-water

[1] From most to least wetting phase.

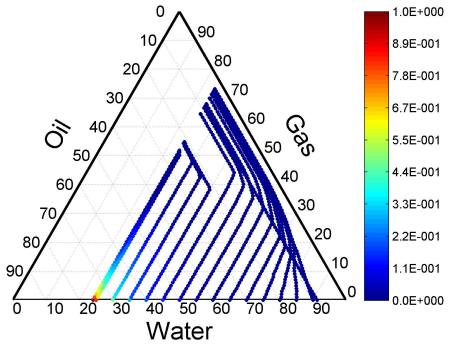

(a) k_{ro}

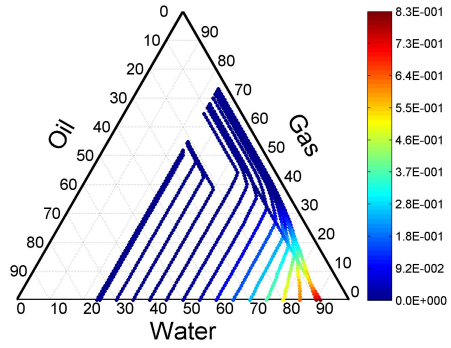

(b) k_{rw}

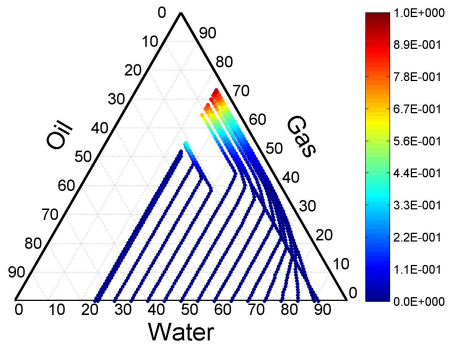

(c) k_{rg}

Figure 7.5: Network derived saturation paths and relative permeabilities during secondary gas injection for oil-wet system with uniform wettability (case 2b). Colour scale indicates the value of the respective relative permeability along the saturation path.

7.7 APPLICATION OF RELATIVE PERMEABILITY MODELS TO FIELD-SCALE SIMULATIONS

To study the efficiency of WAG injection in reservoirs of different wettability we consider two wetting systems that have the same flooding sequence (sections 7.4 and 7.6): a water-wet system (case 1) and an oil-wet system with non-uniform wettability (case 2a). Figure 7.6 shows the oil recoveries for the scenarios listed in Table 7.3. We use the relative permeabilities that were generated by the network model for the water-wet system and the oil-wet system with non-uniform wettability (Table 7.4). For the water-wet system, the lowest oil recovery is found when only one fluid, water (scenario 1) with oil recovery of 43.3% or gas (scenario 2) with oil recovery of 43.1%, is injected. Recovery can be improved by WAG injection. An incremental increase of 2.3% in oil recovery was predicted. In the WAG injection scenarios which we have run, we did not observe significant changes in the incremental recovery based on the number of the WAG cycles. However, it may be possible to further optimise WAG injection and incremental recovery by using different gas slug sizes and WAG ratios. We have not studied this as we are only interested if WAG injection can lead to a noticeable improvement in the overall recovery for the Brugge field and how the predictions vary due to uncertainties in the flow functions, particularly when comparing empirical and network models, and uncertainty in geology, using from the different geological realisations of the Brugge field. For the oil-wet system, waterflooding (scenario 1) yields the lowest oil recovery 41.5%. WAG injection increases the oil recovery by 2.7%. These behaviours are similar to the water-wet system. However,for gas injection into an oil-wet system, oil recovery is even higher than for WAG injection at 48.0%. For real field applications, however, the availability of gas may be become an issue and hence WAG may be more economical.

7.8 GEOLOGICAL UNCERTAINTY VS. UNCERTAINTY IN FLOW FUNCTIONS

We used 13 of the 104 equiprobable geological realisations to compare the uncertainty of the geological model with the uncertainty arising from the flow functions where we used three physical models, Stone I, Stone II and our network

model. Since differences in WAG cycles did not affect the incremental recovery, we ran simulated with 21 slugs of gas/water injection length for 1 year each (scenario 3). This was done for both the water- and oil-wet reservoirs.

Fig. 7.7a and Fig. 7.8a show the resulting oil recovery for WAG injection considering different geological and physical models for water-wet and oil-wet system, respectively. In both systems, the variation of the recovery factor is around 4.5% (absolute) across all models and flow functions. This value represents the uncertainty in predicted oil recovery during WAG as a result of the combined uncertainties in the geological models and relative permeability models. When separating the contributions from geological uncertainty and uncertainty in the three-phase model, we observe that for the water-wet system that the difference between the minimum and maximum recovery factor due to different geological realisations is 1.6%, 1.7% and 1.5% for the network model, Stone I and Stone II, respectively. For the oil-wet system, similar numbers are observed: 1.4%, 1.7% and 1.2%, respectively. To compute variation in predicted oil recovery due to uncertainties in the different relative permeability models, we averaged the oil recoveries of the different geological realisations for each relative permeability model (Fig. 7.7b and Fig. 7.8b). For water-wet system, the difference between the averaged oil recoveries predicted by the network model and Stone I is 2.8% and between network model and Stone II is 1.5% (both absolute); the maximum difference in recovery factor solely based on the different relative permeability factors is 4.3%. For the oil-wet system, the differences between the network model and Stone I are 3.0% and between the network model and Stone II are 0.5% (both absolute); the total difference is 3.5%. These figures suggest that the uncertainty in the prediction of oil recovery caused by using different relative permeability models for three-phase flow processes encountered in IOR and EOR can be at least as big the uncertainty in predicted recoveries when using different equiprobable geological models. Using the "wrong" three-phase flow model in a reservoir simulation, even if the model was history matched for two-phase flow, may hence greatly impact the decision if a tertiary gas injection or WAG scheme is commercially viable or not.

7.9 EFFECT OF PORE-SCALE UNIFORM VS. NON-UNIFORM WETTABILITY ON THE OIL RECOVERY OF RESERVOIR-SCALE

We also studied the impact of uniform and non-uniform wettability at the pore-scale in the oil-wet system on oil recovery (Fig. 7.9). The uniform wettability case yields slightly lower oil recovery compared to the non-uniform wettability case where only water or gas are injected (scenarios 1 & 2). However, the effect of assuming uniform pore-scale wettability on oil recovery for the different WAG injection scenarios is only minor. This may be because the system which we consider here is strongly oil-wet. Hence the oil layers in the non-uniform wettability case are as stable as the oil wetting films in the uniform wettability case. Therefore the oil in both systems has good hydraulic connectivity. This results in similar oil relative permeabilities and hence field-scale recovery factors.

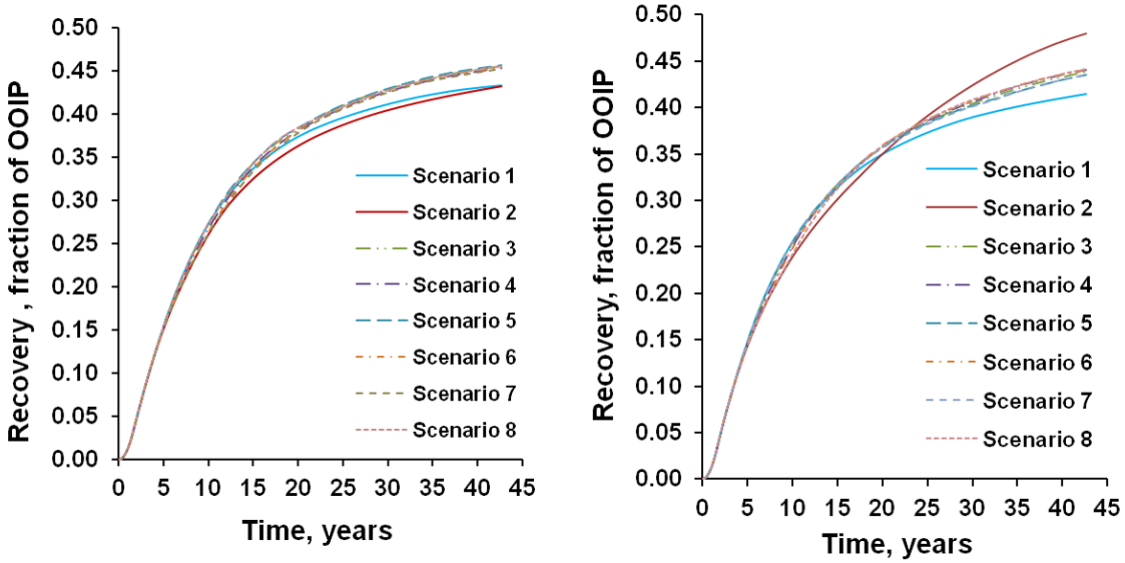

(a) Water-wet system

(b) Oil-wet system

Figure 7.6: Simulated oil recovery for different wetting systems and different WAG scenarios (Table 7.3) using network derived flow functions.

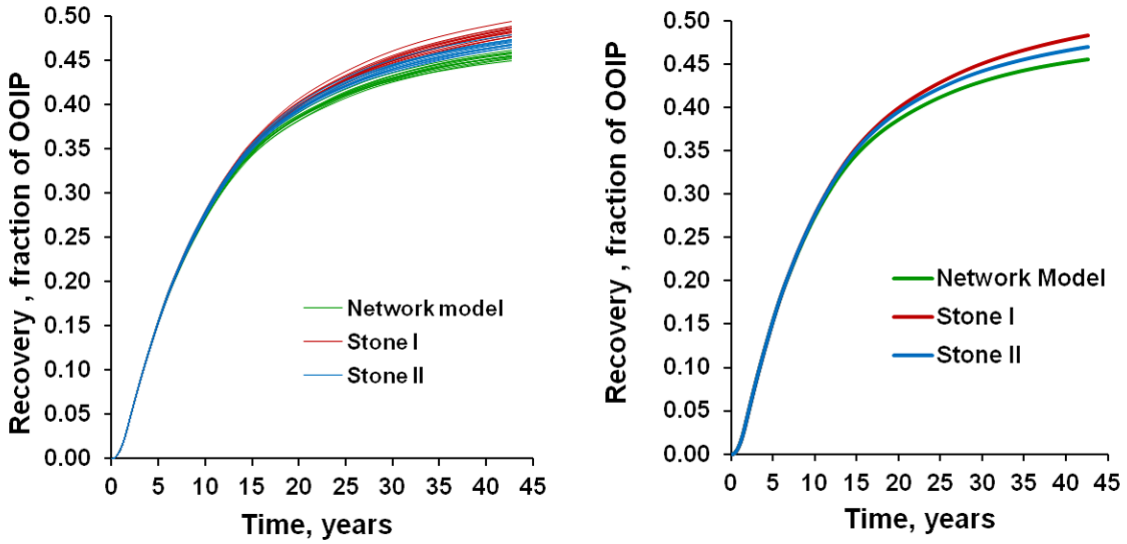

(a) different geological models

(b) averaged recovery of different geological models

Figure 7.7: Simulated oil recovery during WAG injection (scenario 3) for 13 different geological and 3 different relative permeability models in a water-wet reservoir.

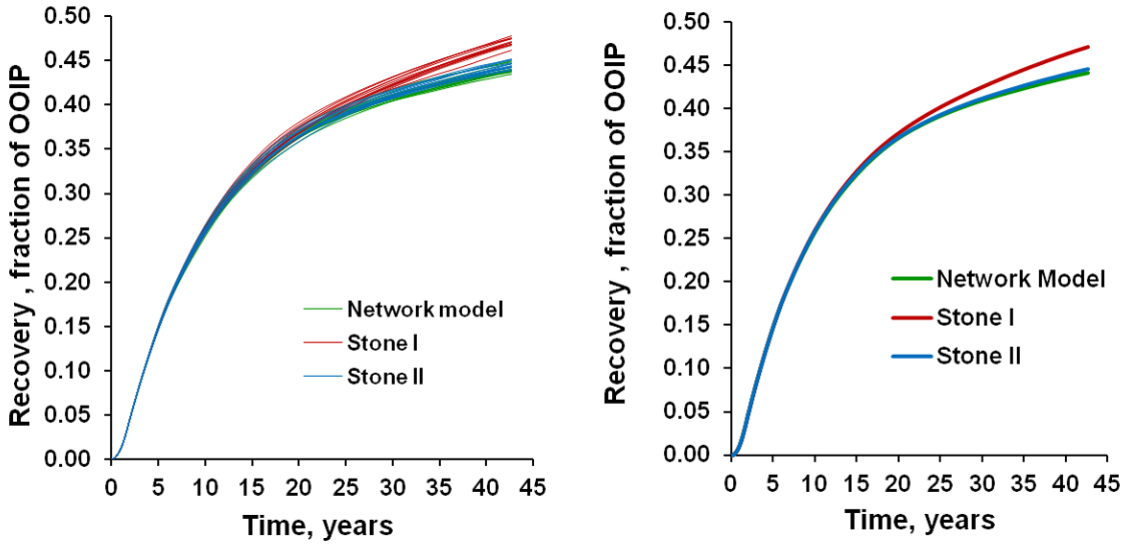

(a) different geological models

(b) averaged recovery of different geological models

Figure 7.8: Simulated oil recovery during WAG injection (scenario 3) for 13 different geological and 3 different relative permeability models in an oil-wet reservoir.

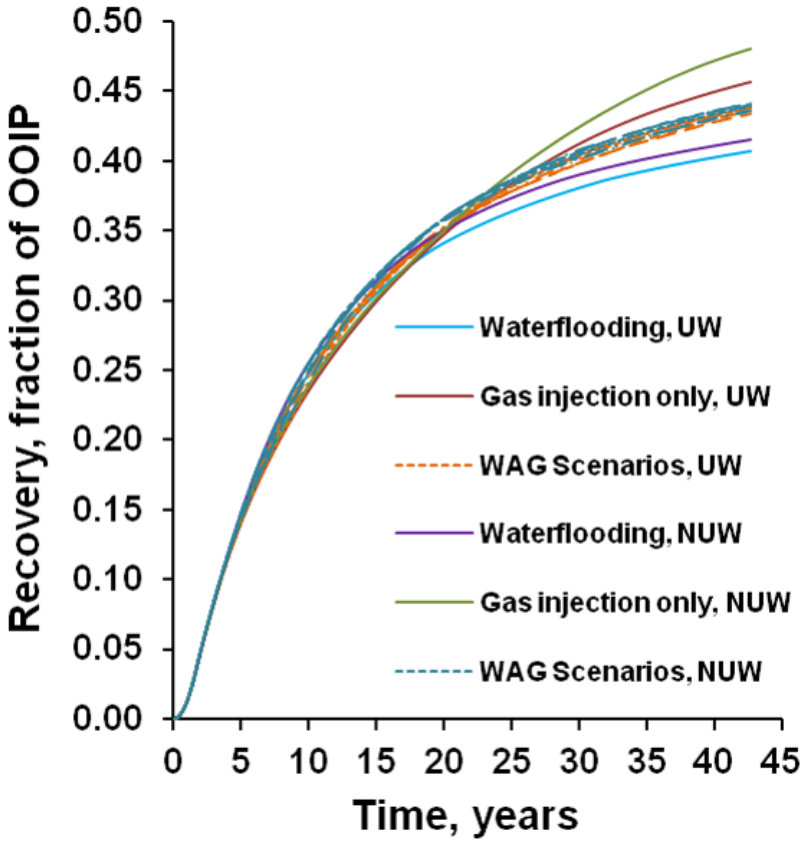

Figure 7.9: Simulated oil recovery for the different WAG scenarios in the two oil-wet systems, assuming uniform wettability (UW) and non-uniform wettability (NUW) of the pore-scale.

7.10 SUMMARY AND CLOSING REMARKS

In this chapter, we applied our new, physically-based, and reliable three-phase pore-network model to field-scale reservoir simulations. We showed that our model can be used for the simulation of any number of WAG cycles of arbitrary wettability (chapter 4) to analyse the efficiency of field-scale oil recovery during WAG in the presence of geological uncertainty. We investigated the effects of different three-phase relative permeability models on field-scale recovery during WAG injection for different wetting systems using the synthetic Brugge field, which comprises 104 different equiprobable geological realizations (Peters et al., 2010).

To generate the three-phase relative permeability models, we used pore networks extracted from pore-space reconstruction methods of Berea sandstone as input into our network model. A constrained set of parameters was tuned to mimic the wetting state of the given reservoir. A water-wet and oil-wet reservoir was considered. Corresponding two-phase relative permeabilities computed with the network model served as input for empirical three-phase relative permeability models (Stone I and Stone II). We also computed three-phase relative permeability models directly from the pore-network simulations.

Simulations at the pore scale show that the residual oil saturation for a water-wet system is higher during waterflooding than the corresponding residual oil saturation during gas injection. This is because of snap-off of oil filled pores by the surrounding water wetting films. This cause oil clusters to breakup and hence traps oil clusters at the pore-scale. For the oil-wet system, the uniform wettability case leads to very low residual oil during both, water injection and gas injection, because highly stable oil wetting films are present in the pore corners. These maintain the connectivity of oil in the network. The presence of the oil layers in the non-uniform wettability case leads to a higher residual oil saturation compared to the uniform wettability. This is because, in this scenario, oil wetting films are more stable than oil layers.

Simulations at the reservoir scale show that the lowest oil recovery for the water-wet system case is obtained by injecting only one fluid (gas or water). Recovery can be improved by over 4% (absolute) during WAG injection in agreement with typical values that were reported in real fields (Christensen et al., 2001), see chapter 1. For the oil-wet system, recovery behaviours are similar to the water-wet system with the exception that pure gas injection leads to the highest oil recovery, i.e. recovery factors that are even higher than during WAG injection.

We also investigated how uncertainty in the geological model, expressed in different realisations of the permeability and porosity distribution, and fundamental uncertainty in three-phase flow physics, expressed by the different three-phase flow models effects the prediction of oil recovery. The uncertainty in prediction oil recovery due to the different three-phase relative permeability models is as large as the uncertainty arising from the different geological models. Combining both, geological uncertainty and uncertainty in the three-phase model, leads to the largest differences in predicted oil recovery. This implies that care must be taken when choosing the relative permeability model for tertiary gas injection or WAG as geological uncertainty does not mask uncertainty in the fundamental flow physics even if the geological model was history matched for two-phase flow. The choice of three-phase flow model can greatly impact the decision of the commercial viability of a WAG project.

8

SUMMARY, CONCLUSIONS AND FUTURE WORK

8.1 SUMMARY AND CONCLUSIONS

We have developed a reliable and physically-based pore-network model that is capable of simulating primary drainage, imbibition, secondary or tertiary gas injection, and any number of WAG cycles for arbitrary wetting systems which mimic the wettability state of a given reservoir rock. Unlike other models, our model *combines* three main features:

1. It employs a novel thermodynamic criterion for formation and collapse of oil layers (van Dijke et al., 2004a, 2007). The new model thus captures wetting film and layer flow of oil adequately, which affects the oil relative permeability at low oil saturation and leads to more accurate prediction of residual oil.

2. It accounts for multiple displacement chains where injection of one phase at the inlet triggers a chain of interface displacements throughout the network. This allows for more accurate modelling of the mobilization of disconnected phase clusters that arise during higher order (WAG) floods.

3. The model takes realistic 3D pore-networks extracted from pore-space reconstruction methods and CT images as input, preserving both topology and pore shape of the original rock.

The new model calculates the relative permeability and capillary pressure functions for two- and three-phase flow. For water-wet systems, the model has been validated against the two- and three-phase relative permeabilities experimental data of the Berea sandstone sample reported by Oak (1990). For two-

phase flow, the predicted values of the relative permeabilities of both, oil and water, are in agreement with the experimental data. For three-phase flow, the predicted three-phase water relative permeability curves are in perfect agreement with experimentally measured data. The predicted three-phase gas relative permeability matches the experimental data. Predicted oil relative permeabilities are scattered in a similar manner as the measured oil relative permeability. This is caused, both experimentally and numerically, by the different saturation histories. Additionally, a comparison with the well-established pore-network model of Piri and Blunt (2005a,b) was preformed. Our model gave a more accurate prediction of the experimental data of Oak (1990) compared to the model of Piri and Blunt (2005b). This emphasises the need for accurate modelling of the oil layers.

For validating our network model in an oil-wet system, micromodel experiments that were conducted by Sohrabi et al. (2000, 2001, 2004) were simulated. Oil recovery profiles of the simulations and experiments were in very good agreement. Our predictions were in better agreement with the experimental data compared to pore-network model developed by van Dijke et al. (2006). We also performed a qualitative visual comparison of simulated and experimental fluid distributions. A satisfactory match of fluid distributions, capturing the main three-phase flow physics like multiple displacements, between experiments and model was achieved.

A sensitivity analysis has been carried out using the full 3D network model for one sandstone and three carbonate rock samples to predict three-phase relative permeabilities under water-wet and different oil-wet conditions during gas injection. We found that very low residual oil saturations can be reached during the gas flood because of the presence of intermediate wetting phase (oil) layers in the water-wet system and oil wetting films in the oil-wet system. Both help to maintain oil connectivity at low oil saturation. The oil relative permeability depends on the presence of oil films in oil-wet systems, particularly for the strongly oil-wet case where surrounding oil films are present, both in gas-filled and water-filled pores. The gas relative permeability shows little sensitivity to the degree of oil wettability in the well connected Berea sandstone network, contrary to the poorly connected carbonate networks. The water relative permeability is very low but non-zero for a large saturation range in the water-wet

system. It drops abruptly to zero in the oil-wet system. There is a significant improvement in the oil recovery in the water-wet system during gas injection because of the formation of oil layers, which provide hydraulic connectivity for the oil. The three-phase region can increase noticeably due to the formation of additional oil films around water in the strongly oil-wet system compared to the weakly oil-wet system. This already leads to very low residual oil saturations during the water flood. Large discontinuities in the saturation paths of the carbonate networks can be observed, which we have attributed to the large volumes occupied by a few large pores (vugs) in those networks.

We then used the network model to simulate WAG in a synthetic reservoir model to demonstrate how pore-scale generated three-phase flow functions impact sweep efficiency after gas injection and WAG for a range of realistic wettability scenarios compared to empirical three-phase flow functions. The detailed physics of three-phase flow at the pore-scale which are captured in our network model, are translated into flow functions i.e. relative permeabilities and capillary pressures, that can be used directly as 2D tables in a commercial reservoir simulator. We investigated oil recovery during WAG for different wetting systems using flow functions from our pore-network model for these cases. These flow functions were input into a synthetic field-scale model in which the WAG injection was implemented. The main conclusions of this work are:

1. Microscopic displacement processes in the network model can be transferred to reservoir-scale through appropriate flow functions.

2. Oil recovery can be improved by over 4% during WAG injection compared to injecting one fluid only.

3. Uncertainty in the predicted oil recovery for different relative permeability models is as great as the uncertainty caused by using statistically equivalent geological models. This means that even if history-matching and uncertainty analysis have been done for two-phase flow, and the geology of the reservoir is thought to be well-understood, it is crucial to use the appropriate k_r and P_c models for EOR processes involving three-phase physics flow.

4. The effect of uniform wettability at the pore-level on field-scale oil recovery during WAG injection is only negligible.

8.2 FUTURE WORK

Based on the work that was presented in this thesis, for the future work we would recommend the following:

1. We treat PBF displacement event as a piston-like displacement. Full implementation of the pore-body filling models should be carried out and consider multiple displacements.

2. Implementations of three-phase flow for the arbitrary triangular shapes. Currently, we either characterise the pore cross-sections by Circle-Triangle (equilateral)-Square or an n-cornered star. This might be a difficult task since arbitrary triangular shapes have different corners where fluid occupancy of each corner could be different, leading to different displacements in each corner.

3. We recommend to find a way to redistribute the fluids within the network when clusters merge, as discussed in section 4.5.5.

4. As we have mentioned in chapter 3, that the pore network that were used in this work to represent carbonate rocks were small. This affected the results of the three-phase flow simulations (chapter 6). We recommend to find larger pore networks that will be more representative for carbonates.

5. In this work, we focused on generating the three-phase relative permeability during tertiary gas injection. The model can simulate WAG injection (see chapter 5). We recommend to run WAG injection and compare the relative permeability hysteresis of each phase during different WAG cycles. These relative permeabilities can be fed into a reservoir-scale simulator to simulate WAG injection at field-scale more accurately (chapter 7).

6. For the reservoir-scale simulation, we used only one network to generate the flow functions that were fed into the reservoir model. However, the model is heterogeneous and thus has different rock types. Therefore, we

suggest using more than one network to derive the flow functions and then assign them to different rock types in the reservoir models.

7. In our study at the pore-network, we considered that the phases are immiscible phases. Hence, we our investigation at the field-scale was for immiscible WAG. However, miscible WAG injection is more common the immiscible WAG injection in of the oil fields (Christensen et al., 2001). Investigation on miscible WAG injection is highly recommended, although this might be a challenging task to implement at the pore-scale using network modelling.

8. In our simulations at the field-scale, we considered the most popular WAG ratio which is 1:1 (Christensen et al., 2001). Using different WAG ration might produce different effect on the oil recovery.

9. The model that we used in our field-scale simulation was homogeneous. However, using a heterogeneous model including structural heterogeneity (e.g. fractures) might give different uncertainties in oil recovery using different relative permeability models.

Part III

APPENDIX

A

PORE GEOMETRY

In this appendix, we give all general equations that are required to calculate different parameters of the pore occupied by different fluids. Fig. A.10 show cross-section of a pore at a corner occupied by phase j in the presence of bulk phase i in the centre of the pore.

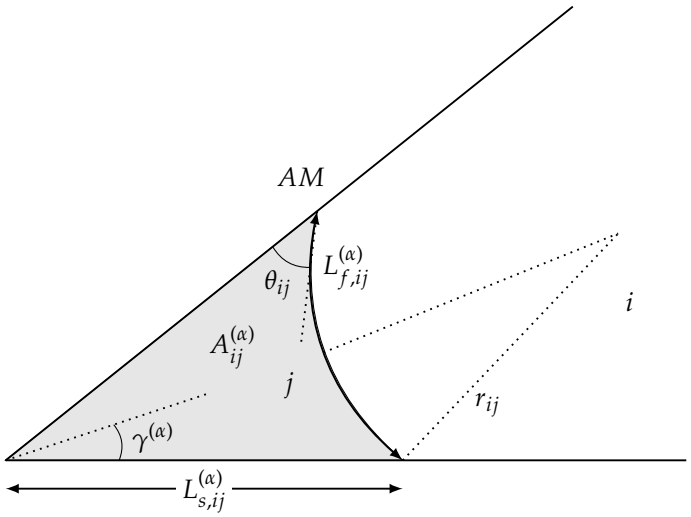

Figure A.10: Phase occupancy in corner with film phase j and bulk phase i. We call j the inner phase of the AM and i the outer phase of the AM.

A.1 PORE GEOMETRY

The area of the shaded region, bounded by AM, in the corner ($A^{(\alpha)}_{ij} = A^{(\alpha)}(r_{ij}, \theta_{ij})$) is defined as

$$A^{(\alpha)}(r_{ij}, \theta_{ij}) = r_{ij}^2 \left(\theta_{ij} + \gamma^{(\alpha)} - \frac{\pi}{2} + cos\theta_{ij} \frac{cos(\theta_{ij} + \gamma^{(\alpha)})}{sin\gamma^{(\alpha)}} \right). \tag{A.1}$$

The contact lengths fluid-solid and fluid-fluid in each corner α are given, respectively, by

$$L_s^{(\alpha)}(r_{ij}, \theta_{ij}) = 2r_{ij}\frac{cos(\theta_{ij} + \gamma^{(\alpha)})}{sin\gamma^{(\alpha)}}, \tag{A.2}$$

$$L_f^{(\alpha)}(r_{ij}, \theta_{ij}) = 2r_{ij}\left(\frac{\pi}{2} - \theta_{ij} - \gamma^{(\alpha)}\right). \tag{A.3}$$

The geometrical functions g and $g^{(\alpha)}$ defined as

$$g(r_{ij}, \theta_{ij}) = \frac{A}{r_{ij}} - cos\theta_{ij}L_s, \tag{A.4}$$

$$g^{(\alpha)}(r_{ij}, \theta_{ij}) = -\frac{A^{(\alpha)}(r_{ij}, \theta_{ij})}{r_{ij}}. \tag{A.5}$$

Where , A and L_s denote the total area and perimeter of the entire cross-section, respectively.

B

DESCRIPTION OF INPUT AND OUTPUT DATA FILES

Our 3-phase pore-network model simulator was written in C++ programming language. The simulator has a GUI (Fig. B.11) on which all main parameters that are required for each run can be specified. However, for very advanced runs where more options are required, the model can read inputs files with defined keywords, explained in section B.1. Before these keywords can be used, the network must be imported, loading the files: *link1.dat*, *link2.dat*, *node1.dat*, and *node2.dat*. These are standard input files which give all the information about the pore-network structure, presented in Table 3.1. Then, another input file (*inputs.data*) which contains the keywords that define the required run.

1. Main model inputs:
    a) Pore-network data. The files: *link1.dat*, *link2.dat*, *node1.dat*, and *node2.dat*.
    b) Wettability distribution, including the interfacial tensions and contact angles.
    c) Linear system solver parameters.
    d) Two- and three-phase floods parameters. Higher order of WAG cycle can be specified using input file, described in section B.1.
    e) Pore shape characterization (e.g. CTS, n-cornered ...).
    f) Oil layers existence criteria.
    g) Wettability sensitivity parameters (e.g. different S_{wi}).
2. Main model outputs:
    a) Floods data: S_o, S_w, S_g, k_{ro}, k_{rw}, k_{rg}, P_{cgo}, P_{cow}, P_{cgw}.
    b) Displacement statistics.

c) Pore occupancy statistics.

d) Cluster statistics.

e) Running time statistics.

f) Real-time plotting, main dialogue window, of saturation path and three-phase relative permeabilities (k_r) and capillary pressures (P_c).

g) Real-time 3D visualization of network three-phase occupancy.

B.1 KEYWORDS OF THE INPUT FILE

1. **FDSQU**: Flooding sequence-Specify the flooding sequence as follow:

   a) Injecting phase (Ph_{inj}): 0 denotes oil, 1 denotes water and 2 denotes gas.

   b) Injecting Phase End Saturation (S_{iend})

   c) Spanning invading Cluster (C_{span})

   d) Oil End Saturation (S_{oend})

   Example:

   FDSQU

$	Ph_{inj}	S_{iend}	C_{span}	S_{oend}
	1	1	0	0
	0	1	0	0
	1	1	0	0
	2	1	0	0

   Note that the first row of the input values of this keyword is used as the initial conditions for the network. In the example above, the first row of inputs indicates that the network is set to be initially filled with water (1). The second row indicate that oil is injected until it saturation reach 1 or residual.

2. **IFT**: Three-phase Interfacial Tensions:

   a) Gas/oil

   b) Oil/water

c) Gas/water

Example:

```
IFT
$      gas-oil    oil-water    gas-water
       19         48           67
```

3. **EVENTSMAX**: The maximum number of invasion events during each flood. It can specify another way of terminating the current flood. This keyword might be very useful during debugging process.

   Example:

```
EVENTSMAX
                125000000
```

4. **MICROMODEL**: For micromodel simulation (0 or 1) Note: if the micromodel simulation set to 1 then you should make the network initially saturated with oil.

   Example:

```
MICROMODEL
                0
```

5. **INIWET**: initial wettability (for the first flood, primary drainage) defined by oil-water contact angle.

   a) Is Distributed contact angles (1 or 0)

   b) Is Cosine contact angles

   c) Min oil-water contact angle

   d) Max oil-water contact angle

   Example:

```
INIWET
$          ConAng(oil/water)
$          isDistr          isCosDistr    min    max
           0                0             0.0    0.0
```

   Note: if MICROMODEL is set to 1 then it would be an oil-wet run. How-

ever, it is still required to assign the oil-water contact angle a value between (0-89) that is automatically translated to (180-91) by the code.

6. **AGEWET**: wettability alteration (ageing)
   a) Is aging active (0 or 1)
   b) Wettability mode (water-wet, oil-wet, mixed-wet etc.)
   c) Is Distributed contact angles (1 or 0)
   d) Is Cosine contact angles
   e) Min oil-water contact angle
   f) Max oil-water contact angle

   Example:

$	isActive	wetMod	isDistr	isCosDistr	min	max
	1	1	1	0	150.0	180.0

7. **RESINF**: make the interface responsive (1) or not responsive (0), this will affect the simulation speed.

   Example:

```
RESINF
        1
```

8. **SENS**: run sensitivity runs or multi-runs using different initial water saturations.
   a) Flood number in which the Swi will be incremented
   b) Initial value of S_{wi}
   c) Increment
   d) Final value of S_{wi}

   Example:

$	Flood number	initial value	increment	Final value
	2	0.00	0.05	1.01

9. **SNOF**: (1 or 0) activate the snap-off displacement in the three-phase runs.

   Example:

   ```
   SNOF
            1
   ```

10. **LC**: Layer collapse criterion, 1=thermodynamically (including the geometric), 0=geometric only

    Example:

    ```
    LC
       1
    ```

11. **SPA**: Shortest Path Algorithm

    $ 0-BFM_WTR...1-BFM_STD

    Example:

    ```
    SPA
         1
    ```

12. **GPU**: Global Pressures update

    $ 0-based on target pressure (default) ; 1- based on effective pressure

    Example:

    ```
    GPU
          0
    ```

13. **BC**: Outlet Boundary Pressure

    $ 0-Constant (default) ; 1-same as maxHistPressure; 2- varied

    Example:

    ```
    BC
       0
    ```

14. **DEBUG**: Debug mode

    $ 0-no debug (default -0); 1-debug

    Example:

    ```
    DEBUG
              0
    ```

15. **GSL**: Gas Layer

    $ Not allowed=0 (defaulet); allowed=1

    Example:

```
GSL
        0
```

16. **TRC**: Saturation Path Tracking. This is done by selecting the phase at the outlet to be produced to track the experiment data

    $ 0-No tracking (defult); 1-tracking

    Example:

```
TRC
        0
```

17. **CUTOFF**: Cut off value.

    $ % of pore volume at which displacment will forced to be completed to avoid volume inconsistancy. defult is 0.001

    Example:

```
CUTOFF
                0.001
```

18. **SUBDOM**: Using only part of the network for the simulation.

    $ From x1 to x2. Default is 0 1

    Example:

```
SUBDOM
                0   1
```

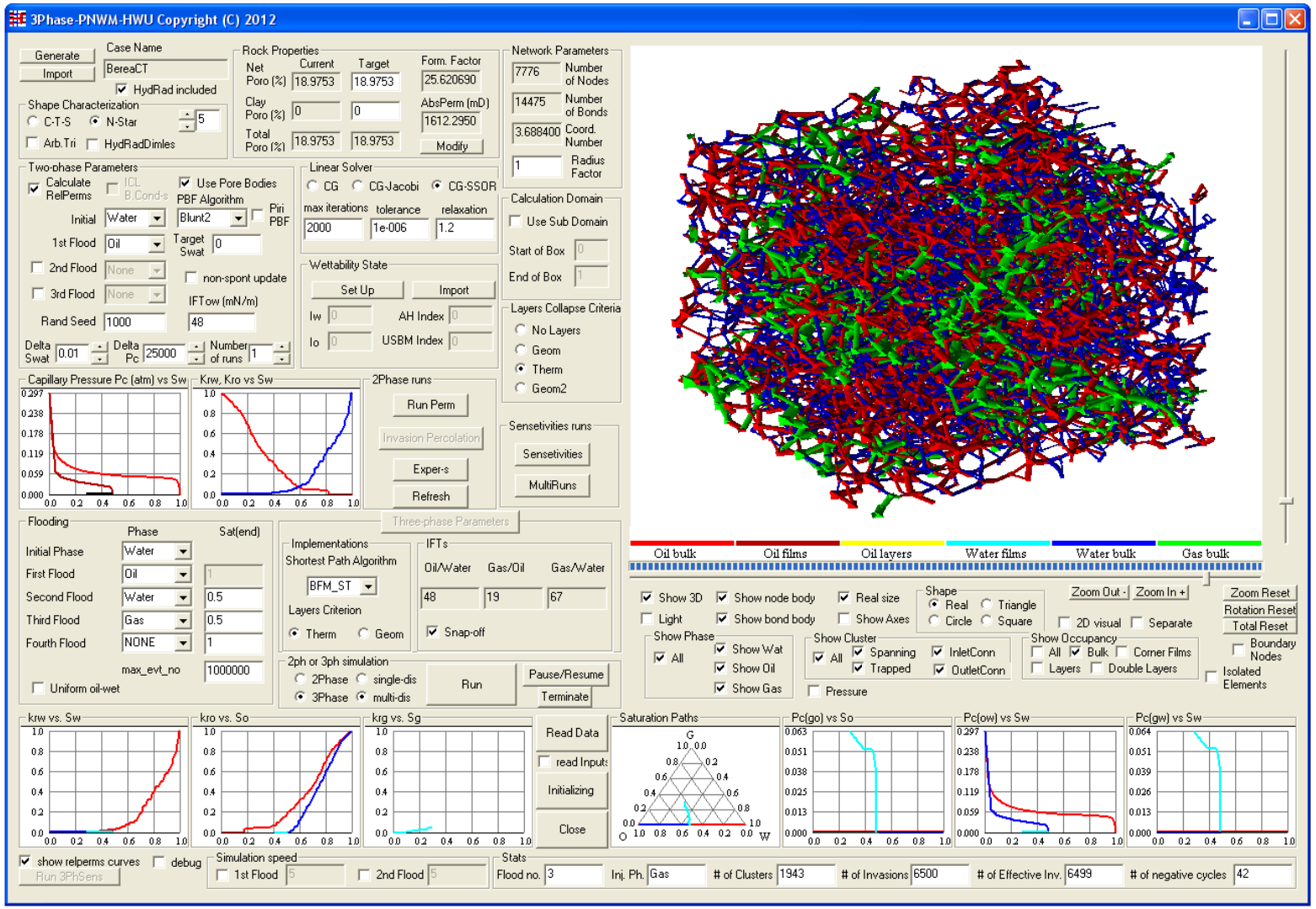

Figure B.11: Graphic user interface.

C

STONE'S MODELS

Here we give all general equations that are required to calculate three-phase relative permeabilities. Two sets of two-phase relative permeabilities, for oil-water and gas-oil, are required to compute the three-phase relative permeabilities. Since Stone assumes that the relative permeabilities of water and gas are function of their own saturations only, then water relative permeability is taken from oil-water data and gas relative permeability is taken from gas-oil data. For Stone I, oil relative permeability is given by

$$k_{ro} = \frac{S_{oe} k_{ro(w)} k_{ro(g)}}{k_{ro(wi)}(1 - S_{we})(1 - S_{ge})} \tag{C.6}$$

where

$$S_{oe} = \frac{S_o - S_{om}}{1 - S_{wi} - S_{om}}, \tag{C.7}$$

$$S_{we} = \frac{S_w - S_{om}}{1 - S_{wi} - S_{om}}. \tag{C.8}$$

$$S_{ge} = \frac{S_g - S_{om}}{1 - S_{wi} - S_{om}}. \tag{C.9}$$

$k_{ro(wi)}$ is the oil relative permeability for an oil/water system measured at irreducible water saturation with no gas present.

$k_{ro(w)}$ is calculated at $S_o = 1 - S_w$, and $k_{ro(g)}$ is calculated at $S_o = 1 - S_g - Swi$ S_{om} is the minimum residual oil saturation. In this work, S_{om} is taken to be the minimum of the critical oil-to-water saturation and the critical oil-to-gas saturation.

The Stone II computes oil relative permeability as

$$k_{ro} = (k_{ro(w)} + k_{ro(wi)}k_{rw(o)})(k_{ro(g)} + k_{ro(wi)}k_{rg(o)}) - k_{ro(wi)}(k_{rw(o)} + k_{rg(o)}). \quad \text{(C.10)}$$

$k_{ro(g)}$ and $k_{ro(w)}$ are measured at S_o given for Stone I.

BIBLIOGRAPHY

A. W. Adamson and A. P. Gast. *Physical Chemistry of Surfaces*. John Wiley and Sons, Inc., New York, 6th edition, 1997.

A. S. Al-Kharusi and M. J. Blunt. Network extraction from sandstone and carbonate pore space images. *Journal of Petroleum Science and Engineering*, 56(4): 219–231, 2007.

R. Amin and T. N. Smith. Interfacial tension and spreading coefficient under reservoir conditions. *Fluid Phase Equilibria*, 142(1–2):231 – 241, 1998.

J. Y. Arns, V. Robins, A. P. Sheppard, R. M. Sok, W. V. Pinczewski, and M. A. Knackstedt. Effect of network topology on relative permeability. *Transport in Porous Media*, 55(1):21–46, 2004.

L. E. Baker. Three-phase relative permeability correlations. In *the SPE/DOE Enhanced Oil Recovery Symposium, Tulsa, Oklahoma*, April 1988. SPE/ODE 17369.

S. Bakke and P. E. Øren. 3-d pore-scale modelling of sandstones and flow simulations in the pore networks. *SPE Journal*, 2(2):136–149, 1997.

F. E. Bartell and H. J. Osterhof. Determination of the wettability of a solid by a liquid. *Industrial & Engineering Chemistry*, 19(11):1277–1280, 1927.

R. Bellman. On a routing problem. *Quarterly of Applied Mathematics*, 16:87–90, 1958.

M. J. Blunt. Effects of heterogeneity and wetting on relative permeability using pore level modeling. *SPE Journal*, 2(1):70–87, 1997.

M. J. Blunt. Physically-based network modeling of multiphase flow in intermediate-wet porous media. *Journal of Petroleum Science and Engineering*, 20(3-4):117–125, 1998.

M. J. Blunt. An empirical model for three-phase relative permeability. *SPE Journal*, 5(4):435–445, 2000.

D. F. Boneau and R. L. Clampitt. A surfactant system for the oil-wet sandstone of the North Burbank Unit. *Journal of Petroleum Technology*, 29(5):501–506, 1977.

S. L. Bryant and M. J. Blunt. Prediction of relative permeability in simple porous media. *Physical Review A*, 46(4):2004, 1992.

S. L. Bryant, P. R. King, and D. W. Mellor. Network model evaluation of permeability and spatial correlation in a real random sphere packing. *Transport in Porous Media*, 11(1):53–70, 1993a.

S. L. Bryant, D. W. Mellor, and C. A. Cade. Physically representative network models of transport in porous media. *AIChE Journal*, 39(3):387–396, 1993b.

I. Chatzis, A. Kantzas, and F. A. L. Dullien. On the investigation of gravity-assisted inert gas injection using micromodels, long berea sandstone cores, and computer-assisted tomography. In *SPE Annual Technical Conference and Exhibition*, 2-5 October 1988.

S. Chen and G. D. Doolen. Lattice Boltzmann method for fluid flows. *Annual Review of Fluid Mechanics*, 30(1):329–364, 1998.

B. V. Cherkassky and A. V. Goldberg. Negative-cycle detection algorithms. *Mathematical Programming*, 85(2):277–311, 1999.

J. R. Christensen, E. H. Stenby, and A. Skauge. Review of WAG field experience. *SPE Reservoir Evaluation & Engineering*, 4(2):97–106, 2001.

J. Coenen, E. Tchouparova, and X. Jing. Measurement parameters and resolution aspects of micro x-ray tomography for advanced core analysis. In *Proceedings of the International Symposium of the Society of Core Analysts, Abu Dhabi, UAE*, 5-9 October 2004.

M. E. Coles, R. D. Hazlett, E. L. Muegge, K. W. Jones, B. Andrews, B. Dowd, P. Siddons, A. Peskin, P. Spanne, and W. E. Soll. Developments in synchrotron x-ray microtomography with applications to flow in porous media. *SPE Reservoir Evaluation & Engineering*, 1(4):288–296, 1998.

J. F. Delerue and E. Perrier. Dxsoil, a library for 3d image analysis in soil science. *Computers & Geosciences*, 28(9):1041–1050, 2002.

D. A. Dicarlo, A. Sahni, and M. J. Blunt. The effect of wettability on three-phase relative permeability. *Transport in Porous Media*, 39:347–366, 2000.

H. Dong and M. J. Blunt. Pore-network extraction from micro-computerized-tomography images. *Phys. Rev. E*, 80:036307, 2009.

F. A. L. Dullien. *Porous media: fluid transport and pore structure*. Academic Press, San Diego, CA, 2nd edition, 1992.

J. H. Dunsmuir, S. R. Ferguson, K. L. D'Amico, and J. P. Stokes. X-ray microtomography: a new tool for the characterization of porous media. In *SPE Annual Technical Conference and Exhibition, Dallas, Texas*, 6-9 October 1991.

P. Egermann, O. Vizika, L. Dallet, C. Requin, and F. Sonier. Hysteresis in three-phase flow: Experiments, modeling and reservoir simulations. In *SPE European Petroleum Conference, Paris, France*, 24-25 October 2000. SPE 65127.

D. J. Element, J. H. K. Masters, N. C. Sargent, A. J. Jayasekera OBE, and S. G. Goodyear. Assessment of three-phase relative permeability models using laboratory hysteresis data. In *Proceedings of the SPE International Improved Oil Recovery Conference in Asia Pacific, Kuala Lumpur, Malaysia*, October 2003. SPE 84903.

R. W. Falta, K. Pruess, I. Javandel, and P. A. Witherspoon. Numerical modeling of steam injection for the removal of nonaqueous phase liquids from the subsurface: 1. numerical formulation. *Water Resources Research*, 28(2):433–449, 1992a.

R. W. Falta, K. Pruess, I. Javandel, and P. A. Witherspoon. Numerical modeling of steam injection for the removal of nonaqueous phase liquids from the subsurface: 2. code validation and application. *Water Resources Research*, 28(2): 451–465, 1992b.

I. Fatt. The network model of porous media i. capillary pressure characteristics. *Trans. AIME*, 207(7):144–159, 1956.

D. H. Fenwick and M. J. Blunt. Pore level modelling of three phase flow in porous media. In *Proceedings of the 8th European Symposium on Improved Oil Recovery, Vienna, Austria*, May 1995.

D. H. Fenwick and M. J. Blunt. Network modeling of three-phase flow in porous media. *SPE Journal*, 3(1):86–96, 1998a.

D. H. Fenwick and M. J. Blunt. Three-dimensional modeling of three phase imbibition and drainage. *Advances in Water Resources*, 21(2):121–143, 1998b.

T. Firincioglu, M. J. Blunt, and D. Zhou. Three-phase flow and wetability effects in triangular capillaries. *Colloids and Surfaces A: Physicochemical and Engineering Aspects*, 155(2-3):259–276, 1999.

L. R. Ford. *Network Flow Theory*. Paper P-923. Rand Corporation, 1956.

A. S. Grader and D. J. O'Meara Jr. Dynamic displacement measurements of three-phase relative permeabilities using three immiscible liquids. In *SPE Annual Technical Conference and Exhibition, Houston, Texas*, 2-5 October 1988. SPE 18293.

J. W. Grate, K. J. Dehoff, M. G. Warner, J. W. Pittman, T. W. Wietsma, C. Zhang, and M. Oostrom. Correlation of oil-water and air-water contact angles of diverse silanized surfaces and relationship to fluid interfacial tensions. *Langmuir*, 28(18):7182–7188, 2012.

A. A. Heiba, H. T. Davis, and L. E. Scriven. Effect of wettability on two-phase relative permeabilities and capillary pressures. In *Proceedings of the 58th SPE Annual Technical Conference and Exhibition, San Francisco, CA*, 5-8 October 1983. SPE 12172.

A. A. Heiba, H. T. Davis, and L. E. Scriven. Statistical network theory of three-phase relative permeabilities. In *SPE Enhanced Oil Recovery Symposium, Tulsa, Oklahoma*, 15-18 April 1984. SPE 12690.

J. O. Helland, M. I. J. van Dijke, K. S. Sorbie, and S. M. Skjæveland. Three-phase relative permeability from mixedwet triangular and star-shaped pores. In *Proceedings of the Symposium on Reservoir Wettability, Bergen, Norway*, 18-19 September 2006.

J. O. Helland, A. V. Ryazanov, and M. I. J. van Dijke. Characterization of pore shapes for pore network models. In *Proceedings of the 11th European Conference on the Mathematics of Oil Recovery (ECMOR XI), Bergen, Norway*, 8 September 2008.

R. Holm, M.I.J. van Dijke, and S. Geiger. Three-phase flow modelling using pore-scale capillary pressures and relative permeabilities for mixed-wet media at the continuum-scale. *Transport in Porous Media*, 81(3):423–442, 2010.

M. H. Hui and M. J. Blunt. Effects of wettability on three-phase flow in porous media. *Journal of Physical Chemistry B*, 104(16):3833–3845, 2000a.

M. H. Hui and M. J. Blunt. Pore-scale modeling of three-phase flow and the effects of wettability. In *Proceedings of SPE/DOE Improved Oil Recovery Symposium, Tulsa, Oklahoma*, 3-5 April 2000b. SPE 59309.

D. D. Jackson, G. L. Andrews, and E. L. Claridge. Optimum WAG ratio vs. rock wettability in co2 flooding. In *the 60fh Annual Technical Conference and Exhibition of Society of Petroleum Engineers, Las Vegas, NV*, September 1985. SPE 14303.

P. P. Jadhunandan and N. R. Morrow. Effect of wettability on waterflood recovery for crude-oil/brine/rock systems. *SPE Reservoir Engineering*, 10(1):40–46, 1995.

Z. Jiang, K. Wu, G. Couples, M. I. J. van Dijke, K. S. Sorbie, and J. Ma. Efficient extraction of networks from three-dimensional porous media. *Water Resources Research*, 43(12):W12S03, 2007.

Z. Jiang, M. I. J. van Dijke, K. Wu, G. D. Couples, K. S. Sorbie, and J. Ma. Stochastic pore network generation from 3d rock images. *Transport in Porous Media*, 94:571–593, 2012.

V. Joekar-Niasar, M. Prodanovic, D. Wildenschild, and S. M. Hassanizadeh. Network model investigation of interfacial area, capillary pressure and saturation relationships in granular porous media. *Water Resour. Res*, 46(6):W06526, 2010.

R. E. Johnson and R. H. Dettre. *Wetting of Low Energy Surfaces*, volume 49 of *Surfactant Science Series*. In: J. C. Berg (Ed.), Wettability. Marcel Dekker Inc., New York, 1993.

R. Juanes and T. W. Patzek. Three-phase displacement theory: An improved description of relative permeabilities. *SPE Journal*, 9(3):302–313, 2004.

M. Kalam, S. Negahban, A. Al-Rawahi, and I. Al Hosani. Miscible gas injection tests in carbonates and its impact on field development. In *SPE Reservoir Characterisation and Simulation Conference and Exhibition, Abu Dhabi, UAE*, 9-11 October 2011.

M. A. Knackstedt, M. Sahimi, and A. P. Sheppard. Invasion percolation with long-range correlations: First-order phase transition and nonuniversal scaling properties. *Phys. Rev. E*, 61:4920–4934, 2000.

A. R. Kovscek, H. Wong, and C. J. Radke. A pore-level scenario for the development of mixed wettability in oil reservoirs. *AIChE Journal*, 39(6):1072–1085, 1993.

C. Laroche. Secondary and tertiary gas injection experiments in heterogeneous wettability micromodels. In *Proceedings of* SPE *European Petroleum Conference, The Hague, The Netherlands*, 20-22 October 1998.

C. Laroche, O. Vizika, and F. Kalaydjian. Network modeling as a tool to predict three-phase gas injection in heterogeneous wettability porous media. *Journal of Petroleum Science and Engineering*, 24(2-4):155–168, 1999a.

C. Laroche, O. Vizika, and F. Kalaydjian. Network modeling to predict the effect of wettability heterogeneities on multiphase flow. In *SPE Annual Technical Conference and Exhibition, Houston, Texas*, 3-6 October 1999b.

J. K. Larsen, N. Bech, and A. Winter. Three-phase immiscible WAG injection: Micromodel experiments and network models. In *SPE/DOE Improved Oil Recovery Symposium, Tulsa, Oklahoma*, 3-5 April 2000. SPE 59324.

R. Lenormand and C. Zarcone. Role of roughness and edges during imbibition in square capillaries. In *Proceedings of SPE Annual Technical Conference and Exhibition, Houston, TX, USA: Soc of Petroleum Engineers of AIME, USA*, 1984. SPE 13264.

R. Lenormand, C. Zarcone, and A. Sarr. Mechanisms of the displacement of one fluid by another in a network of capillary ducts. *J. Fluid Mech*, 135(34):337–353, 1983.

T. R. Lerdahl, P. E. Øren, and S. Bakke. A predictive network model for three-phase flow in porous media. In *Improved Oil Recovery Symposium, Tulsa, Oklahoma*, 3-5 April 2000. SPE 59311.

W. B. Lindquist and A. Venkatarangan. Investigating 3d geometry of porous media from high resolution images. *Physics and Chemistry of the Earth, Part A: Solid Earth and Geodesy*, 24(7):593–599, 1999.

W. B. Lindquist, S. M. Lee, D. A. Coker, K. Jones, and P. Spanne. Medial axis analysis of three dimensional tomographic images of drill core samples. *J. Geophys. Res*, 1:111, 1996.

E. J. Mackay, G. D. Henderson, D. H. Tehrani, and A. Danesh. The importance of interfacial tension on fluid distribution during depressurization. *SPE Reservoir Evaluation & Engineering*, 1(5):408–415, 1998.

V. Mani and K. K. Mohanty. Effect of the spreading coefficient on three-phase flow in porous media. *Journal of Colloid and Interface Science*, 187(1):45 – 56, 1997.

V. Mani and K. K. Mohanty. Pore-level network modeling of three-phase capillary pressure and relative permeability curves. *SPE Journal*, 3(3):238–248, 1998.

G. Mason and N. R. Morrow. Capillary behavior of a perfectly wetting liquid in irregular triangular tubes. *Journal of Colloid and Interface Science*, 141(1):262–274, 1991.

R. P. Mayer and R. A. Stowe. Mercury porosimetry–breakthrough pressure for penetration between packed spheres. *Journal of Colloid Science*, 20(8):893–911, 1965.

S. R. McDougall and K. S. Sorbie. The impact of wettability on waterflooding: pore-scale simulation. *SPE Reservoir Engineering*, 10(3):208–213, 1995.

K. K. Mohanty, H. T. Davis, and L. E. Scriven. Physics of oil entrapment in water-wet rock. *SPE Reservoir Engineering*, 2(1):113–128, 1987.

E. F. Moore. The shortest path through a maze. In *Proceedings of the International Symposium on the Theory of Switching*. Harvard University Press, 1959.

N. Morrow. The effects of surface roughness on contact: Angle with special reference to petroleum recovery. *Journal of Canadian Petroleum Technology*, 14 (4), 1975.

C. Nardi, O. Lopez, P. E. Øren, R. Held, and E. B. Petersen Jr. Pore-scale modelling of three-phase flow: comparative study with experimental reservoir data. In *The International Symposium of the Society of Core Analysts, Noordwijk, The Netherlands*, 27-30 September 2009.

M. J. Oak. Three-phase relative permeability of water-wet berea. In *Proceedings of the SPE/DOE Enhanced Oil Recovery Symposium, Tulsa, Oklahoma*, 22-25 April 1990. SPE 20183.

H. Okabe and M. J. Blunt. Pore space reconstruction of vuggy carbonates using microtomography and multiple-point statistics. *Water Resources Research*, 43 (12):12–02, 2007.

P. E. Øren and S. Bakke. Process based reconstruction of sandstones and prediction of transport properties. *Transport in Porous Media*, 46(2):311–343, 2002.

P. E. Øren and S. Bakke. Reconstruction of berea sandstone and pore-scale modelling of wettability effects. *Journal of Petroleum Science and Engineering*, 39(3-4): 177–199, 2003.

P. E. Øren and W. V. Pinczewski. The effect of film-flow on the mobilization of waterflood residual oil by gas flooding. In *Proceedings of the 6th European Symposium on Improved Oil Recovery, Stavanger*, May 1991.

P. E. Øren and W. V. Pinczewski. The effect of wettability and spreading coefficients on the recovery of waterflood residual oil by miscible gasflooding. *SPE Formation Evaluation*, 9(2):149–156, 1994.

P. E. Øren and W. V. Pinczewski. Fluid distribution and pore-scale displacement mechanisms in drainage dominated three-phase flow. *Transport in Porous Media*, 20:105–133, 1995.

P. E. Øren, J. Billiotte, and W. V. Pinczewski. Mobilization of waterflood residual oil by gas injection for water-wet conditions. *SPE Formation Evaluation*, 7(1): 70–78, 1992.

P. E. Øren, J. Billiotte, and W. V. Pinczewski. Pore-scale network modelling of waterflood residual oil recovery by immiscible gas flooding. In *Proceedings of the SPE/DOE Symposium in Improved Oil Recovery, Tulsa, Oklahoma*, 17-20 April 1994. SPE 27814.

P. E. Øren, S. Bakke, and O. J. Arntzen. Extending predictive capabilities to network models. *SPE Journal*, 3(4):324–336, 1998.

C. Pan, M. Hilpert, and C. T. Miller. Lattice-Boltzmann simulation of two-phase flow in porous media. *Water Resources Research*, 40(1):W01501, 2004.

T. Patzek. Verification of a complete pore network simulator of drainage and imbibition. *SPE Journal*, 6(2):144–156, 2001.

T. W. Patzek and D. B. Silin. Shape factor and hydraulic conductance in non-circular capillaries:: I. one-phase creeping flow. *Journal of Colloid and Interface Science*, 236(2):295–304, 2001.

G. G. Pereira. Numerical pore-scale modeling of three-phase fluid flow: Comparison between simulation and experiment. *Phys. Rev. E*, 59:4229–4242, Apr 1999.

G. G. Pereira, W. V. Pinczewski, D. Y. C. Chan, L. Paterson, and P. E. Øren. Pore-scale network model for drainage-dominated three-phase flow in porous media. *Transport in Porous Media*, 24:167–201, 1996.

L. Peters, R. Arts, G. Brouwer, C. Geel, S. Cullick, R. Lorentzen, Y. Chen, N. Dunlop, F. Vossepoel, R. Xu, et al. Results of the Brugge benchmark study for flooding optimization and history matching. *SPE Reservoir Evaluation & Engineering*, 13(3):391–405, 2010.

E. B. Jr. Petersen, A. Lohne, K. O. Vatne, J. O. Helland, G. Virnovsky, and P. E. Øren. Relative permeabilities for two- and three phase flow processes relevant to the depressurization of the Statfjord field. 29 October - 2 November 2008.

M. Piri. *Pore-scale modelling of three-phase flow*. PhD thesis, Imperial College, 2003.

M. Piri and M. J. Blunt. Three-phase threshold capillary pressures in noncircular capillary tubes with different wettabilities including contact angle hysteresis. *Phys. Rev. E*, 70:061603, 2004.

M. Piri and M. J. Blunt. Three-dimensional mixed-wet random pore-scale network modeling of two- and three-phase flow in porous media. i. model description. *Physical Review E*, 71(2):026301, 2005a.

M. Piri and M. J. Blunt. Three-dimensional mixed-wet random pore-scale network modeling of two- and three-phase flow in porous media. ii. results. *Physical Review E*, 71(2):026302, 2005b.

H. M. Princen. Capillary phenomena in assemblies of parallel cylinders : I. capillary rise between two cylinders. *Journal of Colloid and Interface Science*, 30(1): 69–75, 1969a.

H. M. Princen. Capillary phenomena in assemblies of parallel cylinders : II. capillary rise in systems with more than two cylinders. *Journal of Colloid and Interface Science*, 30(3):359–371, 1969b.

H. M. Princen. Capillary phenomena in assemblies of parallel cylinders : III. liquid columns between horizontal parallel cylinders. *Journal of Colloid and Interface Science*, 34(2):171–184, 1970.

R. Qi, T. LaForce, and M. Blunt. Design of carbon dioxide storage in oil fields. In *SPE Annual Technical Conference and Exhibition, Denver, Colorado, USA*, 21-24 September 2008.

R. Qi, T. C. LaForce, and M. J. Blunt. A three-phase four-component streamline-based simulator to study carbon dioxide storage. *Computational Geosciences*, 13 (4):493–509, 2009.

M. Robin, E. Rosenberg, and O. Fassi-Fihri. Wettability studies at the pore level: a new approach by use of cryo-sem. *SPE Formation Evaluation*, 10(1):11–19, 1995.

J. S. Rowlinson and B. Widom. *Molecular theory of capillarity*. Clarendon Press, Oxford, 1989.

A. Ryazanov. *Pore-Scale Network Modelling of Residual Oil Saturation in Mixed-Wet Systems*. PhD thesis, Heriot-Watt University, June 2011.

A. V. Ryazanov, M. I. J. van Dijke, and K. S. Sorbie. Two-phase pore-network modelling: existence of oil layers during water invasion. *Transport in Porous Media*, 80(1):79–99, 2009.

A. V. Ryazanov, M. I. J. van Dijke, and K. S. Sorbie. Pore-network prediction of residual oil saturation based on oil layer drainage in mixed-wet systems. In *SPE Improved Oil Recovery Symposium, Tulsa, Oklahoma, USA*, 24-28 April 2010. SPE 129919.

A. Sahni, J. Burger, and M. J. Blunt. Measurement of three phase relative permeability during gravity drainage using ct scanning. In *SPE/DOE Improved Oil Recovery Symposium, Tulsa, Oklahoma*, 19-22 April 1998.

A. P. Sheppard, R. M. Sok, and H. Averdunk. Improved pore network extraction methods. In *International Symposium of the Society of Core Analysts, Toronto, Canada*, pages 21–25, 2005.

A. P. Sheppard, R. M. Sok, H. Averdunk, V. B. Robins, and A. Ghous. Analysis of rock microstructure using high-resolution X-ray tomography. In *Proceedings of the International Symposium of the Society of Core Analysts, Trondheim, Norway*, 12-16 September 2006.

D. Silin and T. Patzek. Pore space morphology analysis using maximal inscribed spheres. *Physica A: Statistical Mechanics and its Applications*, 371(2):336–360, 2006.

D. Silin, J. Guodong, and T. Patzek. Robust determination of the pore space morphology in sedimentary rocks. In *SPE Annual Technical Conference and Exhibition, Denver, Colorado*, 5-8 October 2003.

D. B. Silin, G. Jin, and T. W. Patzek. Robust determination of the pore space morphology in sedimentary rocks. *J. Petrol. Technol.*, 56(5):69–70, 2004.

M. Sohrabi, G. D. Henderson, D. H. Tehrani, and A. Danesh. Visualisation of oil recovery by water alternating gas (WAG) injection using high pressure micro-

models - water-wet system. In *SPE Annual Technical Conference and Exhibition, Dallas, Texas*, 1-4 October 2000. SPE 63000.

M. Sohrabi, D. H. Tehrani, A. Danesh, and G. D. Henderson. Visualisation of oil recovery by water alternating gas (WAG) injection using high pressure micromodels - oil-wet and mixed-wet systems. In *SPE Annual Technical Conference and Exhibition, New Orleans, Louisiana*, 30 September-3 October 2001. SPE 71494.

M. Sohrabi, D. H. Tehrani, A. Danesh, and G. D. Henderson. Visualization of oil recovery by water-alternating-gas injection using high-pressure micromodels. *SPE Journal*, 9(3):290–301, 2004.

R. M. Sok, M. A. Knackstedt, A. P. Sheppard, W. V. Pinczewski, W. B. Lindquist, A. Venkatarangan, and L. Paterson. Direct and stochastic generation of network models from tomographic images; effect of topology on residual saturations. *Transport in Porous Media*, 46(2):345–371, 2002.

W. E. Soll and M. A. Celia. A modified percolation approach to simulating three-fluid capillary pressure-saturation relationships. *Advances in Water Resources*, 16(2):107 – 126, 1993.

W. E. Soll, M. A. Celia, and J. L. Wilson. Micromodel studies of three-fluid porous media systems: Pore-scale processes relating to capillary pressure-saturation relationships. *Water Resources Research*, 29(9):2963–2974, 1993.

P. Spanne, J. F. Thovert, C. J. Jacquin, W. B. Lindquist, K. W. Jones, P. M. Adler, et al. Synchrotron computed microtomography of porous media: topology and transports. *Physical Review Letters*, 73(14):2001–2004, 1994.

H. L. Stone. Probability model for estimating three-phase relative permeability. *Journal of Petroleum Technology*, 22(2):214–218, 1970.

H. L. Stone. Estimation of three-phase relative permeability and residual oil data. *Journal of Canadian Petroleum Technology*, 12(4):53–61, 1973.

V. Suicmez, M. Piri, and M. J. Blunt. Pore-scale simulation of water alternate gas injection. *Transport in Porous Media*, 66:259–286, 2007.

V. S. Suicmez, M. Piri, and M. J. Blunt. Pore-scale modeling of three-phase WAG injection: Prediction of relative permeabilities and trapping for different displacement cycles. In *SPE/DOE Symposium on Improved Oil Recovery, Tulsa, Oklahoma, USA*, 22-26 April 2006. SPE 95594.

D. S. Svirsky, M. I. J. van Dijke, and K. S. Sorbie. Prediction of three-phase relative permeabilities using a pore-scale network model anchored to two-phase data. *SPE Reservoir Evaluation and Engineering*, 10(5), 2007.

R. E. Tarjan. Shortest paths. Technical report, AT & T Bell Laboratories, Murray Hill, NJ., 1981.

P. H. Valvatne and M. J. Blunt. Predictive pore-scale modeling of two-phase flow in mixed wet media. *Water Resources Research*, 40(7):W07406, 2004.

P. H. Valvatne, M. Piri, X. Lopez, and M. J. Blunt. Predictive pore-scale modeling of single and multiphase flow. *Transport in Porous Media*, 58(1):23–41, 2005.

M. I. J. van Dijke and K. S. Sorbie. The relation between interfacial tensions and wettability in three-phase systems: consequences for pore occupancy and relative permeability. *Journal of Petroleum Science and Engineering*, 33(1):39–48, 2002.

M. I. J. van Dijke and K. S. Sorbie. Existence of fluid layers in the corners of a capillary with non-uniform wettability. *Journal of Colloid and Interface Science*, 293(2):455–463, 2006.

M. I. J. van Dijke, K. S. Sorbie, and S. R. McDougall. A process-based approach for three-phase capillary pressure and relative permeability relationships in mixed-wet systems. 3-5 April 2000. SPE 59310.

M. I. J. van Dijke, K. S. Sorbie, and S. R. McDougall. Saturation-dependencies of three-phase relative permeabilities in mixed-wet and fractionally wet systems. *Advances in Water Resources*, 24(3):365–384, 2001a.

M. I. J. van Dijke, K. S. Sorbie, and S. R. McDougall. Three-phase capillary pressure and relative permeability relationships in mixed-wet systems. *Transport in Porous Media*, 44(1):1–32, 2001b.

M. I. J. van Dijke, M. Lago, K. S. Sorbie, and M. Araujo. Free energy balance for three fluid phases in a capillary of arbitrarily shaped cross-section: capillary entry pressures and layers of the intermediate-wetting phase. *Journal of Colloid and Interface Science*, 277(1):184–201, 2004a.

M. I. J. van Dijke, K. S. Sorbie, M. Sohrabi, and A. Danesh. Three-phase flow WAG processes in mixed-wet porous media: Pore-scale network simulations and comparison with water-wet micromodel experiment. *SPE Journal*, 9(1): 57–66, 2004b.

M. I. J. van Dijke, K. S. Sorbie, M. Sohrabi, and A. Danesh. Simulation of WAG floods in an oil-wet micromodel using a 2-D pore-scale network model. *Journal of Petroleum Science and Engineering*, 52(1-4):71 – 86, 2006.

M. I. J. van Dijke, M. Piri, J. O. Helland, K. S. Sorbie, M. J. Blunt, and S. M. Skjæveland. Criteria for three-fluid configurations including layers in a pore with nonuniform wettability. *Water Resour. Res.*, 43(12):W12S05, 2007.

M. I. J. van Dijke, J. E. Juri, and K. S. Sorbie. Shortest path algorithm for pore-scale simulation of water-alternating-gas injection. In *Proceedings of the 11th European Conference on the Mathematics of Oil Recovery (ECMOR XI), Bergen, Norway*, September 2008.

G. P. Willhite. *Waterflooding, Society of Petroleum Engineers.* SPE Textbook Series. Society of Petroleum Engineers, 1986. ISBN 9781555630058.

K. Wu, M. I. J. van Dijke, G. D. Couples, Z. Jiang, J. Ma, K. S. Sorbie, J. Crawford, I. Young, and X. Zhang. 3D stochastic modelling of heterogeneous porous media–applications to reservoir rocks. *Transport in Porous Media*, 65(3):443–467, 2006.

Y. Zaretskiy, S. Geiger, K. Sorbie, and M. Förster. Efficient flow and transport simulations in reconstructed 3D pore geometries. *Advances in Water Resources*, 33(12):1508 – 1516, 2010.

D. G. Zhou and M. J. Blunt. Effect of spreading coefficient on the distribution of light non-aqueous phase liquid in the subsurface. *Journal of Contaminant Hydrology*, 25(1-2):1–19, 1997.